GLOBAL APPROACH TO THE SPECTRAL PROBLEM OF MICROINSTABILITIES IN TOKAMAK PLASMAS USING A GYROKINETIC MODEL

THÈSE N^{O} 1701 (1997)

PRÉSENTÉE AU DÉPARTEMENT DE PHYSIQUE

ÉCOLE POLYTECHNIQUE FÉDÉRALE DE LAUSANNE

POUR L'OBTENTION DU GRADE DE DOCTEUR ÈS SCIENCES

PAR

Stephan BRUNNER
Ingénieur physicien diplômé EPF
originaire de Wald (ZH)

acceptée sur proposition du jury:

Dr J. Vaclavik, directeur de thèse
Dr J.W. Connor, corapporteur
Dr X. Garbet, corapporteur
Dr O. Sauter, corapporteur

Lausanne, EPFL
1997

Abstract

Ion temperature gradient (ITG) -related instabilities are studied in tokamak-like plasmas with the help of a new global eigenvalue code. Ions are modeled in the frame of gyrokinetic theory so that finite Larmor radius effects of these particles are retained to all orders. Non-adiabatic trapped electron dynamics is taken into account through the bounce-averaged drift kinetic equation. Assuming electrostatic perturbations, the system is closed with the quasineutrality relation. Practical methods are presented which make this global approach feasible. These include a non-standard wave decomposition compatible with the curved geometry as well as adapting an efficient root finding algorithm for computing the unstable spectrum. These techniques are applied to a low pressure configuration given by a large aspect ratio torus with circular, concentric magnetic surfaces. Simulations from a linear, time evolution, particle in cell code provide a useful benchmark. Comparisons with local ballooning calculations for different parameter scans enable further validation while illustrating the limits of that representation at low toroidal wave numbers or for non-interchange-like instabilities. The stabilizing effect of negative magnetic shear is also considered, in which case the global results show not only an attenuation of the growth rate but also a reduction of the radial extent induced by a transition from the toroidal- to the slab-ITG mode. Contributions of trapped electrons to the ITG instability as well as the possible coupling to the trapped electron mode are clearly brought to the fore.

Traduction de l'Abstract

Différentes instabilités liées au gradient de température ionique, notées GTI, sont étudiées dans des plasmas de tokamak à l'aide d'un nouveau code global aux valeurs propres. Les ions sont modélisés dans le cadre de la théorie gyrocinétique afin que les effets du rayon fini de Larmor de ces particules soient retenus à tous les ordres. La dynamique non-adiabatique des électrons piégés est prise en compte à l'aide de l'équation cinétique de dérive ('drift kinetic'), moyennée sur la période de piégage. Sous l'hypothèse de perturbations électrostatiques, le système est fermé par la relation de quasineutralité. Cette approche globale a nécessité une décomposition ondulatoire non-standard qui est compatible avec la géométrie curviligne, de même que l'adaptation d'un algorithme de recherche de zéros pour calculer le spectre instable. Ces techniques sont appliquées à une configuration torique de grand rapport d'aspect, avec des surfaces magnétiques circulaires concentriques. Des simulations d'un code linéaire d'évolution temporelle du genre 'particle in cell' fournissent un repère utile. La comparaison avec des calculs 'ballooning' locaux pour différentes variations de paramètre, permettent d'effectuer une validation supplémentaire, tout en illustrant les limites de cette représentation face à des nombres d'onde toroïdaux bas ainsi qu'à des instabilités qui ne sont pas du type 'interchange'. L'effet stabilisant du cisaillement magnétique négatif est également considéré; dans ce cas, les résultats globaux montrent non seulement une atténuation du taux de croissance mais aussi une réduction de l'extension radiale, toutes deux induites par la transition d'un mode GTI-torique à un mode GTI-plan. Les contributions des électrons piégés à l'instabilité GTI, de même que la possibilité d'un couplage entre l'instabilité GTI et le mode propre à ces particules, sont clairement mis en évidence.

Contents

Acknowledgments

I am very much indebted to Dr. Jan Vaclavik who has led me through this work, spending his time and sharing his knowledge with great generosity. I shall not forget the very privileged position I have held as his thesis student.

An essential contribution was provided by the collaboration with Mathieu Fivaz. I thank him for the numerous fruitful discussions.

I am very grateful to Guillaume Jost and Alexandre Pletzer for showing endless patience towards my ignorance of computers.

I wish to thank Professor Troyon for the interesting hours he spent answering my questions at the time I was an undergraduate student and later for giving me the opportunity to work in his institute.

My family and friends have been a great source of encouragement at all times. Vi ringrazio tutti!

I thank the external experts, Dr Connor and Dr Garbet, as well as the internal expert, Olivier Sauter, for examining this thesis.

Chapter 1

Introduction

1.1 A Brief History of Studies on ITG-Related Microinstabilities

Careful evaluation of energy losses in tokamak plasmas[1] has shown that they are usually well above those predicted by collisional neoclassical rates[2]. It is believed that microinstabilities, which subsist even when the most dangerous magnetohydrodynamic (MHD) modes have been suppressed, provide an alternative channel through which the plasma releases the extra amount of free energy associated with the spatial variations of physical quantities, thus contributing at least partly to the transport enhancement. The term microinstability refers to a whole class of low frequency destabilizing mechanisms arising from the different behaviors of electrons and ions in an inhomogeneous magnetized plasma. Due to the prominent role of average diamagnetic drifts in the presence of pressure gradients and the individual particle drifts related to gradients and curvature of the magnetic field, which are examples of such charge dependent phenomena, microinstabilities are often also called drift waves.

A particular type of drift wave is the ion temperature gradient (ITG) mode. The first experimental indications that this instability might be correlated to anomalous transport appeared in 1984 on the Alcator C tokamak[3]. Subsequent experiments confirm this hypothesis. This has triggered a great effort to establish a theoretical basis supporting the relevance of ITG-related instabilities to the transport anomaly.

The basic form of this instability appears in a straight magnetic system and therefore is called slab-ITG. It is essentially a sound wave destabilized by ion temperature gradients sufficiently steep with respect to the density variation. The possible existence of such modes had already been predicted in the 1960s by Rudakov and Sagdeev[4].

In a tokamak plasma, the nature of this mode can however be greatly altered by toroidal effects. At sufficiently high frequencies it will adopt the character of the more unstable toroidal-ITG, first identified by Horton, Choi and Tang[5]. Contrary to its slab counterpart, which is driven by the ion dynamics parallel to the magnetic field, the toroidal-ITG aligns along the magnetic field lines and becomes driven by the perpendicular drifts induced in such a curved system. These turn out to be destabilizing only when going in the same direction as the ion diamagnetic drift, that is usually on the outer side of the torus. As a consequence this mode tends to balloon so that it can localize in this so called unfavorable curvature region. This mechanism is characteristic of an interchange-type instability.

Another effect of toroidicity is the inevitable appearance of a local magnetic mirror in this outer region, where particles with low parallel velocities compared with the transverse ones become trapped. Their oscillating motion along the magnetic field line allows one to define the so called bounce frequency. If the frequency of the ITG mode falls below the ion bounce frequency, dynamics specific to these trapped particles become important and the instability undergoes a transition to the trapped ion mode (TIM). A theory of trapped particle modes was first established by Kadomtsev and Pogutse around 1966 [6, 7]. Only more recently has one realized the importance of trapped electrons, which due to their high bounce frequency can affect the ITG instability over all regimes. Romanelli and Briguglio have shown clearly the possible coupling between the toroidal-ITG and the trapped electron mode (TEM)[8]. This tends to be confirmed by experimental results revealing fluctuations propagating as well in the ion and electron diamagnetic directions[9].

Although a first rough understanding of these instabilities can be obtained with simple two fluid equations, these modes also comprise important microscopic features such as wave-particle resonances and finite Larmor radius (FLR) effects, therefore requiring a kinetic model for a full description. This is provided by the gyrokinetic equation (GKE) which is derived from the Boltzmann or Vlasov equation considering appropriate scalings: the time variation of the perturbation is slow compared with the gyrofrequency and the characteristic length of equilibrium large compared with the Larmor radii, however transverse wavelengths can take arbitrary values, leading to the mentioned FLR effects. Pioneering work for establishing linear gyrokinetic equations was carried out by Rutherford and Frieman[10] as well as Taylor and Hastie[11] in 1967, all employing a WKB ansatz. A simpler mathematical formulation was given by Catto[12] in 1977. Non-linear gyrokinetic equations were derived in the 1980s by Frieman and Chen[13] and using an elegant action-variational Lie perturbation technique by Hahm[14].

Gyrokinetic theory and increasing numerical resources have allowed one to tackle always more complex systems. After acquiring basic understanding of the slab-ITG[4] and the trapped particle modes[6, 7] by solving local dispersion relations, geometrical effects such as magnetic shear were investigated in slab configurations[15, 16]. Cylindrical plasmas were other one-dimensional systems considered[17, 18].

An important contribution for analyzing the two-dimensional problem of linear perturbations in an axisymmetric system was made by Connor, Hastie and Taylor around 1977 with the introduction of ballooning theory[19]. The associated representation enforces the interchange-like character, i.e. the tendency of certain modes to align with the magnetic field line, while at the same time satisfying the poloidal periodicity. Applying this ansatz for high toroidal wave numbers allows one to separate the fast variation of the phase factor from the slow modulation. This leads in lowest order to a one-dimensional equation for the envelope along the field line. First developed for studying MHD stability, it was applied successfully by Horton et al.[5] for describing the toroidal-ITG in the frame of a fluid model. Ballooning representation was then extensively used when solving the GKE [20, 21, 22, 23, 24, 25]. Except for very few cases[20] these calculations do not include a higher order WKB procedure for evaluating the radial structure. Hence, these results usually stay local to a magnetic surface and there remains some questioning on the actual radial extent of these modes.

For low toroidal wave numbers where the ballooning representation breaks down and the full two-dimensional problem cannot be reduced, very little linear computation has been carried out. This limit is of interest as it describes longer wavelength fluctuations which could lead to higher turbulent transport. This is supported by empirical results from certain non-dimensional transport scaling studies[26] indicating that Bohm-like trends characteristic of long wavelength modes are more in evidence than the gyro-Bohm scaling associated with shorter wavelength microinstabilities. Until recently the only published results from true global, linear computations came from a spectral code by Marchand, Tang and Rewoldt[27]. This model contains no FLR effects and is based on a second order expansion with respect to the radial excursion of trapped particles which leads to spurious modes[28] and thus to a difficult search of physical eigenfrequencies. The first version of this code was written in 1979 but due to the lack of numerical power had not been exploited at the time. Only ten years later, with the help of new generation computers and a more efficient root finding method has it been run for realistic tokamak parameters[28, 29]. But even in its optimized form this code is slow and difficult in use.

At present, computational power allows for non-linear gyrofluid[30, 31] and gyrokinetic [32, 33, 34] simulations. These are however still limited to flux tubes (radially local) or small configurations and the results from these different methods remain contradictory. So even today linear studies are not outdated. A linear calculation is the first systematic approach when considering additional physical effects such as non-adiabatic electrons, toroidal flow, reversed magnetic shear or shaping of equilibrium. Furthermore they are indispensable for defining marginal stability. Finally, for non-linear codes they allow valuable benchmarking of the linear stage of evolution and can provide information on possible channels of energy release and absorption.

1.2 Initial Goal and Present Status of this Work

The fact that very few full two-dimensional linear results are available in the potentially important low toroidal wave number regime has prompted us to undertake the development of a new, global, spectral gyrokinetic code. The aim was to keep FLR and finite radial orbit width effects to all orders which in particular would avoid generating non-physical modes. This leads to a two-dimensional integral equation which requires appropriate modeling and numerical methods to be solved. Starting in spring 1995, these techniques were first devised and tested in a simple cylindrical system. Toroidal effects were then introduced progressively. This allowed us a systematic introduction to the topic of microinstabilities, new for the group at CRPP. At present, our model is still quite simple in some respects as it considers the approximation of electrostatic perturbations in a collisionless plasma idealized by a large aspect ratio torus with concentric circular magnetic surfaces and furthermore neglects the dynamics specific to trapped ions. However it contains the full dynamics of circulating ions as well as non-adiabatic trapped electrons.

Parallel to the spectral approach a time evolution particle in cell (PIC) code has been written by Fivaz [35, 36]. Except for FLR effects included only to second order it contains full ion dynamics. Coupled to an MHD equilibrium code, it handles more realistic configurations. Electrons however are still approximated by taking their adiabatic response. In this way the eigenvalue and PIC methods are complementary. Comparisons[37] have led the way to the correct approximations and have given a better understanding of our results.

1.3 Outline

Chapter 2 provides an introduction to the physical concepts underlying this work. After a summary of the different kinetic models which will be used here for describing non-dissipative drift waves, a description of the slab-ITG, toroidal-ITG and trapped particle instabilities is given by solving local fluid and kinetic dispersion relations. The connection and possible coupling between these modes are also discussed. This part has no claim of completeness but can serve as an introductory guideline for someone new to the field and intending to carry on with this work. A clear review article on anomalous transport in general is given by Connor and Wilson[38]. A review specific to trapped particles, including the basic theory of the associated instabilities, is the paper of Kadomtsev and Pogutse[7].

The different techniques developed for solving the eigenvalue problem[39] are first presented in chapter 3 in the simple case of a periodic cylindrical system. The key elements are solving in the Fourier space relative to a particular mode decomposition and adapting an efficient root finding method [40] for identifying the spectra. Some illustrative results of slab-ITG modes in this configuration are also shown.

The methods devised in cylinder are applied to a first toroidal model which neglects trapped particle dynamics of ions and electrons. This is the subject of chapter 4. Having given the derivation of the corresponding eigenvalue equation and some details on its numerical implementation, results of different parameter scans are discussed. These are compared with those provided by PIC [34, 35] and ballooning[24, 41] calculations. The transition from the slab- to the toroidal-ITG is given particular attention and in this context the limits of the ballooning approximation are brought to the fore. Magnetic shear scans down to negative values have been performed. Motivation for such studies come from experimental evidence on TFTR[42], DIII-D[43, 44] and JT-60U[45] tokamaks of the formation of a transport barrier in regions of shear reversal accompanied by a reduction in core fluctuation amplitudes. Good confinement of such negative central shear (NCS) scenarios together with a large bootstrap current fraction and favorable ideal-MHD stability conditions had already been predicted by Kessel[46]. For peaked pressure profiles, these regimes however seem to be limited by resistive interchange instabilities[43, 44, 47].

Chapter 5 explains how trapped electrons are added to the global code through the bounce-averaged drift kinetic equation (DKE). Coupling of the TEM to the toroidal-ITG is analyzed along similar scans as the ones shown in chapter 4. Results are also compared with calculations from a local kinetic dispersion relation.

After the conclusions, three appendices have been written to ease the main text from lengthy algebra. Hence, appendix A repeats the derivation of the linear GKE following the procedure by Catto[12]. Appendix B explains how this equation can be solved in a general toroidal configuration. As an illustration the circular, large aspect ratio geometry is considered. Finally, the average toroidal precessional drift of trapped particles and the bounce-averaged DKE are rederived in appendix C.

Chapter 2

Basic Concepts

The linear response of a system is entirely determined by the non-perturbed initial state. We shall thus start by giving a brief overview of the properties of a stationary magnetically confined system and in particular consider the case of tokamak-type plasmas. Appropriate kinetic models for describing the different microinstabilities related to the ion temperature gradient instability are then introduced.

2.1 Tokamak Configuration

Magnetohydrodynamics (MHD) is well suited for describing the equilibrium state of magnetically confined fusion type systems:

$$\begin{aligned} \nabla p &= \vec{j} \times \vec{B}, && (2.1) \\ \nabla\times \vec{B} &= \mu_0 \, \vec{j}, && (2.2) \\ \nabla\cdot \vec{B} &= 0, && (2.3) \end{aligned}$$

where p is the plasma pressure, $\vec{j}$ the current density and $\vec{B}$ the self-consistent magnetic field.

The tokamak configuration is idealized by an axisymmetric toroidal plasma. In cylindrical coordinates (r, φ, z) all physical quantities are then independent of the toroidal angle φ. With this symmetry, (2.3) implies that the magnetic field must be of the form

$$\vec{B} = \nabla\psi \times \nabla\varphi + rB_\varphi \nabla\varphi,$$

where $2\pi\psi$ is the poloidal magnetic flux enclosed by a toroidal line:

$$\psi(r,z) = \frac{1}{2\pi}\int_{\Sigma(r,z)} \vec{B}\cdot d\,\vec{\sigma} = rA_\varphi,$$

A_φ being the toroidal component of the vector potential ($\vec{B} = \nabla\times\vec{A}$). Even though in a tokamak the toroidal field $\vec{B}_\varphi = rB_\varphi\nabla\varphi$ is dominant, the poloidal field $\vec{B}_p = \nabla\psi\times\nabla\varphi$, as will be shown, is essential for confinement. Since $\vec{B}\cdot\nabla\psi = 0$, ψ =const is a magnetic surface. In turn, Eq.(2.1) shows that magnetic and current surfaces are identical and given by $p = p(\psi)$ =const. The current flux enclosed by any toroidal line lying on a given magnetic surface is therefore constant so that by the poloidal component of Ampère's law (2.2):

$$rB_\varphi = \frac{1}{2\pi}\int_{\Gamma(r,z)} \vec{B}_\varphi\cdot d\vec{l}_\varphi = \frac{\mu_0}{2\pi}\int_{\Sigma(r,z)} \vec{j}_p\cdot d\,\vec{\sigma} = I(\psi),$$

which in differential form reads:

$$\vec{j}_p = \frac{1}{\mu_0}\nabla\times\vec{B}_\varphi = \frac{1}{\mu_0}\frac{d}{d\psi}(rB_\varphi)\,\vec{B}_p\,.$$

The toroidal component of Ampère's law leads to the so-called Grad-Shafranov equation[48]:

$$-\Delta^\star\psi \equiv -\left(\Delta - \frac{2}{r}\frac{\partial}{\partial r}\right)\psi = \frac{1}{2}\frac{d}{d\psi}(rB_\varphi)^2 + \mu_0 r^2\frac{dp}{d\psi} = \mu_0 r j_\varphi. \tag{2.4}$$

Hence, the MHD equilibrium is entirely determined after choosing a pair of independent profiles $p = p(\psi)$, $rB_\varphi = (rB_\varphi)(\psi)$ and solving (2.4) for $\psi = \psi(r,z)$.

By defining the generalized poloidal coordinate $\chi = \chi(r,z)$ independent of ψ and so that $r = r(\psi,\chi)$ and $z = z(\psi,\chi)$ are 2π periodic in χ, one obtains a new set of space variables (ψ,χ,φ), which suits the axial symmetry of the magnetic surfaces. Assuming furthermore that χ is chosen such that this system is right-hand oriented, the associated Jacobian is given by

$$J = \left[(\nabla\psi\times\nabla\chi)\cdot\nabla\varphi\right]^{-1},$$

so that $d\,\vec{r} = Jd\psi d\chi d\varphi$. For the following it is also useful to define the local orthonormal

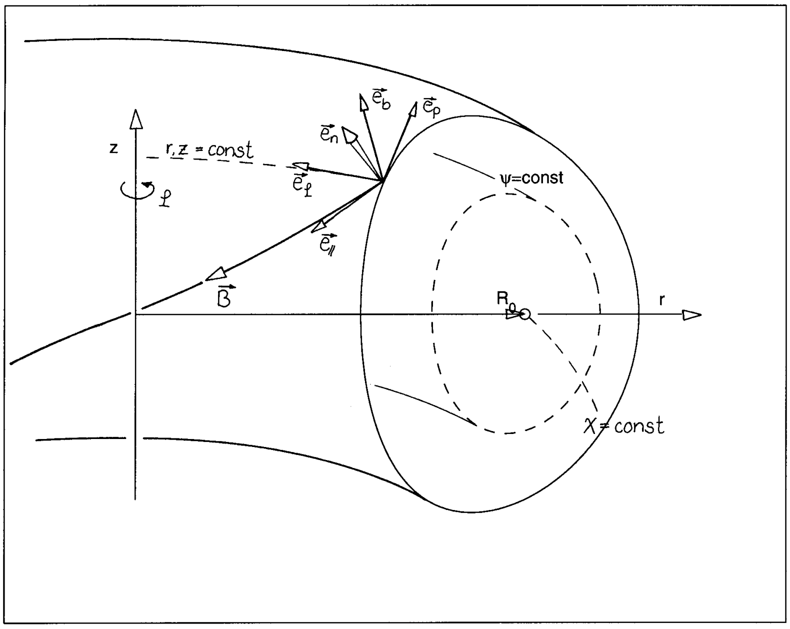

Figure 2.1: General toroidal geometry.

coordinate systems $(\vec{e_n}, \vec{e_b}, \vec{e_\parallel})$:

$$\vec{e_n} = \frac{\nabla\psi}{|\nabla\psi|}, \qquad \vec{e_\parallel} = \frac{\vec{B}}{|\,\vec{B}\,|}, \qquad \vec{e_b} = \vec{e_\parallel} \times \vec{e_n},$$

and $(\vec{e_n}, \vec{e_p}, \vec{e_\varphi})$:

$$\vec{e_p} = \vec{e_\varphi} \times \vec{e_n} \ .$$

Fig.(2.1) illustrates these notations and shows how the combined effect of toroidal and poloidal fields produce a twisting of the magnetic field lines around the magnetic surfaces. The number of toroidal revolutions of such a line to complete one poloidal revolution is given by the safety factor

$$q_s(\psi) = \frac{1}{2\pi}\int_0^{2\pi} d\chi \left|\frac{d\varphi}{d\chi}\right| = \frac{1}{2\pi}\int_0^{2\pi} d\chi \frac{JB_\varphi}{r}.$$

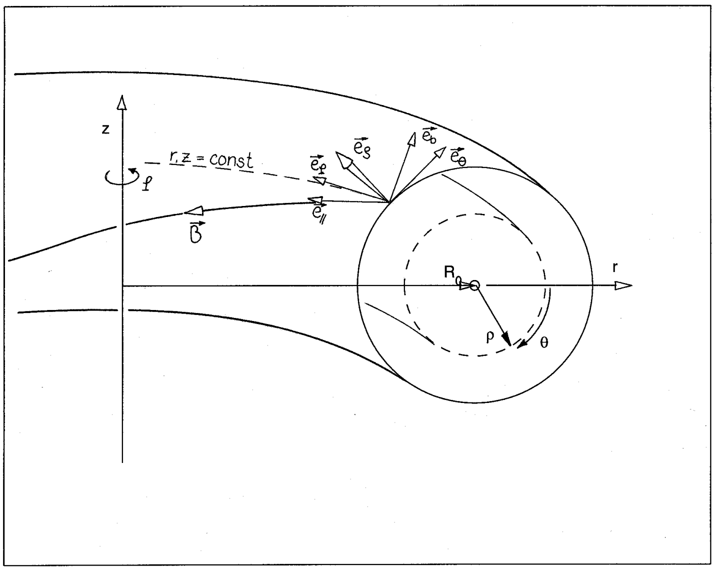

Figure 2.2: Circular, large aspect ratio geometry.

2.1.1 Circular, Large Aspect Ratio Tokamak

For analytical purposes, it is of interest to have an explicit solution of the Grad-Shafranov equation. A Solovev type[49] is obtained for rB_φ =const and $p \sim \psi$:

$$\psi = \frac{\psi_s}{(Ra)^2}\left[(rz)^2 + \frac{1}{4}(r^2 - R^2)^2\right], \tag{2.5}$$

where R stands for the major radius, a for the minor radius and ψ_s the poloidal flux on the plasma surface. In the limit of a large aspect ratio $R/a \gg 1$, (2.5) reduces to $\psi = \psi_s(\rho/a)^2$, i.e. magnetic surfaces have a circular cross-section, and the corresponding magnetic field has the simple form

$$\vec{B} = B_0\frac{R}{r}\left(-\frac{\rho}{Rq_s}\,\vec{e_\theta} + \vec{e_\varphi}\right), \tag{2.6}$$

(ρ, θ, φ) being the standard toroidal variables (see Fig.2.2). In this limit the safety factor $q_s = |\rho B_\varphi / R B_p|$ is a constant. However, the magnetic shear

$$\hat{s} = \frac{d\ln q_s}{d\ln\sqrt{\psi/\psi_s}},$$

is an important element with respect to microinstabilities. As a model, (2.6) is therefore considered with an ad-hoc profile $q_s = q_s(\rho)$ and will be often referred to for obtaining estimates valid in most tokamak configurations. But let us point out that such an equilibrium contains no finite pressure effects such as the Shafranov shift or the digging of a magnetic well through the diamagnetic behavior of the plasma, as well as no shaping effects such as elongation or triangularity. When considering this circular, large aspect ratio geometry, only lowest order terms in an expansion with respect to the inverse aspect ratio $A^{-1} = \rho/R$ are kept so that for example the magnitude of the magnetic field is approximated by

$$B = B_0(1 - A^{-1}\cos\theta), \tag{2.7}$$

and the parallel unit vector by

$$\vec{e_\|} = -\frac{A^{-1}}{q_s}\,\vec{e_\theta} + \vec{e_\varphi}\ . \tag{2.8}$$

2.2 Guiding Center Theory

To get a better understanding of magnetic confinement, it is instructive to consider the trajectory of a single independent particle. In a fusion-type plasma the magnetic field is typically of the order $B \simeq 5$Tesla so that the corresponding cyclotron frequencies $\Omega = qB/m$ for hydrogen ions and electrons are

$$\Omega_i \simeq 5 \cdot 10^8 s^{-1}, \qquad \Omega_e \simeq 9 \cdot 10^{11} s^{-1}.$$

For a temperature $T \simeq 10keV$ these particles have a thermal velocity $v_{th} = \sqrt{T/m}$:

$$v_{th\,i} \simeq 10^6 m/s, \qquad v_{th\,e} \simeq 4 \cdot 10^7 m/s,$$

and the average Larmor radius $\lambda_L = v_{th}/\Omega$ is then respectively

$$\lambda_{L\,i} \simeq 2 \cdot 10^{-3} m, \qquad \lambda_{L\,e} \simeq 4 \cdot 10^{-5} m.$$

These values are orders of magnitude smaller then the characteristic length of equilibrium such as the minor radius $a \simeq 1m$. Under these conditions a particle's trajectory can be decomposed over three time scales: The fast Larmor gyration, the slower motion parallel to the magnetic field of the center of rotation, or guiding center (GC), and the even slower GC drifts across the magnetic field. This situation is formulated rigorously by guiding center theory which in its general form considers time varying electromagnetic fields $(\vec{E}\,(\vec{r},t), \vec{B}\,(\vec{r},t))$. The ordering applied for deriving the GC trajectories is given in terms of a small parameter ϵ. The assumption that the fields are slowly varying in space and time reads

$$\frac{\lambda_L}{L} \sim \epsilon, \qquad \frac{\omega}{\Omega} \sim \epsilon,$$

where L is either the characteristic length of static fields or the wavelength of time dependent electromagnetic fields and ω a characteristic frequency. Furthermore, the electric force is considered small as compared with the magnetic force

$$\frac{|\,\vec{E}\,|}{v_{th}|\,\vec{B}\,|} \sim \epsilon.$$

The GC is then well defined and its equation of motion, independent of the gyroangle α, is given by the first order differential equations valid to order $O(\epsilon)$ [50]

$$\frac{d\vec{R}}{dt} = v_\parallel \vec{e_\parallel} + \frac{\vec{E} \times \vec{e_\parallel}}{B} + \frac{1}{\Omega} \vec{e_\parallel} \times \left[\mu \nabla B + v_\parallel^2 \vec{e_\parallel} \cdot (\nabla \vec{e_\parallel})\right], \tag{2.9}$$

$$\frac{d\mathcal{E}}{dt} = \frac{q}{m}\frac{d\vec{R}}{dt} \cdot \vec{E} + \mu \frac{\partial B}{\partial t}, \tag{2.10}$$

where $\vec{R}$ is the guiding center position and $\mathcal{E} = v^2/2$ the kinetic energy. The magnetic moment $\mu = v_\perp^2/2B$ is the adiabatic invariant related to the periodic gyromotion so that

$$\frac{d\mu}{dt} = 0.$$

Relation (2.9) shows explicitly how the GC velocity is divided into a parallel motion of order zero and perpendicular drifts of order ϵ. These drifts are all of the form

$$\vec{v}_d = \frac{\vec{f} \times \vec{e_\parallel}}{qB}, \tag{2.11}$$

where $\vec{f}$ is either the electric force $\vec{f}_e = q \vec{E}$, or the force acting on the magnetic moment in a gradient of the magnetic field $\vec{f}_\mu = -m\mu\nabla B$, or still the centrifugal force $\vec{f}_c = -mv_\parallel^2 \vec{e}_\parallel \cdot(\nabla \vec{e}_\parallel)$ related to the curvature of the magnetic lines. Charge independent forces such as $\vec{f}_\mu$ and $\vec{f}_c$ induce drifts in opposite directions for electrons and ions. However charge dependent forces such as $\vec{f}_e$ induce charge independent drifts. Note furthermore that all the considered forces and corresponding drifts are independent of mass on average.

When considering the GC orbits in the magnetostatic field of a plasma equilibrium Rel.(2.9) reads

$$\frac{d\vec{R}}{dt} = \vec{v}_g = v_\parallel \vec{e}_\parallel + \frac{1}{\Omega}\left(\frac{v_\perp^2}{2} + v_\parallel^2\right) \vec{e}_\parallel \times \nabla \ln B, \tag{2.12}$$

where the drifts relative to gradients and curvature of the magnetic field have been combined assuming a low pressure plasma and using the following relation easily derived from MHD equilibrium:

$$\vec{B} \cdot (\nabla \vec{B}) = \nabla(\frac{1}{2}B^2 + \mu_0 p).$$

In this case (2.10) simply states that kinetic energy is conserved.

2.3 Circulating and Trapped Particles

Let us now come back to the tokamak configuration. To lowest order a GC follows the magnetic field line with velocity $v_\parallel = \pm\sqrt{2(\mathcal{E} - B\mu)}$. As the lines twist round the magnetic surface due to the small poloidal component, the particles are brought from the low field in the outside region of the torus towards the high field in the inside region. Magnetic moment and kinetic energy being both conserved here, the parallel velocity decreases in this process to the point that some particles are reflected and stay trapped in the low field region, oscillating along the magnetic line. The other particles having sufficiently small values of μ overcome this barrier and continue following the line in the same direction. In this context it is convenient to define the dimensionless variable $\lambda = \mu B_0/\mathcal{E}$ which is also a constant of motion and allows one to classify these two groups of particles:

$$\begin{aligned} &\text{circulating particles:} \quad && 0 < \lambda < \frac{B_0}{B_{max}}, \\ &\text{trapped particles:} \quad && \frac{B_0}{B_{max}} < \lambda < \frac{B_0}{B} < \frac{B_0}{B_{min}}, \end{aligned}$$

$B(\psi, \chi)$ being the magnetic field at the point of interest, $B_{min,max}(\psi)$ the minimum respectively maximum value on the considered magnetic surface and B_0 the value on the magnetic axis taken as a normalization. For a trapped particle with a given value of λ the turning point angles χ_1 and χ_2 in the poloidal plane are solution of

$$\frac{B(\psi, \chi_{1,2})}{B_0} = \frac{1}{\lambda}.$$

In the following all terms relative to circulating particles are labeled 't', which stands for 'transit', all terms relative to trapped particles labeled 'b' for 'bounce'.

The angle Γ between the particle velocity $\vec{v}$ and the field $\vec{B}$ is referred to as the pitch angle and is related to λ at a given point (ψ, χ) by

$$\sin^2 \Gamma = \frac{B(\psi, \chi)}{B_0} \lambda.$$

The critical pitch angle Γ_c separating trapped from circulating particles therefore reads

$$\Gamma_c = \arcsin \sqrt{\frac{B(\psi, \chi)}{B_{max}(\psi)}}.$$

Assuming an isotropic velocity distribution, one can then easily estimate the fraction α_b of trapped particles at a given point in the plasma:

$$\alpha_b \simeq \sqrt{1 - \frac{B(\psi, \chi)}{B_{max}(\psi)}}.$$

From (2.7), $B_{max,min} = B_0(1 \pm A^{-1})$ so that in the low field region $\alpha_b \simeq \sqrt{2A^{-1}}$. For an aspect ratio $A = 10$ this corresponds to 45% of the particles.

When taking into account drifts, the GC travel across the magnetic surfaces. Indeed, in most toroidal equilibria B is proportional to $1/r$ as illustrated by (2.6), so that drifts are essentially vertical:

$$\vec{v}_d \simeq \frac{1}{\Omega}\left(\frac{v_\perp^2}{2}+v_\parallel^2\right)\frac{1}{R}\,\vec{e}_z\ . \tag{2.13}$$

However, in the absence of collisions the combined effect of poloidal rotation and vertical drifts lead to closed trajectories in the poloidal plane. This can be proved by reminding that due to the symmetry of the system φ is a cyclic variable and the conjugated momentum $\psi_0 = \psi + mrv_\varphi/q$ is also an invariant. The conservation of $\mathcal{E}$, μ and the gyroaveraged momentum $< \psi_0 >$ entirely define the GC orbit in the poloidal plane, which is closed if the magnetic surfaces are closed. Thus owing to the poloidal field and the symmetry of the system, one can guarantee the existence of long time confined orbits. Fig.(2.3) illustrates the different possible trajectories (dashed lines) for positively charged particles leaving the same point P on a given magnetic surface (full line) with different velocities. Starting with $v_\parallel > 0$ respectively $v_\parallel < 0$ the particles drift outward respectively inward and in both cases can be either trapped or untrapped. Particles of the same mass but opposite electric charge follow the same orbits but in opposite direction. Due to their characteristic shape trapped orbits are also called banana orbits. For circulating particles to perform a full revolution in the poloidal plane they must travel the distance $2\pi R q_s$ along the field line. An estimate of the corresponding frequency ω_t, called transit frequency, is thus given by

$$\omega_t \sim \frac{v_{th}}{Rq_s}.$$

As the GC drifts are of order $v_d \sim v_{th}\lambda_L/R$, one obtains for the radial excursion

$$\lambda_t \sim \frac{v_d}{\omega_t} \sim \lambda_L q_s.$$

In appendix B it is shown that the corresponding estimates for trapped particles must be weighted by a factor $\sqrt{A^{-1}}$. Thus the bounce frequency is of the order

$$\omega_b \sim \sqrt{A^{-1}}\frac{v_{th}}{Rq_s},$$

and the banana width:

$$\lambda_b \sim \frac{\lambda_L q_s}{\sqrt{A^{-1}}}.$$

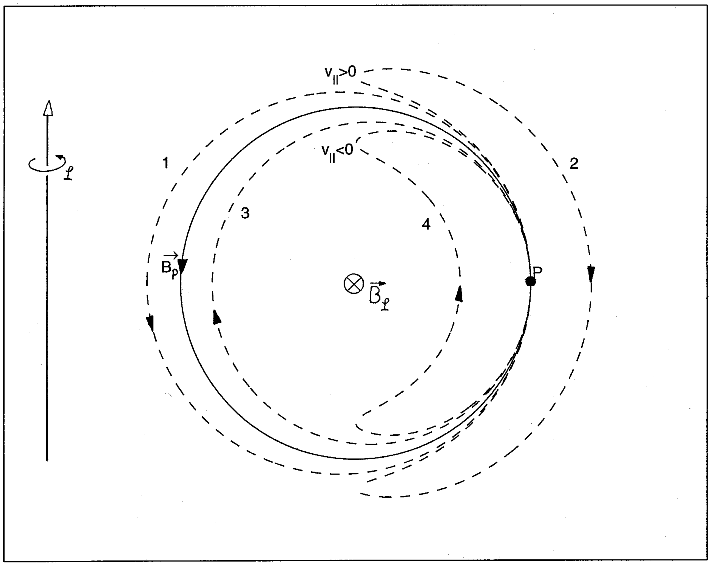

Figure 2.3: Trajectories in the poloidal plane of GC starting at point P with different velocities. In the case of positively charged particles, trajectories 1 & 2 correspond to initial conditions with $v_\parallel > 0$ and trajectories 3 & 4 to $v_\parallel < 0$. 1 & 3 are the orbits of circulating particles, 2 & 4 the banana orbits of trapped particles.

In fact after having completed a full orbit in the poloidal plane a trapped particle in general does not return exactly to the same point along φ. The toroidal drift $<\dot{\varphi}>$ which results can be expressed in terms of the longitudinal adiabatic invariant $I_\parallel = \oint dl_\parallel v_\parallel$, related to the periodic motion of the GC along the magnetic field line:

$$<\dot{\varphi}> = -\frac{m}{q}\frac{\partial I_\parallel/\partial\psi}{\partial I_\parallel/\partial\mathcal{E}}. \tag{2.14}$$

This relation is derived in appendix C and evaluated in the particular case of a circular, large aspect ratio torus which allows one to give the rough estimate

$$R <\dot{\varphi}> \sim v_{th}\frac{\lambda_L}{R}\frac{q_s}{A^{-1}} \sim v_d\frac{q_s}{A^{-1}},$$

which again is of the same order for electrons and ions. It is to be noted that this precessional drift arises even in the absence of magnetic shear in which case positively (resp. negatively) charged particles drift mainly against (resp. along) the toroidal field $\vec{B}_\varphi$. This situation can be reversed in the case of a very negatively sheared field.

2.4 Diamagnetic Drifts

A particular feature of a magnetized plasma is the presence of average drifts resulting from the interplay between spatial inhomogeneities and the finiteness of the Larmor radius. One must point out that these so-called diamagnetic drifts are not an effect of the individual GC drifts discussed above. This can easily be illustrated by considering a plasma in a uniform magnetic field $\vec{B}$ in which case particles are submitted to no drifts. Let us set the orthonormal right handed system $(\vec{e_x}{=}\vec{e_n}, \vec{e_y}{=}\vec{e_b}, \vec{e_\parallel})$. For the distribution function $F(\vec{r}, \vec{v})$ of a given species to be stationary it must be function of the constants of motion. Hence, besides the $\mathcal{E}$ dependence, F is chosen function of the GC position $X = x + v_y/\Omega$ along $\vec{e_x}$ so as to obtain density and temperature inhomogeneities:

$$F(\vec{r}, \vec{v}) = F_M(X, \mathcal{E}) = \frac{N(X)}{(2\pi T(X)/m)^{3/2}} \exp -\frac{\mathcal{E}}{T(X)/m}. \tag{2.15}$$

Thus to zero order in Larmor this form is a Maxwellian distribution with density $N(X)$ and temperature $T(X)$. Expanding to first order in Larmor:

$$F = \left[1 + \frac{v_y}{\Omega}\left(\frac{d\ln N}{dx} + \frac{dT}{dx}\frac{\partial}{\partial T}\right)\right] F_M(x, \mathcal{E}) + O(\epsilon^2).$$

Integrating to obtain the average velocity gives

$$\vec{V_d} \simeq \frac{1}{N}\int d\,\vec{v}\; F\; \vec{v} = \frac{1}{qB}\frac{1}{N}\frac{d(NT)}{dx}\;\vec{e_y} = -\frac{\nabla p}{N} \times \frac{\vec{e_\parallel}}{qB}. \tag{2.16}$$

Note that (2.16) is again of the form (2.11) but here $\vec{f} = -\nabla p/N$ is the macroscopic force related to pressure gradients.

2.5 Kinetic Models for Microinstabilities

It will be shown in the following sections that although simple fluid limits can give a first understanding of microinstabilities, these are affected by specifically kinetic mechanisms such as Landau damping or finite Larmor radius (FLR) effects. For this reason, even with the sole aim of deriving the appropriate fluid equations, kinetic equations are necessary as a starting point.

The basic equation for the kinetic description of a collisionless plasma is the Vlasov equation:

$$\frac{D}{Dt}f = \left[\frac{\partial}{\partial t} + \vec{v}\cdot\frac{\partial}{\partial\vec{r}} + \frac{q}{m}(\vec{E} + \vec{v}\times\vec{B})\cdot\frac{\partial}{\partial\vec{v}}\right]f = 0,$$

where $f(\vec{r}, \vec{v}; t)$ is the distribution function of a given species of mass m and electric charge q, and $(\vec{E}(\vec{r}, t), \vec{B}(\vec{r}, t))$ the self-consistent electromagnetic fields. This implies that in full generality one must solve over time the non-linear Vlasov-Maxwell system in the six-dimensional phase space $(\vec{r}, \vec{v})$. This problem can naturally be reduced by restricting our study to ITG-type microinstabilities and taking advantage of certain scaling relations which then appear. Defining the small parameter

$$\epsilon = \frac{\lambda_{L\,i}}{a}, \tag{2.17}$$

where here $\lambda_{L\,i}$ is specifically the ion Larmor radius and a again a characteristic length of equilibrium, these relations are summarized by what is called gyro-ordering:

$$\frac{\omega}{\Omega_i} \sim \epsilon^1, \tag{2.18}$$

$$k_\parallel\lambda_{L\,i} \sim \epsilon^1, \tag{2.19}$$

$$k_\perp\lambda_{L\,i} \sim \epsilon^0, \tag{2.20}$$

with $(\vec{k}, \omega)$ a typical wave vector-frequency pair. The justification for these relations appears throughout the description of ITG-related instabilities.

2.5.1 Gyrokinetic Equation for Ions

Let us first consider the case of ions. Except for (2.20) gyro-ordering would be appropriate for a direct application of guiding center theory. However this third relation states that the considered modes can contain perpendicular wavelengths down to the scale of the ion Larmor radius. The problem of considering this feature while at the same time taking advantage, as possible, of guiding center theory is solved by gyrokinetic theory. In appendix A the linearized gyrokinetic equation (GKE) for electrostatic perturbations is derived from the Vlasov equation [12]:

$$\left.\frac{D}{Dt}\right|_{u.t.g.} \tilde{g} = \left(\frac{\partial}{\partial t} + \vec{v}_g \cdot \frac{\partial}{\partial \vec{R}}\right) \tilde{g} = \left[\frac{q}{T} F_M \frac{\partial}{\partial t} + \left(\nabla_n F_M\right) \frac{1}{B} \nabla_b\right] < \phi > . \tag{2.21}$$

Here $\tilde{g} = \tilde{f} + qF_M\phi/T$ is the non-adiabatic part of the perturbed distribution function $\tilde{f}$ and $< \phi >$ the gyroaveraged electrostatic potential. F_M is the stationary distribution function chosen as a local Maxwellian with density N and temperature T similar to (2.15), i.e. to zero order in the Larmor radius F_M must be constant on a magnetic surface. In appendix A the proof is given for an axisymmetric system, but in fact this equation is valid for other geometries. This equation is written in gyrokinetic variables $(\vec{R}, \mathcal{E}, \mu, \alpha, \sigma = \mathrm{sign}(v_\parallel))$, with $\vec{R} = \vec{r} + \vec{v} \times \vec{e_\parallel} /\Omega$ the guiding center, $\mathcal{E}$ the kinetic energy, μ the magnetic moment and α the gyroangle defined by $\vec{v} = v_\perp(\cos\alpha\, \vec{e_n} + \sin\alpha\, \vec{e_b}) + v_\parallel\, \vec{e_\parallel}$. Although one solves for the particle distribution, the GKE has taken full advantage of guiding center theory as $\left.\frac{D}{Dt}\right|_{u.t.g.}$ stands for the total time derivative along the unperturbed trajectories of the GC, $\vec{v}_g$ being given by (2.12). Using a plane wave decomposition:

$$\phi(\vec{r}) = \int d\,\vec{k}\; e^{i\vec{k}\cdot\vec{r}}\; \hat{\phi}\,(\vec{k}),$$

the gyroaveraged potential can be written

$$< \phi > (\vec{R}, \mathcal{E}, \mu) = \int d\,\vec{k}\; J_0\left(\frac{k_\perp v_\perp}{\Omega}\right) e^{i\vec{k}\cdot\vec{R}}\; \hat{\phi}\,(\vec{k}).$$

Note the Bessel function having argument $\sim k_\perp \lambda_L$, which is the central term taking into account FLR effects.

2.5.2 Adiabatic Electrons

In first approximation the mobile electrons can be considered to respond adiabatically to the low frequency microinstabilities and therefore follow a Boltzmann distribution:

$$n = N \exp -\frac{q\phi}{T} = N\left(1 - \frac{q\phi}{T}\right) + O(\phi^2).$$

However, as already discussed, in the non trivial tokamak geometry the trapped particles have a precessional drift which can become comparable to the phase velocity of the perturbation. To take into account the resonances which may arise, a more detailed description must be given for electrons.

2.5.3 Bounce-Averaged Drift Kinetic Equation for Trapped Electrons

For similar temperatures the average electron Larmor radius λ_{Le} is smaller then λ_{Li} by a factor $\sqrt{m_e/m_i}$ and therefore is usually negligible to all considered wavelengths. For this reason, contrary to ions, it is justified to identify these particles to their GC. The corresponding equation to Vlasov for the GC is given by the drift kinetic equation (DKE)[50]

$$\left(\frac{\partial}{\partial t} + \frac{d\vec{R}}{dt} \cdot \frac{\partial}{\partial \vec{R}} + \frac{d\mathcal{E}}{dt} \frac{\partial}{\partial \mathcal{E}} \right) f_g = 0, \tag{2.22}$$

$f_g(\vec{R}, \mathcal{E}, \mu; t)$ being the GC distribution function. With $d\vec{R}/dt$ and $d\mathcal{E}/dt$ given by (2.9)- (2.10), this equation is in its non-linear form. It turns out that the perturbation frequencies ω are much smaller (again by a factor $\sqrt{m_e/m_i}$) then the average bounce frequency ω_{be} of electrons. Thus, as the GKE and DKE have been derived to get rid of the fast cyclotron time scale using gyroaveraging, a similar procedure can be undertaken with respect to this second periodicity. This is performed in Appendix C where the bounce-averaged drift kinetic equation linearized for electrostatic perturbations is obtained [51]:

$$\left(\frac{\partial}{\partial t} + <\dot{\varphi}> \frac{\partial}{\partial \varphi} \right) \tilde{g}_g = \left(\frac{q}{T} F_M \frac{\partial}{\partial t} - \nabla_n F_M \frac{1}{B_p} \nabla_\varphi \right) < \phi >_b, \tag{2.23}$$

with $\tilde{g}_g = \tilde{f}_g + qF_M\phi/T$ the non-adiabatic part of the perturbed guiding center distribution function $\tilde{f}_g$, $<\dot{\varphi}>$ the toroidal precessional drift given by (2.14) and $< \phi >_b$ the bounce-averaged potential.

2.5.4 Closure Through Quasineutrality

As we shall be essentially dealing with electrostatic instabilities the system must be closed with one equation for ϕ. In fusion type plasmas typical particle densities are of the order $N \simeq 10^{20} m^{-3}$ so that

$$\Omega_i \ll \omega_p \simeq 6 \cdot 10^{11} s^{-1}, \qquad \text{and} \qquad \lambda_{L\,i} \gg \lambda_D \simeq 1 \cdot 10^{-4} m,$$

where $\omega_p^2 = N e^2 / m_e \epsilon_0$ is the plasma frequency squared and $\lambda_D = v_{th\,e}/\omega_p$ the Debye length. It then follows from gyro-ordering that microinstabilities verify

$$\omega \ll \omega_p, \qquad \text{and} \qquad |\vec{k}| \lambda_D \ll 1.$$

This scaling allows to replace Maxwell's equations, which for electrostatic perturbations reduce to the Poisson's equation, by the quasineutrality condition. In other words, at each point there appears essentially no internal charge displacement:

$$\rho_q^{int}(\vec{r}, t) = e\left(n_i(\vec{r}, t) - n_e(\vec{r}, t)\right) \simeq 0, \tag{2.24}$$

n_e and n_i being respectively the electron and ion densities and assuming singly charged ions. This is in particular true at equilibrium where both species have same density $N(\vec{r})$.

2.6 Slab-ITG Instability

To get a first understanding of the destabilizing effects of ion temperature gradients (ITG), the system is again simplified to a slab configuration, as the one already introduced in Sec.2.4, so that all toroidal effects are put aside. By considering a single plane wave component

$$\phi = \overset{\wedge}{\phi} e^{i(\vec{k} \cdot \vec{r} - \omega t)},$$

a local dispersion relation can be established. The GKE for ions is trivial to solve as the GC trajectories reduce to the parallel motion:

$$\tilde{g}_i = \frac{e}{T_i} \frac{\omega - \omega_i^\star}{\omega - k_\parallel v_\parallel} F_{Mi} J_0\left(\frac{k_\perp v_\perp}{\Omega_i}\right) \overset{\wedge}{\phi} e^{i(\vec{k} \cdot \vec{R} - \omega t)},$$

with

$$\omega^\star = \omega_n(1 + \eta T\partial/\partial T) \qquad \text{and} \qquad \eta = d\ln T/d\ln N.$$

The diamagnetic drift frequencies related to density and temperature gradients are respectively given by

$$\omega_n = \frac{T}{qB}\frac{d\ln N}{dx}k_y \qquad \text{and} \qquad \omega_T = \eta\omega_n = \frac{1}{qB}\frac{dT}{dx}k_y.$$

By analogy to the toroidal configuration, let us assume that in the standard case N and T decrease along $\vec{e_x}=\vec{e_n}$ so that one defines the characteristic lengths

$$L_n = -(\frac{d\ln N}{dx})^{-1}, \qquad \text{and} \qquad L_T = -(\frac{d\ln T}{dx})^{-1}.$$

Going back to particle variables, that is replacing the factor $\exp i\vec{k}\cdot\vec{R}$ by $\exp i\vec{k}\cdot(\vec{r} + \vec{v}\times\vec{e_\parallel}/\Omega_i)$, the ion density can be evaluated:

$$\tilde{n_i}= \int d\vec{v}\tilde{f_i}= -\frac{Ne}{T_i}\left\{1 - \int d\vec{v}\, J_0^2\left(\frac{k_\perp v_\perp}{\Omega_i}\right)\frac{\omega-\omega_i^\star}{\omega - k_\parallel v_\parallel}\frac{F_{Mi}}{N}\right\}\phi, \tag{2.25}$$

with $d\vec{v}= 2\pi v_\perp dv_\perp dv_\parallel$, the integration over the gyroangle α having produced a second Bessel function J_0. Note the term $-Nq\phi/T$ corresponding to the adiabatic response. The integrals with respect to $v_\perp$ and $v_\parallel$ can be expressed in terms of the scaled modified Bessel function $\Lambda_p(x) = e^{-x}I_p(x)$ and the plasma dispersion function $W(z)$ [52]:

$$W(z) = \frac{1}{\sqrt{2\pi}}\int_{-\infty}^{+\infty}\frac{x}{x-z}\exp(-\frac{x^2}{2})dx \quad , \quad \Im m(z) > 0. \tag{2.26}$$

Considering adiabatic electrons, the quasineutrality relation (2.24) gives the dispersion relation

$$\begin{aligned} 0 &= \frac{1}{\tau} + 1 + \left(1 - \frac{\omega_i^\star}{\omega}\right)(W-1)\Lambda_0 \qquad (2.27)\\ &= \frac{1}{\tau} + 1 + \left[1 - \frac{\omega_{ni}}{\omega}\left(1-\frac{\eta_i}{2}\right)\right](W-1)\Lambda_0 - \frac{\omega_{ni}}{\omega}\eta_i\left[\frac{z_i^2}{2}W\Lambda_0 + (W-1)\xi_i(\Lambda_1 - \Lambda_0)\right], \end{aligned}$$

using the notations $\tau = T_e/T_i$ for the temperature ratio, $\Lambda_p = \Lambda_p(\xi_i)$, $W = W(z_i)$, $\xi = (k_\perp\lambda_L)^2$, and $z = \omega/|k_\parallel|v_{th}$. Details of similar calculations are given in chapter 3.

When normalizing the frequency with respect to $v_{th\,i}/L_n$ the independent parameters are τ, η_i, $\overset{\sim}{k_\perp} = k_\perp \lambda_{L\,i}$ and $\overset{\sim}{k_\parallel} = k_\parallel L_n$.

Let us first consider cold ions. In this limit, with the help of the asymptotic expansion $W(z) = -1/z^2 - 3/z^4 - 15/z^6 - \ldots$ one can easily derive

$$\left[1 + (k_\perp \lambda_L^\star)^2\right] \omega^2 - \omega\omega_{ne} - (k_\parallel c_s)^2 = 0, \tag{2.28}$$

where $c_s^2 = T_e/m_i$ is the sound velocity squared and $\lambda_L^\star = c_s/\Omega_i$ the ion Larmor radius evaluated with the electron temperature. Note the perpendicular dispersion from the polarization drift which is the remaining FLR effect of ions in this limit. For $|k_\parallel c_s| \gg |\omega_{ne}|$ this relation yields

$$\omega^2 \simeq \frac{(k_\parallel c_s)^2}{1 + (k_\perp \lambda_L^\star)^2},$$

which is the ion-acoustic or sound wave. For $|k_\parallel c_s| \ll |\omega_{ne}|$ one of the two roots becomes

$$\omega \simeq \omega_{ne}.$$

This is the electron drift mode which can be destabilized by non-adiabatic electron dynamics.

In the case of a finite, inhomogeneous ion temperature $T_i \simeq T_e$ an ion driven instability can arise. This can be shown by first assuming $1/|z_i| = |k_\parallel v_{th\,i}/\omega| \ll 1$ and retaining in (2.27) terms up to second order in $1/|z_i|$. Furthermore neglecting FLR effects and considering a flat density profile gives

$$1 - \left(\frac{k_\parallel v_{th\,i}}{\omega}\right)^2 \left(1 - \frac{\omega_{Ti}}{\omega}\right) = 0. \tag{2.29}$$

For $|k_\parallel v_{th\,i}| \ll \omega_{Ti}$ this relation contains an unstable root $\omega = \omega_r + i\gamma$, $\gamma > 0$ referred to as the slab-ITG instability or η_i-instability:

$$\omega \simeq \frac{1}{2}(1 + i\sqrt{3}) \left[(k_\parallel v_{th\,i})^2 \omega_{Ti}\right]^{1/3},$$

and at the limit of applicability of this result $\omega_r \simeq \gamma \simeq \omega_{Ti}$. In fact maximal growth rates appear for longitudinal phase velocities of the order $v_{th\,i}$ and perpendicular wavelengths

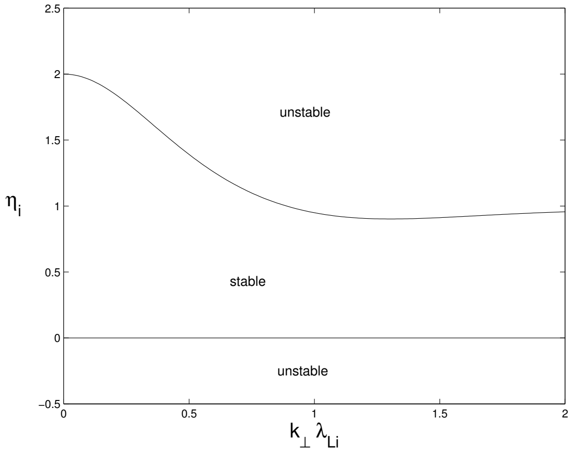

Figure 2.4: Critical value of η_i as a function of $k_\perp\lambda_{L\,i}$ for the slab-ITG instability.

of the order $\lambda_{L\,i}$ so that accurate results can only be obtained by solving the full kinetic dispersion relation (2.27). At finite values of η_i one can show that there are two conditions of instability. One is on η_i itself, which for arbitrary values of $k_\perp\lambda_{L\,i}$ reads [53]

$$\eta_i > \eta_{ic} = \frac{2}{1+2\xi_i(\Lambda_0-\Lambda_1)/\Lambda_0} \qquad \text{or} \qquad \eta_i < 0, \tag{2.30}$$

illustrated in Fig.2.4. The other condition as we have already seen is on $k_\parallel$:

$$|k_\parallel| < k_{\parallel\,\mathrm{lim}},$$

where for $k_\perp\lambda_{L\,i} \ll 1$

$$k_{\parallel\,\mathrm{lim}} = \frac{1}{2}\left(1-\frac{2}{\eta_i}\right)^{1/2}\frac{|\omega_{Ti}|}{v_{th\,i}} = \frac{1}{2}\left(1-\frac{2}{\eta_i}\right)^{1/2}\frac{\lambda_{L\,i}}{|L_{Ti}|}k_y. \tag{2.31}$$

For $|k_\parallel| > k_{\parallel\,\mathrm{lim}}$ the instability is suppressed by Landau damping. Notice that $\omega_{Ti}/\Omega_i \sim k_{\parallel\,\mathrm{lim}}\lambda_{L\,i} \sim \tilde{k}_\perp\ \lambda_{L\,i}/L_{Ti} \sim \epsilon$ so that gyro-ordering assumptions are verified. As shown in Fig.2.5 and 2.6, γ and $k_{\parallel\,\mathrm{lim}}$ are both maximum for $k_\perp\lambda_{L\,i} \simeq 1$. For even shorter wavelengths the potential felt by the ions tends to be averaged out over their Larmor gyration and the drive becomes less effective.

In the next section it is shown that if toroidicity effects are not too strong, these slab-type instabilities, despite their name, can prevail in a tokamak geometry. One can

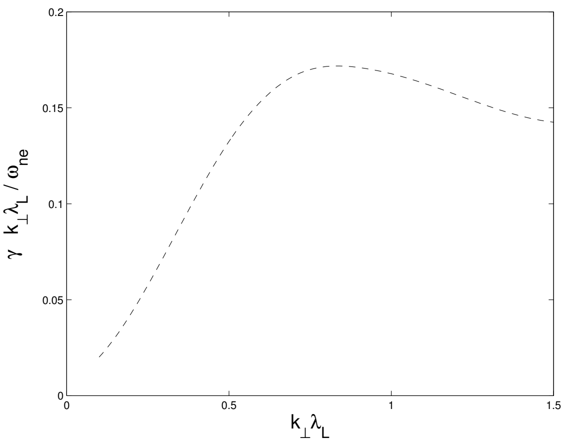

Figure 2.5: Growth rate of slab-ITG instability as a function of $k_\perp \lambda_{L\,i}$. Maximum value is near $k_\perp \lambda_{L\,i} = 1$. Here $\tau = 1$, $\eta_i = 4$ and $k_\parallel$ was varied for maximum growth rate.

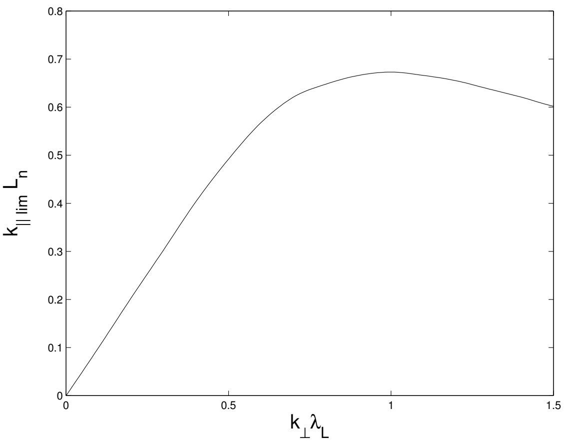

Figure 2.6: Maximum value of $k_\parallel L_n$ for slab-ITG instability as a function of $k_\perp \lambda_{L\,i}$. Here $\tau = 1$, $\eta_i = 4$.

get an idea of the structure of such an eigenmode by considering a circular cross-section equilibrium of the form (2.6). Besides having a fixed toroidal mode number n due to the symmetry of equilibrium, such a mode also contains a dominant poloidal mode number m due to the weak toroidal coupling:

$$\phi \simeq \phi(\rho) e^{i(m\theta + n\varphi)}.$$

The parallel wave number can then be obtained using (2.8):

$$\vec{e_\parallel} \cdot \nabla \phi \simeq i \frac{1}{R q_s}(n q_s - m)\phi \qquad \Longrightarrow \qquad k_\parallel(\rho) = \frac{1}{R q_s(\rho)}(n q_s(\rho) - m).$$

As $|k_\parallel| < k_{\parallel\,\mathrm{lim}}$, such a mode tends to be localized around the corresponding mode rational surface $\rho = \rho_r$ =const, where $q_s(\rho_r) = m/n$ and thus $k_\parallel(\rho_r) = 0$. At a distance $\Delta\rho$ from this surface $|k_\parallel| = \Delta\rho |k_\theta| / L_s$, with $L_s = R q_s / \hat{s}$ the shear length and $k_\theta = m/\rho$ the poloidal mode number. From (2.31) and noticing that here $\omega_T = -T k_\theta / q B_0 L_T$, one can then estimate the radial extent of such a mode for $k_\perp \lambda_{L\,i} \ll 1$:

$$\Delta\rho \simeq \frac{1}{2}\left(1 - \frac{2}{\eta_i}\right)^{1/2} \frac{L_s}{L_{T_i}} \lambda_{L\,i}. \tag{2.32}$$

The condition for two such modes with same toroidal wave number n and centered on neighboring rational surfaces to overlap is then given in the fluid regime $\eta_i \gg \eta_{ic}$ by

$$\Delta\rho \ \overset{\sim}{>} \ \frac{1}{nq'_s} \qquad \Longrightarrow \qquad \epsilon_{T_i} \ \overset{\sim}{<} \overset{\sim}{k_\theta} \, q_s,$$

with $\epsilon_T = L_T/R$, and $\overset{\sim}{k_\theta} = k_\theta \lambda_{L\,i}$. Under this condition, for a fixed toroidal wave number, many independent modes can form a fluctuating structure with a large radial extent spanning the corresponding mode rational surfaces.

2.7 Toroidal-ITG Instability

As discussed in section (2.3), when going to a toroidal system the particles are mainly affected in two ways. First, toroidicity induces a drift on all GC. Second, each species is divided into circulating and trapped particles. Here we shall neglect the distinct wave interaction in relation with trapped particle dynamics. The simplest way to model GC drifts then consists in adding an external force of the form

$$\vec{f} = m \left(\frac{v_\perp^2}{2} + v_\parallel^2 \right) \frac{1}{R} \, \vec{e}_x,$$

to the slab system introduced above. This gives rise to drifts

$$\vec{v}_d = \frac{\vec{f} \times \vec{e}_\parallel}{qB} = -\frac{1}{\Omega} \left(\frac{v_\perp^2}{2} + v_\parallel^2 \right) \frac{1}{R} \, \vec{e}_y,$$

of the same order and having similar velocity dependence as (2.13). This layout can be identified to the local configuration in the outer (poloidal angle $\theta = 0$) respectively inner (poloidal angle $\theta = \pi$) region of a torus with major radius R, depending whether the geometry factor $1/R$ is positive or negative. The GC still follow uniform rectilinear trajectories, however slightly skew with the field lines due to drifts. The local dispersion relation can again be easily derived:

$$0 = \frac{1}{\tau} + 1 - \int d\,\vec{v} \; J_0^2 \left(\frac{k_\perp v_\perp}{\Omega_i} \right) \frac{\omega - \omega_i^\star}{\omega - k_\parallel v_\parallel - \omega_{gi}} \frac{F_{Mi}}{N}, \tag{2.33}$$

with the GC drift frequency defined by

$$\omega_g = \vec{k} \cdot \vec{v}_d \ .$$

With no approximation, the velocity integrals in (2.33) cannot be expressed in terms of well-known special functions.

To get a first understanding one takes again a fluid limit by assuming $|k_\parallel v_{th\,i}/\omega| \ll 1$, $|\omega_{gi}/\omega| \ll 1$ and $k_\perp \lambda_{L\,i} \ll 1$, so that for $T_e = T_i$[22][54]:

$$1 + \frac{\omega_{ni}}{\omega} + \left[\xi_i - \left(\frac{k_\parallel v_{th\,i}}{\omega}\right)^2 - \frac{< \omega_{gi} >}{\omega}\right]\left(1 - \frac{\omega_{ni}(1+\eta_i)}{\omega}\right) = 0, \qquad (2.34)$$

where $< \omega_{gi} >$ is the average drift frequency:

$$< \omega_g > = -\frac{2T}{qB}\frac{k_y}{R} = 2\epsilon_n \omega_n,$$

using the definition $\epsilon_n = L_n/R$. For further purposes density gradients as well as ion polarization drift have been retained. However, neglecting these terms for the time being gives

$$1 - \left[\left(\frac{k_\parallel v_{th\,i}}{\omega}\right)^2 + \frac{< \omega_{gi} >}{\omega}\right]\left(1 - \frac{\omega_{Ti}}{\omega}\right) = 0,$$

which, contrary to (2.29), can provide an instability with finite growth rate down to $k_\parallel = 0$. Indeed, for $< \omega_{gi} > \ll \omega_{Ti}$ this equation then has solutions

$$\omega = \pm(- < \omega_{gi} > \omega_{Ti})^{1/2},$$

which yields an instability if $1/R$ is positive. Note that this so-called toroidal-ITG instability and the slab-ITG are different limits of the same branch. If $1/R$ is negative, GC drifts act in the opposite direction so that no instability appears around $k_\parallel = 0$. This mechanism is characteristic of an interchange instability. Hence, in a tokamak plasma these modes tend to balloon in the low-field region, also called unfavorable curvature region for this reason. In fact, as the corresponding envelope contains parallel wavelengths of the order $2\pi R q_s$, which is the distance along a magnetic field line to perform one poloidal rotation, the minimum value for $|k_\parallel|$ cannot be zero but $1/Rq_s$. An estimate whether toroidicity is sufficiently strong for the transition from slab- to the toroidal-ITG instability to occur, depends on the relative importance of

$$\left|\frac{k_\parallel v_{th\,i}}{\omega}\right|^2 \quad \gtrless \quad \left|\frac{<\omega_{gi}>}{\omega}\right|, \tag{2.35}$$

appearing in (2.34). Testing the perturbing effect of toroidicity on the slab-ITG by taking the typical frequency $\omega \simeq \omega_{Ti}$ and $|k_\parallel| \simeq 1/Rq_s$ in (2.35) gives the condition for transition to the slab-ITG:

$$\sqrt{\epsilon_{T_i}} \;\overset{\sim}{>}\; \tilde{k}_\theta\, q_s. \tag{2.36}$$

The solution to (2.34) for $k_\parallel = 0$, still neglecting polarization drift but taking into account density gradients reads

$$\omega = \frac{1}{2}\left[(<\omega_{gi}> -\omega_{ni}) \pm \sqrt{(<\omega_{gi}> -\omega_{ni})^2 - 4 <\omega_{gi}> \omega_{ni}(1+\eta_i)}\right],$$

which leads to the following condition for stability

$$8\epsilon_n(1+\eta_i) < (2\epsilon_n - 1)^2. \tag{2.37}$$

Note that for $\epsilon_n < 1/2$ the toroidal-ITG mode propagates in the electron diamagnetic direction. These fluid results are naturally only of very qualitative value, especially near marginal stability where drift resonances appearing in (2.33) become important. This is shown in Fig.2.8 where condition (2.37) is compared to the marginal stability obtained by solving numerically the kinetic dispersion relation (2.33) for $\tau = 1$, $k_\parallel = 0$ and $\tilde{k}_\perp = 0.3$. As can be seen from (2.37), for flat density the condition for stability becomes a constraint on ϵ_{T_i}. From the kinetic dispersion relation one obtains $\epsilon_{T_i} \overset{\sim}{>} 0.3$ instead of $\epsilon_{T_i} > 2$ coming from the fluid condition. Fig.2.7 illustrates FLR effects and shows how the toroidal-ITG has maximum growth rate for $k_\perp \lambda_{L\,i} \sim 0.5$, that is at definitely longer perpendicular wavelengths then the slab-ITG.

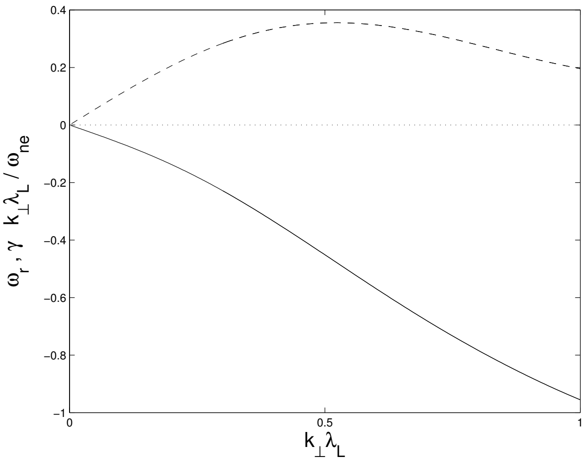

Figure 2.7: Real frequency (full line) and growth rate (dashed line) of toroidal-ITG instability as a function of $k_\perp \lambda_{Li}$. Maximum value of growth rate is near $k_\perp \lambda_{Li} = 0.5$. Here $\tau = 1$, $\epsilon_n = 0.3$, $\eta_i = 4$ and $k_\| = 0$. Note that for $\omega_r/\omega_{ne} < 0$ the mode propagates in the ion diamagnetic direction.

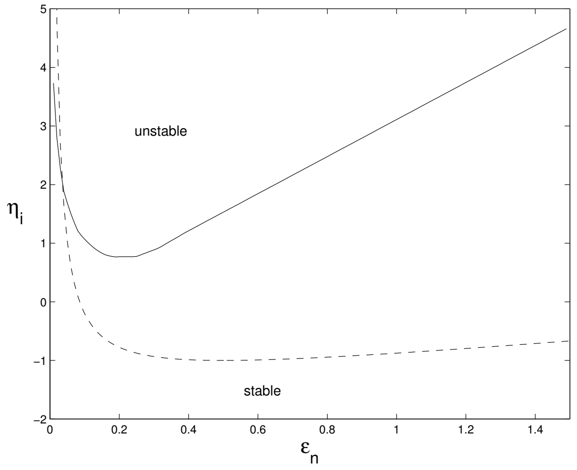

Figure 2.8: Stability curve for toroidal-ITG mode in plane (ϵ_n, η_i). Full line is obtained by numerical resolution of kinetic dispersion relation with $\tau = 1$, $k_\| = 0$, $k_\perp \lambda_L = 0.3$. Dashed line is the fluid result.

2.8 Ballooning Representation

The simple description of the toroidal-ITG instability given in the preceding section showed that this mode is interchange-like and therefore tends to be aligned with the magnetic field lines. In a general tokamak geometry, for a linear perturbation with fixed toroidal wave number n, this implies

$$\begin{aligned}
0 &\simeq \vec{e_\|} \cdot \nabla\phi \\
&= \frac{1}{B}(\nabla\psi \times \nabla\varphi + rB_\varphi \nabla\varphi) \cdot (\nabla\chi \frac{\partial}{\partial\chi} + \nabla\varphi \frac{\partial}{\partial\varphi})\phi = \left(-\frac{1}{JB}\frac{\partial}{\partial\chi} + \frac{B_\varphi}{B}\frac{in}{r}\right)\phi \\
\Longrightarrow &\ \ \phi \simeq \overset{\wedge}{\phi} \exp inS(\psi, \chi, \varphi), \qquad (2.38)
\end{aligned}$$

with

$$S = \int_0^\chi d\chi \frac{JB_\varphi}{r} + \varphi.$$

As the mode has a finite radial extension and furthermore balloons in the unfavorable curvature region, $\overset{\wedge}{\phi}$ must provide a modulation in ψ and χ. Such a form can be useful as an ansatz when considering toroidal-ITG instabilities in a true tokamak configuration. In fact, as $S(\psi, \chi + 2\pi, \varphi) = S(\psi, \chi, \varphi) + 2\pi q_s(\psi)$, Rel.(2.38) is not periodic in χ except on mode rational surfaces where $nq_s = m$ is an integer. Therefore one actually chooses the ansatz

$$\phi = \sum_{p=-\infty}^{+\infty} \overset{\wedge}{\phi}\,(\psi, \chi + p2\pi) \exp inS(\psi, \chi + p2\pi, \varphi), \tag{2.39}$$

so that no periodicity has to be enforced on $\overset{\wedge}{\phi}$ whose χ domain is the whole real axis. This so-called ballooning representation was first proposed by Connor, Hastie and Taylor[19] and put on a rigorous mathematical ground by Hazeltine and Newcomb[55] who have shown that (2.39) defines a one to one transformation if $\overset{\wedge}{\phi}$ varies sufficiently slowly from one mode rational surface to another. For high values of n let us assume that one can distinguish a fast length scale relative to the phase factor:

$$\lambda_{L\,i}|n\nabla S| \sim \epsilon^0, \tag{2.40}$$

from a slow length scale relative to the ballooning envelope:

$$\lambda_{L\,i}|\nabla \ln \overset{\wedge}{\phi}\,| \sim \epsilon^1. \tag{2.41}$$

Adopting for $\tilde{g}$ an equivalent form to (2.39) and inserting these relations in (2.21) leads to the GKE in ballooning representation, which to lowest order in ϵ is given by

$$\left[\frac{\partial}{\partial t} - \frac{v_\parallel}{JB}\frac{\partial}{\partial \chi} + i\,\vec{k}\cdot\vec{v}_d\right] \overset{\wedge}{\tilde{g}}\,(\psi, \chi; t) = \left[\frac{q}{T}F_M\frac{\partial}{\partial t} + \nabla_n F_M \frac{ik_b}{B}\right] J_0\left(\frac{k_\perp v_\perp}{\Omega}\right) \overset{\wedge}{\phi}\,(\psi, \chi; t),$$

with the notation $\vec{k} = n\nabla S$. Note that this equation is local to a magnetic surface. To obtain the radial dependence $\overset{\wedge}{\phi}\,(\psi)$ of the envelope one must work to higher order in ϵ[20]. Let us emphasize that this relation is valid only under the scaling (2.40)- (2.41) which in particular breaks down for low n. Furthermore, independent of the value of n, this representation is not adapted for instabilities having no interchange character. This is the case for the slab-ITG, which has no tendency to balloon and although having long parallel wavelengths, never aligns along the magnetic field line (i.e. $|k_\parallel/k_\perp| \ll 1$ but $k_\parallel \neq 0$).

As an illustration, let us consider the circular, large aspect ratio equilibrium. In this case the gyrokinetic ballooning equation reads

$$\left[\frac{\partial}{\partial t} - \frac{v_\parallel}{Rq_s}\frac{\partial}{\partial \theta} - ik_\theta v_{dz}(\cos\theta + \hat{s}\,\theta\sin\theta)\right]\overset{\wedge}{\tilde{g}}(\rho,\theta;t) = \left[\frac{q}{T}F_M\frac{\partial}{\partial t} + \frac{dF_M}{d\rho}\frac{ik_\theta}{B}\right]J_0\left(\frac{k_\perp v_\perp}{\Omega}\right)\overset{\wedge}{\phi}(\rho,\theta;t), \tag{2.42}$$

having used $JB = Rq_s$ and $S = q_s(\rho)\theta + \varphi$ as well as $\vec{k} \simeq k_\rho\,\vec{e_\rho} + k_\theta\,\vec{e_\theta} + n/R\,\vec{e_\varphi}$ with $k_\rho = k_\theta\,\hat{s}\,\theta$, $k_\theta = nq_s/\rho$. This relation shows explicitly how ballooning representation takes into account shear $\hat{s}$ which appears as well in the perpendicular wave number

$$k_\perp \simeq \sqrt{k_\theta^2 + k_\rho^2} = k_\theta\sqrt{1 + (\hat{s}\,\theta)^2},$$

as in the GC drift frequency $\omega_g = \vec{k}\cdot\vec{v}_d$. The system of (2.42) together with the quasineutrality equation can again be considered in the fluid limit. The corresponding equation for $\overset{\wedge}{\phi}$ can be directly obtained from the slab relation (2.34) using the following transcriptions:

$$ik_\parallel \longrightarrow \nabla_\parallel \simeq -\frac{1}{Rq_s}\frac{\partial}{\partial\theta} \tag{2.43}$$

$$k_y \longrightarrow k_\theta \tag{2.44}$$

$$< \omega_g > \longrightarrow -\frac{2T}{qB_0}\frac{k_\theta}{R}(\cos\theta + \hat{s}\,\theta\sin\theta) \tag{2.45}$$

so that

$$\left[\left(\frac{v_{th\,i}}{\omega Rq_s}\right)^2\frac{d^2}{d\theta^2} - \frac{<\omega_{gi}>}{\omega}(\cos\theta + \hat{s}\,\theta\sin\theta) + \frac{\omega + \omega_{ni}}{\omega - \omega_{ni}(1+\eta_i)} + \tilde{k}_\theta^{\,2}\left(1 + (\hat{s}\,\theta)^2\right)\right]\overset{\wedge}{\phi}(\theta) = 0, \tag{2.46}$$

where now $< \omega_g >= 2\epsilon_n\omega_n$, $\omega_{n,T} = -Tk_\theta/qB_0L_{n,T}$. On the basis of this equation Horton, Choi and Tang[5] first discussed the toroidal-ITG mode. This defines a one-dimensional eigenvalue equation for $\overset{\wedge}{\phi}(\theta)$ with a non-trivial dependence in the eigenfrequency ω.

2.9 Trapped Particle Instabilities

We will now consider how trapped particles may affect the basic ITG instabilities. If the frequency ω of a perturbation falls below the bounce frequency ω_b of a given species, trapped particles can carry out complete banana orbits over a characteristic time of evolution of the mode. The interaction of these particles with the wave can then be fundamentally different from circulating particles: not only are they localized in the low field region, but also their oscillating GC trajectories allow no parallel phase resonance. However, so-called trapped particle instabilities, driven by their toroidal precessional drift may appear[56].

It was shown that typical frequencies of the ITG-type modes are of the order

$$\omega \sim \omega^\star \sim \omega_g \sim \frac{v_{th\,i}}{a},$$

where $a \sim L_{n,T}, R$ is a characteristic length of equilibrium. This can be comparable with the ion bounce frequency $\omega_{bi} \sim \sqrt{A^{-1}} v_{th\,i}/Rq_s$. Estimating $\omega < \omega_{bi}$ with $\omega = \omega_{Ti}$ yields

$$\tilde{k}_\theta\, q_s \overset{\sim}{<} \sqrt{A^{-1}} \epsilon_{T_i}.$$

Under this condition the transition from the slab-ITG to the trapped ion mode (TIM) occurs. Together with (2.36) one can then establish the rough picture

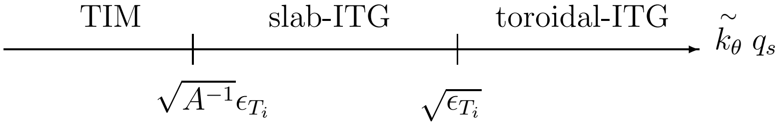

Note that when unbending the torus into a cylinder, carried out by increasing R while holding Rq_s and $\tilde{k}_\theta$ constant, the slab-ITG is indeed the only mode which remains. However, for sufficient toroidicity there may be a direct transition from the toroidal-ITG, with frequency $\omega \sim < \omega_{gi} >$, to the TIM. This situation is then summarized by

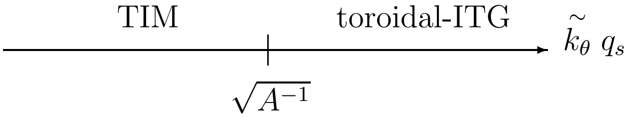

With respect to electrons however one always has $\omega \ll \omega_{be}$ in a torus:

$$\frac{\omega}{\omega_{be}} \sim \frac{1}{\sqrt{A^{-1}}}\frac{v_{th\,i}}{v_{th\,e}} \sim \frac{1}{\sqrt{A^{-1}}}\sqrt{\frac{m_e}{m_i}} \ll 1.$$

As a consequence trapped electron dynamics can affect the ITG-instability over most regimes.

To get a basic understanding of these mechanisms let us establish the contribution of non-adiabatic trapped particles to the local dispersion relations discussed above. For this purpose the bounce-averaged DKE (2.23) is suitable even for ions if FLR effects are neglected. This equation is trivial to solve and yields the non-adiabatic part of the GC distribution function of trapped particles:

$$\tilde{g}_g = \frac{q}{T}F_M\frac{\omega-\omega^\star}{\omega - n <\dot{\varphi}>} < \phi >_b,$$

where n is the fixed toroidal wave number. To obtain a zero-dimensional relation, let us approximate

$$< \phi >_b \simeq \phi.$$

This can be justified by assuming an interchange-like structure. From relation (C.7) of appendix C the precessional drift frequency is given by

$$n <\dot{\varphi}> = \frac{\mathcal{E}}{v_{th}^2}\omega_\varphi, \qquad \text{with} \qquad \omega_\varphi = \omega_n \epsilon_n G,$$

where the factor $G \sim 1$ is approximated to a constant, i.e. neglecting here its pitch angle dependence. Thus calculating the non-adiabatic trapped particle density fluctuation $\tilde{n}_b^{n.a.}$ reduces to an integration over energy:

$$\int d\,\vec{v} = 4\pi\alpha_b \int d\mathcal{E}\sqrt{2\mathcal{E}},$$

so that

$$\begin{aligned}\tilde{n}_b^{n.a.} &= 4\pi\alpha_b N\frac{q}{T}\int d\mathcal{E}\sqrt{2\mathcal{E}}\frac{F_M}{N}\frac{\omega-\omega^\star}{\omega - n <\dot{\varphi}>}\phi \\ &= -2\alpha_b N\frac{q}{T}\frac{1}{\omega_\varphi}\left[\left(\omega - \omega_n(1-\frac{3}{2}\eta)\right)W(z_b) - \omega_n\eta\left(\frac{\omega}{\omega_\varphi}W(z_b)+\frac{1}{2}\right)\right]\phi, \quad (2.47)\end{aligned}$$

where $z_b = \mathrm{sign}(\omega_\varphi)\sqrt{2\omega/\omega_\varphi}$. When deriving this relation one must be particularly careful with causality. This is related to the fact that the wave can resonate with a given species of trapped particles only if it propagates in the same direction as the precessional drift of the corresponding bananas. This is in fact similar to the GC drift resonances affecting the toroidal-ITG instability. Details of this calculation are given in chapter 5.

2.9.1 Trapped Ion Mode (TIM)

As mentioned above, this mode falls in the regime $\omega < \omega_{bi} \ll \omega_{be}$. The corresponding local dispersion relation is based as usual on the quasineutrality condition considering for each species, besides its adiabatic response, the non-adiabatic trapped particle dynamics through (2.47):

$$0 = \sum_{\text{electrons, ions}} \frac{1}{T}\left\{1 + \frac{2\alpha_b}{\omega_\varphi}\left[\left(\omega - \omega_n(1-\frac{3}{2}\eta)\right)W(z_b) - \omega_n\eta\left(\frac{\omega}{\omega_\varphi}W(z_b) + \frac{1}{2}\right)\right]\right\}.$$

Considering the limit $|\omega_\varphi/\omega| \ll 1$ and retaining lowest order terms leads to

$$0 = 1 + \alpha_b\left[-1 + \frac{3}{2}\frac{\omega_{\varphi i}\omega_{ni}(1+\eta)}{\omega^2}\right],$$

having assumed equal temperature profiles for electrons and ions so that $\tau = 1$ and $\eta_e = \eta_i \equiv \eta$. This yields the trapped ion instability driven by precessional drift in the presence of inhomogeneous temperature and density profiles[57]:

$$\gamma \simeq \sqrt{\frac{3}{2}\alpha_b\omega_{\varphi i}\omega_{ni}(1+\eta)}.$$

Similar to the toroidal-ITG instability driven by the vertical drifts of the GC, the trapped ion instability requires that the banana orbits of each species drift in the corresponding diamagnetic direction so that $\omega_n\omega_\varphi > 0$. This is usually the case as the factor G is positive except for very sheared fields.

2.9.2 Trapped Electron Mode (TEM)

This instability appears in the regime $\omega_{bi} < \omega < \omega_{be}$. As will be shown below, this mode can be strongly coupled to the toroidal-ITG instability. Therefore, to isolate the pure

TEM, let us neglect parallel ion drive by taking $k_\| v_{th\,i} = 0$ as well as perpendicular ion drive setting $\omega_{gi} = 0$ so that from (2.25)

$$\underset{\sim}{n}_i = \frac{Ne}{T_i}\frac{\omega_{ni}}{\omega},$$

having also neglected all FLR effects. The appropriate dispersion relation then reads

$$0 = \frac{1}{\tau} + \frac{1}{\tau}\frac{2\alpha_b}{\omega_{\varphi e}}\left[\left(\omega - \omega_{ne}(1-\frac{3}{2}\eta_e)\right)W(z_{be}) - \omega_{ne}\eta_e\left(\frac{\omega}{\omega_{\varphi e}}W(z_{be}) + \frac{1}{2}\right)\right] + \frac{\omega_{ni}}{\omega}.$$

Again assuming $|\omega_{\varphi e}/\omega| \ll 1$, $\tau = 1$ and retaining lowest order terms leads to

$$0 = 1 + \alpha_b\left[-1 + \frac{\omega_{ne} - 3\omega_{\varphi e}/2}{\omega} + \frac{3}{2}\frac{\omega_{\varphi e}\omega_{ne}(1+\eta_e)}{\omega^2}\right] - \frac{\omega_{ne}}{\omega},$$

giving an estimate of the trapped electron instability $\omega = \omega_r + i\gamma$ for $\eta_e >> 1$:

$$\omega_r \simeq \omega_{ne}, \qquad \gamma \simeq \sqrt{\frac{3}{2}\alpha_b\omega_{\varphi e}\omega_{ne}(1+\eta_e)}.$$

This result reveals a mode propagating in the electron diamagnetic direction and having a similar driving mechanism as the TIM.

2.9.3 Coupling of the TEM to the ITG Instability

As already mentioned, trapped electron dynamics can potentially be effective throughout all ITG-instability regimes. This can be studied by adding non-adiabatic trapped electron dynamics to the dispersion relation (2.33)

$$\begin{aligned} 0 &= \frac{1}{\tau} + \frac{1}{\tau}\frac{2\alpha_b}{\omega_{\varphi e}}\left[\left(\omega - \omega_{ne}(1-\frac{3}{2}\eta_e)\right)W(z_{be}) - \omega_{ne}\eta_e\left(\frac{\omega}{\omega_{\varphi e}}W(z_{be}) + \frac{1}{2}\right)\right] \\ &+ 1 - \int d\,\vec{v}\; J_0^2\left(\frac{k_\perp v_\perp}{\Omega_i}\right)\frac{F_{Mi}}{N}\frac{\omega - \omega_i^\star}{\omega - k_\| v_\| - \omega_{gi}}. \end{aligned} \tag{2.48}$$

Thus, depending on which drive is dominant, this dispersion relation yields an instability having either an ITG or TEM character. In an intermediate state one obtains a hybrid mode referred to as the trapped electron-η_i instability[58]. For fixed electron parameters this transition takes place near the marginal stability of the pure toroidal-ITG mode where

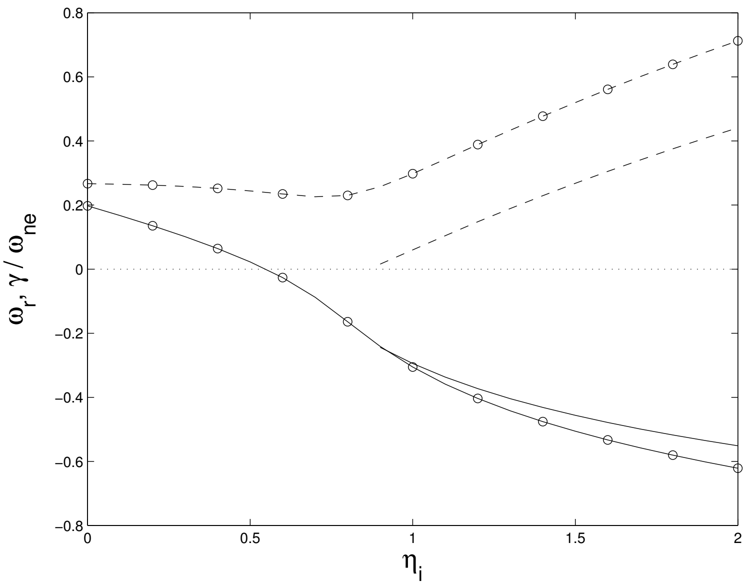

Figure 2.9: Real frequency (full line) and growth rate (dashed line) as a function of η_i. Circles label results with non-adiabatic trapped electron contribution. As a reference plain lines represent results with only the adiabatic response of these particles. Here $\tau = 1.0$, $\epsilon_n = 0.3$, $\alpha_b = 0.32$, $G = 1.0$, $\eta_e = 0.1$, $k_{\|} = 0$, $k_{\perp}\lambda_{Li} = 0.3$.

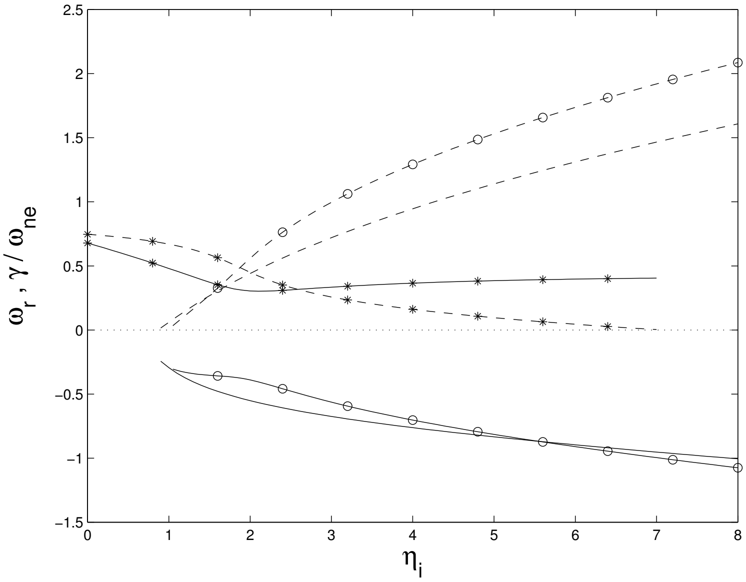

Figure 2.10: The same situation as in the previous figure except for $\eta_e = 4.0$. When considering non-adiabatic trapped electrons dynamics there is an interval in η_i were the perturbed toroidal-ITG (circles) and trapped electron mode (stars) are present simultaneously. Plain curves represent again results without trapped electrons.

ion drive becomes weak. As already mentioned, a kinetic description is necessary in this regime to take into account the resonant mechanisms. The numerical results obtained by solving (2.48) are presented in the following figures. We will essentially discuss how the toroidal-ITG is affected and therefore set $k_{\parallel} = 0$.

Fig.2.9 shows the real frequency (full line with circles) and growth rate (dashed line with circles) of the instability as a function of η_i for $\tau = 1$, $\epsilon_n = 0.3$ and $k_{\perp}\lambda_{L\,i} = 0.3$. Trapped electron parameters are $\alpha_b = 0.32$, $G = 1$ and $\eta_e = 0.1$. The toroidal-ITG with no trapped electrons is plotted as a reference with plain lines. For $\eta_i \gg \eta_{ic} \sim 1$ the instability is essentially the toroidal-ITG but with increased growth rate. However for $\eta_i < \eta_{ic}$, contrary to the pure toroidal-ITG, the hybrid mode remains unstable and starts to propagate in the electron diamagnetic direction, revealing the transition to the TEM.

In fact for $\eta_e > 2/3$ two instabilities can be present simultaneously[8][59]. This is illustrated in Fig.(2.10) for the same parameters as above except $\eta_e = 4.0$. The lines with circles represent a mode with toroidal-ITG character damped at $\eta_i = \eta_{ic} \sim 1$, the lines labeled with stars an instability with TEM character remaining unstable for $\eta_i < \eta_{ic}$. Hence, non-adiabatic electron dynamics can greatly alter the stability picture one had from the pure toroidal-ITG.

Fig.2.11 and Fig.2.12 present the stability curves of the trapped electron-η_i mode (full line) in the plane (ϵ_n, η_i) for $\eta_e = 0.1$ and $\eta_e = 4.0$ respectively. As a reference the stability curve of the pure toroidal-ITG is added (dashed line). Note that in both cases the η_i threshold is only removed for low values of ϵ_n. This corresponds to the parameter region where the toroidal-ITG starts to propagate in the electron diamagnetic direction, therefore allowing a more effective coupling to the TEM.

Fig.2.13 shows for $\eta_e = 4.0$ the frequencies and growth rates of the two instabilities as a function of the precessional amplitude G. The TEM-type instability vanishes for $G < 0$. However for the toroidal-ITG-type instability, trapped electrons only have a damping effect for $G \lesssim -0.75$. As shown by Fig.C.1 of appendix C this requires an unrealistic

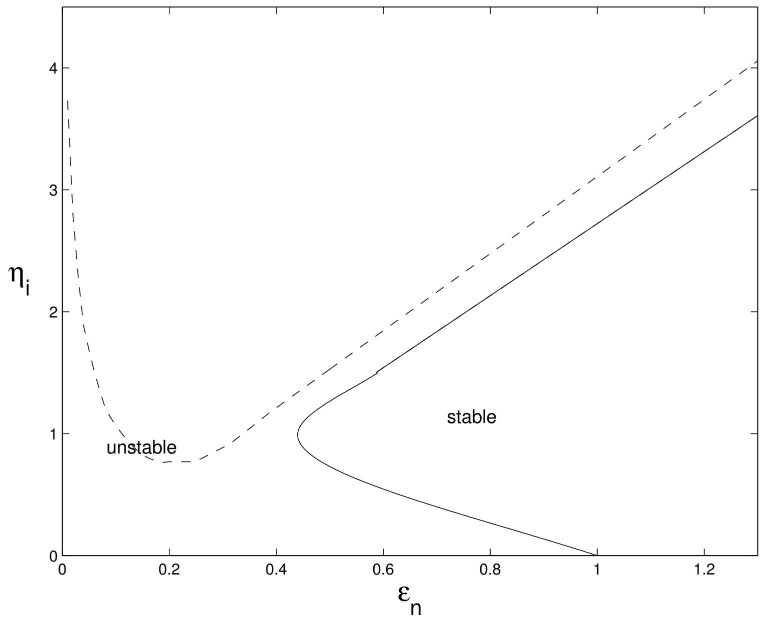

Figure 2.11: Effect of non-adiabatic trapped electrons on stability curve (full line) in plane (ϵ_n, η_i). The η_i threshold is removed for low values of ϵ_n. Here $\tau = 1.0$, $\alpha_b = 0.32$, $G = 1.0$, $\eta_e = 0.1$, $k_\parallel = 0$, $k_\perp \lambda_{L\,i} = 0.3$. For comparison, the stability curve without trapped electrons (dashed line) is also plotted.

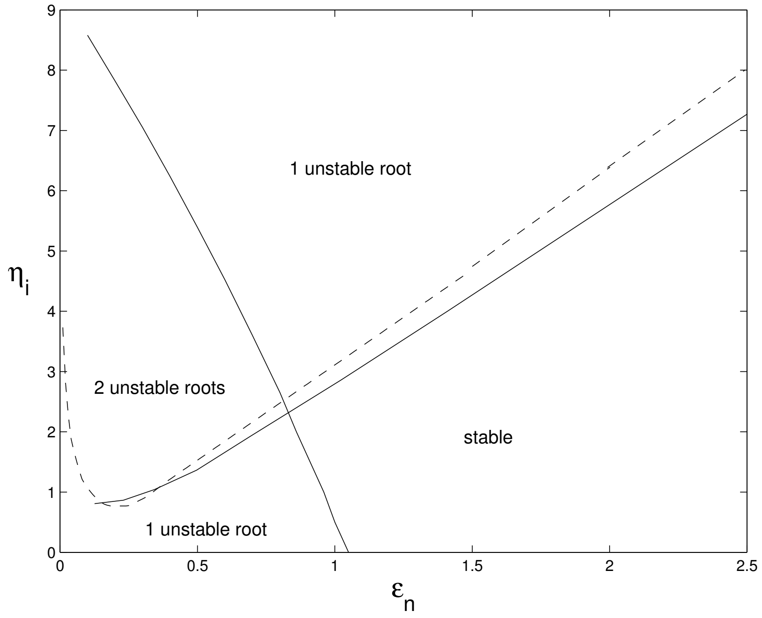

Figure 2.12: The same as in the previous figure except for $\eta_e = 4$.

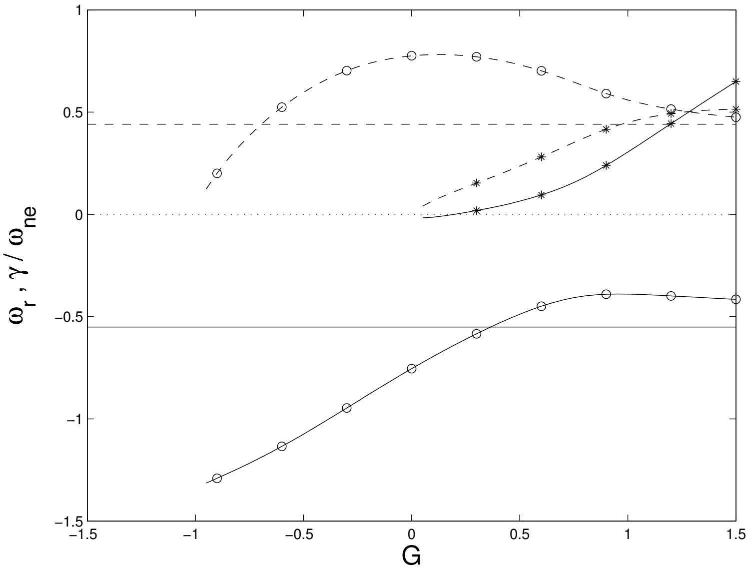

Figure 2.13: Dependence of real frequency (full line) and growth rate (dashed line) on magnitude G of precessional drift. Here $\tau = 1$, $\epsilon_n = 0.3$, $\eta_i = 2$, $\alpha_b = 0.32$, $\eta_e = 4$, $k_\| = 0$, $k_\perp \lambda_{L\,i} = 0.3$. The trapped electron instability (stars) disappears for $G < 0$, the toroidal-ITG type mode (circles) however has maximum growth rate around $G = 0$. For comparison, plain curves represent results without trapped electron dynamics.

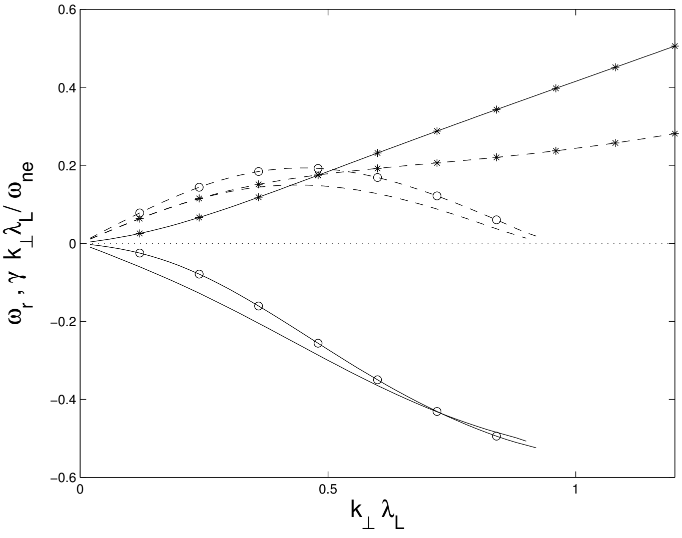

Figure 2.14: The same as in previous figure however varying $k_\perp \lambda_{L\,i}$ and holding $G = 1$ fixed. The growth rate of the toroidal-ITG (circles) peaks at $k_\perp \lambda_{L\,i} \sim 0.5$ due to FLR effect of ions, similar to the case without trapped electrons (plain). The TEM (stars) however is unaffected by ion dynamics and its growth rate does not role over for these values of $k_\perp \lambda_{L\,i}$.

negative shear.

Finally, again for $\eta_e = 4.0$, Fig.2.14 presents the variation of the frequencies and growth rates with increasing perpendicular wave number. As in the absence of trapped electrons, the toroidal-ITG starts to be stabilized beyond $k_\perp \lambda_{L\,i} \sim 0.5$ due to FLR effects of ions. The TEM, essentially insensible to ion dynamics, keeps on growing. Going to even shorter wavelengths would ultimately require taking into account finite banana width and finite Larmor width effects of electrons.

Chapter 3

Global Gyrokinetic Model in Cylinder

When keeping FLR and finite orbit width effects of ions to all orders the non-Hermitian eigenvalue problem for the electrostatic potential appears in the form of an integral equation. Before considering the two-dimensional problem of a toroidal system, we have started by developing methods for solving this eigenvalue equation in the case of a simple cylindrical configuration[39]. This geometry can be considered as the limiting case of a stretched tokamak to a periodic cylindrical plasma with remaining magnetic shear and realistic density and temperature profiles.

Kinetic equations have been solved in the past for spectral problems in cylindrical plasmas when studying mirror-like configurations confined by straight magnetic fields [17] [18]. Fourier representation appears naturally in gyrokinetic theory as it allows one to integrate explicitly the unknown perturbed fields along the trajectories of the particles. Gyroaveraging, as already shown in chapter 2, is such an operation. In Refs [17][18], the plane wave decomposition was considered as it enabled to perform these integrations analytically with no further approximation. However, in other then the simplest cases (slab, cylinder), the plane wave decomposition is unsuited to the geometry of the system. In a torus for instance, it is advantageous to choose a curved wave representation, compatible with the magnetic surfaces. By defining these mode components to be propagating waves, gyroaveraging can still be carried out analytically but nevertheless becomes more delicate as the wave vector is now local and varies between the particle and guiding center (GC) position, especially near a geometrical singularity such as the magnetic axis. This requires certain approximations which must be justified. For a test case this problem is addressed here using a special cylindrical wave decomposition which is different from the usual Bessel representation. Two methods for solving the final eigenvalue equation have been tested. The first computes the perturbation in configuration space using a finite element method with well known convergence properties and has been crucial for verifying and validating the second which consists of working directly in the Fourier space relative to the non-standard cylindrical mode decomposition. Therefore both techniques shall be presented here although the latter turns out to be the method of choice when going to a toroidal geometry, as it is the only one which allows a straightforward generalization to such a system. A numerical technique developed by Davies [40] turns out to be efficient for locating the eigenfrequencies of the non-Hermitian eigenvalue problem. As an illustration, results are shown for slab-like ITG instabilities.

3.1 Physical Model

A periodic cylindrical plasma of radius a and length $2\pi R$ is considered as the limiting case of a stretched torus. The plasma is confined by a magnetic field of the form

$$\vec{B}= B_0 \left(-\frac{\rho}{R q_s(\rho)}\, \vec{e_\theta} + \vec{e_z} \right),$$

where (ρ, θ, z) are the cylindrical coordinates, and $q_s = q_s(\rho)$ the safety factor profile such that $|B_\theta/B_z| \ll 1$. Magnetic surfaces are the cylinders $\rho =$const. Figure 3.1 illustrates these notations. It is assumed that the plasma contains one species of singly charged ions. For the derivations appearing in this chapter and the following we shall discard the indice 'i' for most physical quantities relative to ions, so as to lighten notations. The temperature T_i is an exception as it must be distinguished from the electron temperature

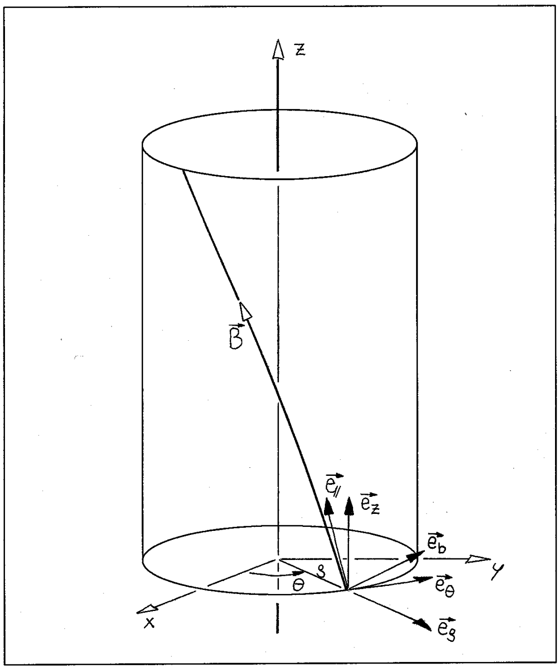

Figure 3.1: Geometry of a cylindrical plasma.

T_e, which is the only relevant physical parameter for adiabatic electrons.

3.1.1 The Gyrokinetic Equation in Cylindrical Geometry

The evolution of the fluctuating part $\tilde{f}$ of the ion distribution function is given by the linearized GKE (2.21) written in gyrokinetic variables $(\vec{R}, \mathcal{E}, \mu, \alpha, \sigma)$:

$$\left.\frac{D}{Dt}\right|_{u.t.g.} \tilde{g} = \left(\frac{\partial}{\partial t} + \vec{v}_g \cdot \frac{\partial}{\partial \vec{R}}\right) \tilde{g} = \left(\frac{e}{T_i} F_M \frac{\partial}{\partial t} + \frac{dF_M}{d\rho} \frac{1}{B} \vec{e}_\theta \cdot \nabla\right) < \phi >, \tag{3.1}$$

where $\tilde{g} = \tilde{f} + e\phi F_M / T_i$ is the non-adiabatic part of the distribution function $\tilde{f}$, and F_M the local Maxwellian distribution function

$$F_M(\rho, \mathcal{E}) = \frac{N}{(2\pi T_i/m_i)^{3/2}} \exp - \left(\frac{\mathcal{E}}{T_i/m_i}\right),$$

with temperature $T_i = T_i(\rho)$ and density $N = N(\rho)$ constant on a magnetic surface. The GC velocity

$$\vec{v}_g = v_\parallel \vec{e}_\parallel + \vec{v}_d,$$

is divided into parallel motion and drifts

$$\vec{v}_d = \frac{1}{\Omega}\left(\frac{v_\perp^2}{2} + v_\parallel^2\right) \vec{e}_\parallel \times \nabla \ln B.$$

It will be shown here that these drifts, related to the finite safety factor, only have a very weak effect and therefore are negligible in torus compared to the much stronger drifts related to the toroidal curvature.

To be able to perform explicitly the gyroaveraging of the unknown potential, a plane wave decomposition is usually considered:

$$\phi(\vec{r}) = \int d\vec{k}\; e^{i\vec{k}\cdot\vec{r}}\; \overset{\wedge}{\phi}(\vec{k}). \tag{3.2}$$

Gyroaveraging can then be performed analytically with no further approximation:

$$\begin{aligned} <\phi> &= \int d\vec{k}\; e^{i\vec{k}\cdot\vec{R}}\; \overset{\wedge}{\phi}(\vec{k}) \frac{1}{2\pi}\int_0^{2\pi} d\alpha\; \exp\left(-i\,\vec{k}\cdot\frac{\vec{v}\times\vec{e}_\parallel}{\Omega}\right) \\ &= \int d\vec{k}\; J_0\left(\frac{k_\perp v_\perp}{\Omega}\right) e^{i\vec{k}\cdot\vec{R}}\; \overset{\wedge}{\phi}(\vec{k}), \end{aligned}$$

using the integral representation of the Bessel function [60]. Thus Fourier space appears as the natural representation for gyrokinetic theory.

Going back to particle variables $(\vec{r}, \vec{v})$ and keeping lowest order terms in the small parameter ϵ (2.17) of gyro-ordering, one must essentially replace the factor $\exp i\,\vec{k}\cdot\vec{R}$ by $\exp i\,\vec{k}\cdot(\vec{r} + \vec{v}\times\vec{e}_\parallel/\Omega)$ so that

$$\begin{aligned} &\left(\frac{\partial}{\partial t} + \vec{v}_g \cdot \frac{\partial}{\partial \vec{r}}\right) \tilde{g}(\vec{r}, \vec{v}, t) = \\ &\quad \left(\frac{e}{T_i} F_M \frac{\partial}{\partial t} + \frac{dF_M}{d\rho}\frac{1}{B}\,\vec{e}_\theta \cdot \nabla\right) \int d\vec{k}\; J_0\left(\frac{k_\perp v_\perp}{\Omega}\right) e^{i\vec{k}\cdot\vec{r}} \exp\left(i\,\vec{k}\cdot\frac{\vec{v}\times\vec{e}_\parallel}{\Omega}\right) \overset{\wedge}{\phi}(\vec{k}, t). \end{aligned} \tag{3.3}$$

For a curved system, the plane wave decomposition (3.2), although exact [17][18], leads to relations that do not allow the simple numerical methods presented in Sec.3.2. Instead let us consider another Fourier representation which will be referred to as the cylindrical wave decomposition, so that in the above relations the following terms must be replaced by the corresponding right hand side:

$$\int d\vec{k}\; e^{i\vec{k}\cdot\vec{r}}\;\overset{\wedge}{\phi}(\vec{k}) \;\longrightarrow\; \sum_{m,n}\int d\kappa\;\overset{\wedge}{\phi}_{m,n}(\kappa)\exp i(\kappa\rho + m\theta + n\frac{z}{R}).$$

In particular one must reconsider

$$\begin{aligned}\vec{k}\cdot\vec{R} &= \vec{k}\cdot\vec{r} + \vec{k}\cdot\frac{\vec{v}\times\vec{e_\parallel}}{\Omega} \\ &\longrightarrow \left(\kappa\rho + m\theta + n\frac{z}{R}\right) + \left(\kappa\nabla\rho + m\nabla\theta + \frac{n}{R}\nabla z\right)\cdot\frac{\vec{v}\times\vec{e_\parallel}}{\Omega} + O(\epsilon^2).\end{aligned} \tag{3.4}$$

Note that the last relation is valid only to order $O(\epsilon)$. The effect of this approximation will be discussed further on. From Eq.(3.4) the local wave vector can be deduced:

$$\vec{k}\longrightarrow \kappa\nabla\rho + m\nabla\theta + \frac{n}{R}\nabla z = \kappa\,\vec{e_\rho} + \frac{m}{\rho}\,\vec{e_\theta} + \frac{n}{R}\,\vec{e_z}\;.$$

As the system is homogeneous along θ, z and time, the poloidal and toroidal wave numbers (m, n) can be fixed, as well as the frequency ω:

$$\phi(\vec{r},t) = \phi(\rho)\exp i(m\theta + n\frac{z}{R} - \omega t). \tag{3.5}$$

Thus, the linear study becomes an effectively one dimensional problem along the radial direction.

One can easily show that $\vec{e_\rho}\cdot\vec{v_d}= 0$ so that the GC trajectories lie on the magnetic surfaces $\rho =$const. This leads to a straightforward solution of the gyrokinetic equation:

$$\begin{aligned}\tilde{f}(\rho,\vec{v}) &= \frac{e}{T_i}\Bigg[-\phi(\rho)F_M \\ &+ \frac{(\omega-\omega^\star)F_M}{\omega - k_\parallel v_\parallel - \omega_g}\int d\kappa J_0(\frac{k_\perp v_\perp}{\Omega})e^{i\kappa\rho}\exp(i\,\vec{k}\cdot\frac{\vec{v}\times\vec{e_\parallel}}{\Omega})\,\overset{\wedge}{\phi}(\kappa)\Bigg],\end{aligned} \tag{3.6}$$

with $k_\parallel = (nq_s - m)/Rq_s$, $k_\theta = m/\rho$, $k_\perp = \sqrt{\kappa^2 + k_\theta^2}$, the different components of the wave vector, and

$$\begin{aligned}\omega_g &= k_\theta v_d = -\frac{1}{\Omega}\left(\frac{v_\perp^2}{2} + v_\parallel^2\right)\frac{k_\theta}{R_\theta}, \qquad \frac{1}{R_\theta} = \frac{1}{Rq_s}\frac{d}{d\rho}\left(\frac{\rho^2}{Rq_s}\right), \\ \omega^\star &= \omega_n\left(1 + \eta T_i\frac{\partial}{\partial T_i}\right), \qquad \omega_n = \frac{T_i}{eB}\frac{d\ln N}{d\rho}k_\theta,\end{aligned}$$

the guiding center and diamagnetic drift frequencies, $\eta = d\ln T_i/d\ln N$. In (3.6) $\Im m(\omega)$ is taken positive to ensure causality.

3.1.2 The Eigenvalue Equation

The system is closed invoking quasineutrality (2.24):

$$\varrho_q^{int} = e(n_i - n_e) \simeq 0, \tag{3.7}$$

n_i and n_e being respectively the ion and electron densities. This relation must hold as well for the stationary state as for the fluctuating parts. Hence, the perturbed ion density $\tilde{n}_i$ is evaluated:

$$\begin{aligned}&\tilde{n}_i(\rho) = \int \tilde{f}(\rho, \vec{v}) d\vec{v} = \\ &\quad \frac{Ne}{T_i}\left[-\phi(\rho) + (\omega - \omega^\star)\int d\kappa e^{i\kappa\rho} \overset{\wedge}{\phi}(\kappa) \frac{1}{(2\pi v_{th\,i}^2)^{3/2}} \int d\vec{v}\, \frac{J_0^2(k_\perp v_\perp/\Omega)\exp(-v^2/2v_{th\,i}^2)}{\omega - k_\parallel v_\parallel - \omega_g}\right],\end{aligned}$$

where $d\vec{v} = 2\pi v_\perp dv_\perp dv_\parallel$, the integral over α having again been performed analytically. Here the perturbed electron density may be reduced to the adiabatic response

$$\tilde{n}_e = \frac{e\phi}{T_e} N.$$

Inverting the Fourier representation by expressing $\overset{\wedge}{\phi}(\kappa)$ in terms of $\phi(\rho)$, the quasineutrality equation now becomes

$$-\overset{\sim}{\varrho}_q^{int}(\rho) = \int d\rho' \mathcal{K}(\rho, \rho'; \omega)\phi(\rho') = 0, \tag{3.8}$$

with

$$\begin{aligned}\mathcal{K}(\rho, \rho'; \omega) &= \frac{Ne^2}{T_i}\left[\left(\frac{1}{\tau} + 1\right)\delta(\rho - \rho') - \mathcal{N}(\rho, \rho'; \omega)\right], &(3.9)\\ \mathcal{N}(\rho, \rho'; \omega) &= \frac{1}{2\pi}\int d\kappa \exp(i\kappa|\rho - \rho'|) \overset{\wedge}{\mathcal{N}}(\rho, \kappa; \omega), &(3.10)\\ \overset{\wedge}{\mathcal{N}}(\rho, \kappa; \omega) &= (\omega - \omega^\star)\frac{1}{(2\pi v_{th\,i}^2)^{3/2}}\int d\vec{v}\, \frac{J_0^2(k_\perp v_\perp/\Omega)\exp(-v^2/2v_{th\,i}^2)}{\omega - k_\parallel v_\parallel - \omega_g}, &(3.11)\end{aligned}$$

all equilibrium quantities being evaluated at ρ and having defined $\tau = T_e/T_i$. Eq(3.8) is an eigenvalue equation, i.e. one must find the complex frequencies ω for which there exists a non trivial function ϕ verifying this relation.

In a first approximation, GC drifts are neglected in the resonant denominator so that the velocity integrals can be separated and expressed in terms of the scaled modified Bessel function $\Lambda_p(x) = e^{-x} I_p(x)$ and the plasma dispersion function $W(z)$ [52]:

$$\frac{1}{(2\pi v_{th\,i}^2)^{3/2}} \int d\vec{v}\, \frac{J_0^2(k_\perp v_\perp/\Omega)\exp(-v^2/2v_{th\,i}^2)}{\omega - k_\parallel v_\parallel} = -\Lambda_0(\xi)\frac{1}{\omega}\left[W(z) - 1\right], \tag{3.12}$$

with the definitions $\xi = (k_\perp \lambda_L)^2$, $\lambda_L = v_{th\,i}/\Omega$, $z = \omega/|k_\parallel| v_{th\,i}$ and

$$W(z) = \frac{1}{\sqrt{2\pi}} \int_{-\infty}^{+\infty} \frac{x}{x - z} \exp(-\frac{x^2}{2}) dx \quad , \quad \Im m(z) > 0.$$

When carrying out the derivative with respect to T_i one obtains

$$\begin{aligned} \overset{\wedge}{\mathcal{N}}(\rho, \kappa; \omega) &= \left(\frac{\omega^\star}{\omega} - 1\right)(W - 1)\Lambda_0 \qquad (3.13) \\ &= \left[\frac{\omega_n}{\omega}\left(1 - \frac{\eta}{2}\right) - 1\right](W - 1)\Lambda_0 + \frac{\omega_n}{\omega}\eta\left[\frac{z^2}{2} W\Lambda_0 + (W - 1)\xi(\Lambda_1 - \Lambda_0)\right], \end{aligned}$$

using the notations $W = W(z)$, $\Lambda_p = \Lambda_p(\xi)$. The integral representation for the modified Bessel function[60]:

$$I_p(x) = \frac{1}{\pi} \int_0^\pi e^{x \cos\nu} \cos(p\nu) d\nu,$$

allows one to replace the integral over the infinite domain of κ appearing in $\mathcal{N}$ by the integral over the finite interval of the new variable ν [61]:

$$\begin{aligned} \mathcal{N}(\rho, \rho'; \omega) = \left(\frac{\omega^\star}{\omega} - 1\right)(W - 1)\frac{1}{2\pi\lambda_L} \int_0^\pi \frac{d\nu}{\sqrt{\pi(1 - \cos\nu)}} \times \\ \exp - \left[\left(\frac{m\lambda_L}{\rho}\right)^2 (1 - \cos\nu) + \left(\frac{\rho - \rho'}{2\lambda_L}\right)^2 \frac{1}{1 - cos\nu}\right], \end{aligned} \tag{3.14}$$

This last step will be useful when performing numerical integration.

For comparison purposes let us still summarize here the derivation leading to the eigenvalue equation in the case of plane wave decomposition. The decomposition in plane waves in the poloidal plane for a perturbation of the form (3.5) is given by

$$\begin{aligned} \overset{\wedge}{\phi}(\vec{k}_\perp) &= \frac{1}{(2\pi)^2} \int d\vec{r}\, \phi(\vec{r}) e^{-i\vec{k}_\perp \cdot \vec{r}} \\ &= \frac{1}{(2\pi)^2} \int_0^{+\infty} \rho d\rho \phi(\rho) \int_0^{2\pi} d\theta \exp i(m\theta - k_\perp \rho \cos(\theta - \theta_{\vec{k}})) \\ &= (-i)^m \frac{\exp im\theta_{\vec{k}}}{2\pi} \int_0^{+\infty} \rho d\rho \phi(\rho) J_m(k_\perp \rho), \end{aligned} \tag{3.15}$$

where $(k_\perp, \theta_{\vec{k}})$ are the polar coordinates of the poloidal component $\vec{k}_\perp$ of the plane wave vector $\vec{k}$. Inserting this relation in Eq.(3.3) and carrying out the equivalent steps as for the cylindrical wave decomposition leads to the following eigenvalue equation:

$$\begin{aligned}
-\varrho_q^{int}(\rho) &= \int \rho' d\rho' \mathcal{K}(\rho,\rho';\omega)\phi(\rho') = 0, && (3.16)\\
\mathcal{K}(\rho,\rho';\omega) &= \frac{Ne^2}{T_i}\left[\frac{1}{\rho}\left(\frac{1}{\tau}+1\right)\delta(\rho-\rho') - \mathcal{N}(\rho,\rho';\omega)\right], && (3.17)\\
\mathcal{N}(\rho,\rho';\omega) &= \left(\frac{\omega^\star}{\omega}-1\right)(W-1)\int_0^{+\infty} k_\perp dk_\perp J_m(k_\perp\rho)J_m(k_\perp\rho')\Lambda_0(\xi) && (3.18)\\
&= \left(\frac{\omega^\star}{\omega}-1\right)(W-1)\frac{1}{2\pi\lambda_L^2}\int_0^{\pi}\frac{d\nu}{(1-\cos\nu)}\times\\
&\quad \Lambda_m\left(\frac{\rho\rho'}{2\lambda_L^2(1-\cos\nu)}\right)\exp-\left[\left(\frac{\rho-\rho'}{2\lambda_L}\right)^2\frac{1}{1-\cos\nu}\right]. && (3.19)
\end{aligned}$$

Eq.(3.18) shows that in cylindrical geometry the plane wave decomposition actually leads to a Bessel representation instead of the handier Fourier transform appearing in (3.10). This illustrates how in a more complex geometry the plane wave decomposition simply becomes intractable.

3.1.3 Properties of the Integral Equation

Local Dispersion Relation

The eigenvalue problem is formulated as a one-dimensional integral equation for the radial dependence of the electrostatic potential. Notice that the only radial coupling comes from FLR effects appearing in (3.13) through the argument ξ and explicitly brought forth in relation (3.14). By taking $\xi = (\kappa^2 + k_\theta^2)\lambda_{L\,i}^2 \simeq (k_\theta\lambda_L)^2$ one neglects this coupling and finds a local dispersion relation for each magnetic surface:

$$D(\rho;\omega) = \frac{1}{\tau} + 1 - \overset{\wedge}{\mathcal{N}}(\rho, \kappa = 0; \omega) = 0. \qquad (3.20)$$

One must point out that (3.20) is equivalent to the local dispersion relation (2.27) of slab geometry so that after neglecting drifts, all modes that appear in cylinder are of slab type. Solving this equation for fixed wave numbers (m, n) gives the frequency as a function of ρ at which the decoupled magnetic surfaces oscillate. This local analysis gives a good initial estimation for the frequencies and radial localization of the global eigenmodes.

Energy Conservation, Power Response and Symmetry of the Integral Operator

For an electrostatic perturbation, the time variation of the total kinetic energy $E_k = \frac{1}{2}m\int d\vec{r}\ d\vec{v}\ v^2 f$ of the particles is given by

$$\frac{d}{dt}E_k = -\int d\vec{r}\ \phi\frac{\partial\varrho_q^{int}}{\partial t}. \tag{3.21}$$

The time averaged power absorbed or released by the particles with a wave of frequency ω thus reads

$$P =< \frac{d}{dt}E_k >= -\frac{1}{2}\Im m(\omega\int d\vec{r}\ \phi^\star\varrho_q^{int}). \tag{3.22}$$

Let us consider relation (3.22) with ϱ_q^{int} written in its integral form (3.8):

$$P = \frac{1}{2}\Im m\left[\omega\int d\rho\,\rho\phi^\star(\rho)\int d\rho'\mathcal{K}(\rho,\rho';\omega)\phi(\rho')\right].$$

In the absence of dissipation (i.e. $P = 0$) related to the imaginary parts produced by the resonant denominator $\omega - k_\parallel v_\parallel - \omega_g$, one concludes that the kernel $\mathcal{K}$ must verify

$$\rho\mathcal{K}(\rho,\rho';\omega) = \rho'\mathcal{K}(\rho',\rho;\omega). \tag{3.23}$$

This functional form holds even in the presence of dissipation when $\mathcal{K}$ becomes complex. In this sense the integral equation (3.8) is symmetric and not Hermitian. This does not appear explicitly in Eqs.(3.8) -(3.11). However, one must not forget that $\mathcal{K}$ was established only to lowest order in ϵ. Let us write all equilibrium terms depending on the variable ρ as in the following case for temperature:

$$T(\rho) = T\left(\frac{\rho+\rho'}{2}\right) + \frac{\rho-\rho'}{2}\frac{dT}{d\rho} + \ldots = T\left(\frac{\rho+\rho'}{2}\right) + O(\epsilon),$$

where we have used the fact that the radial coupling distance is of the order of the Larmor radius ($|\rho - \rho'| \sim \lambda_L$). In this way and to order to which we work, one can verify (3.23).

Boundary Conditions

As the equation is of integral type, it already contains boundary conditions. Expressions (3.8), (3.9) and (3.14) evidently show that the regularity condition at $\rho = 0$

$$\phi_m(\rho = 0) = 0 \quad \text{if} \quad m \neq 0, \tag{3.24}$$

is verified. However, we will see in the next point that the full regularity condition expected:

$$\phi_m(\rho) \sim \rho^{|m|} \quad \text{as} \quad \rho \longrightarrow 0, \tag{3.25}$$

is not exactly fulfilled. At the edge of the plasma, where the electron temperature falls to zero, one has the condition at the boundary

$$\phi_m(\rho = a) = 0, \tag{3.26}$$

for all values of m.

Fluid Limit

To get a better understanding of the behavior of Eq.(3.8) on the axis, the limiting case of cold ions is considered, so that the integral equation becomes differential:

$$\left\{\omega^2 \left[1 - \lambda_L^{\star 2} \left(\frac{d^2}{d\rho^2} - \frac{m^2}{\rho^2}\right)\right] - \omega\omega_{ne} - (k_\| c_s)^2 \right\} \phi = 0, \tag{3.27}$$

with $c_s^2 = T_e/m_i$, $\lambda_L^\star = c_s/\Omega$ and $\omega_{ne} = -\tau\omega_n$. This is the equation for the electron drift wave already discussed in its local form (2.28). Note that the only radial coupling, i.e. the differential character of the equation, comes from the polarization drift.

The question is whether Eq.(3.27) still contains approximations related to gyro-ordering. Had one intended to derive this relation from the basic set of fluid equations, that is the linearized equation of motion for cold magnetized ions:

$$m_i \frac{\partial \vec{v}}{\partial t} = e\left(\vec{v} \times \vec{B} - \nabla\phi\right),$$

the equation of continuity, the Boltzmann equation for electrons and invoking again quasineutrality, would have led to[62]:

$$\left\{\omega^2\left[1-\lambda_L^{\star 2}\left(\frac{1}{\rho}\frac{d}{d\rho}\rho\frac{d}{d\rho}-\frac{m^2}{\rho^2}\right)\right]-\omega\omega_{ne}-(k_\parallel c_s)^2\right\}\phi=0. \tag{3.28}$$

Note the difference with Eq.(3.27). This can be traced back to the approximation in relation (3.4) where the factor $1/|\nabla\theta| = \rho$, corresponding to the Jacobian in cylindrical variables, was treated as a characteristic length of equilibrium. As a consequence, this approximation leads to the following behavior on the axis:

$$\phi_m(\rho)\sim\rho^{m'} \quad , \quad m' = \frac{1+\sqrt{1+4m^2}}{2}, \tag{3.29}$$

instead of (3.25). However, for large values of $|m|$ this difference becomes negligible.

By considering Eqs(3.16)- (3.19) obtained with the plane wave decomposition, which are exact in this respect, and applying the asymptotic relation for the modified Bessel function

$$\Lambda_m(x)\longrightarrow\frac{1}{\sqrt{2\pi x}}\exp-\frac{m^2}{2x} \quad \text{as} \quad x\longrightarrow\infty,$$

which also improves for low arguments with increasing mode number m, one recovers Eqs (3.8), (3.9) and (3.14). Therefore, a few Larmor radii off the axis or for not too small poloidal mode numbers, the discussed difference is negligible. This is the case in practice where the linear instabilities are localized around the region of steepest gradients, i.e. usually around mid-point between the magnetic axis and plasma edge. Furthermore, for ITG instabilities $k_\parallel \simeq 0$, so that $m \simeq nq_s \neq 0$ if the toroidal mode number n is non zero.

3.2 Numerical Methods

The eigenvalue equation must be approximated by a finite set of simultaneous algebraic linear equations. In a first approach one solves the equation for the potential $\phi = \phi(\rho)$ in configuration space, as given by Eq.(3.8). In a second approach the equation for the potential written in Fourier representation $\overset{\wedge}{\phi}=\overset{\wedge}{\phi}(\kappa)$ is solved. It is not evident a priori wether the radial decomposition over the interval $0 < \rho < a$ of the perturbation and the non-periodic equilibrium quantities in terms of the components $\exp i\kappa\rho$ is practical. Thus, although the first technique cannot be directly generalized to a toroidal system due to the significantly more complicated particle trajectories in such a geometry, it has been essential here for testing and gaining confidence in the non-standard Fourier method.

3.2.1 Solving in Configuration Space

Equation (3.8) is classified as a linear homogeneous Fredholm equation of the second kind. As can be seen in relation (3.14), its kernel $\mathcal{N}(\rho, \rho'; \omega)$ exhibits a singularity at $\rho = \rho'$ with a characteristic length of the order of the ion Larmor radius. This is obviously related to the radial coupling due to FLR effects. Integrating this singularity numerically over ρ' would require a sufficient number of integration points in an interval of order λ_L. However, by using a finite element method, this can actually be performed analytically. Let us approximate $\phi(\rho)$ using a set of linearly independent basis functions $\{\Gamma_i(\rho)\}_{i=1,\dots,n_\rho}$:

$$\phi(\rho) = \sum_{i=1}^{n_\rho} \phi_i \Gamma_i(\rho). \tag{3.30}$$

For the purpose of solving the integral equation, it is sufficient to take constant elements:

$$\Gamma_i(\rho) = \begin{cases} 1 & \text{if} \quad \rho_{i-1} \le \rho \le \rho_i \\ 0 & \text{else,} \end{cases}$$

having defined a radial mesh $\{\rho_i\}_{i=0,\dots,n_\rho}$, not necessarily equidistant. Furthermore, let us point out here that the radial computing domain $\left[\rho_0 = \rho_l, \rho_{n_\rho} = \rho_u\right]$ need not be the whole interval $[0, a]$ but can be restricted to the sub-domain where the instability is localized.

Substituting relation (3.30) in Eq.(3.8) and projecting on the same basis $\{\Gamma_i\}$ leads to a system of linear equations for the components $\{\phi_i\}$:

$$\begin{aligned} \sum_{j=1}^{n_\rho} M_{ij}(\omega)\phi_j &= 0 \qquad , i = 1, \ldots, n_\rho, & (3.31)\\ M_{ij}(\omega) &= \int d\rho\, \rho \Gamma_i(\rho) \int d\rho' \mathcal{K}(\rho, \rho'; \omega)\Gamma_j(\rho'). & (3.32) \end{aligned}$$

The symmetry property of the kernel given by relation (3.23) translates to the complex matrix M:

$$M_{ij} = M_{ji} \quad , \quad i, j = 1, \ldots, n_\rho. \tag{3.33}$$

The elements $\{\Gamma_i\}$ must be able to resolve the radial wavelength, which implies under the gyro-ordering assumption (2.20) that

$$\Delta\rho_i = |\rho_i - \rho_{i-1}| \sim \lambda_L,$$

and thus by (2.17) that the equilibrium quantities can be considered constant over the corresponding interval. Using this approximation when evaluating the matrix element M_{ij} and commuting the integral over ν in relation (3.14) with those over ρ and ρ':

$$\begin{gathered} M_{ij}(\omega) = \frac{Ne^2}{T_{ion}}\, \bar{\rho_i} \left\{ \left(\frac{1}{\tau} + 1\right) \Delta\rho_i\, \delta_{ij} - \left(\frac{\omega^\star}{\omega} - 1\right) (W-1) \frac{1}{2\pi\lambda_L} \int_0^\pi \frac{d\nu}{\sqrt{\pi(1-\cos\nu)}} \times \right. \\ \left. \exp\left[-(m\lambda_L/\bar{\rho_i})^2(1-\cos\nu)\right] \int_{\rho_{i-1}}^{\rho_i} d\rho \int_{\rho_{j-1}}^{\rho_j} d\rho' \exp\left[-(\frac{\rho-\rho'}{2\lambda_L})^2 \frac{1}{1-\cos\nu}\right] \right\}, \end{gathered}$$

where all equilibrium quantities are evaluated at $\rho = \bar{\rho_i} = (\rho_i + \rho_{i-1})/2$. The integration over ρ and ρ' has now been brought down to the term giving rise to the actual radial coupling and to the above mentioned singularity:

$$\begin{aligned} I_{ij} &= \frac{1}{\lambda_L^2(1-\cos\nu)} \int_{\rho_{i-1}}^{\rho_i} d\rho \int_{\rho_{j-1}}^{\rho_j} d\rho' \exp\left[-\left(\frac{\rho-\rho'}{2\lambda_L}\right)^2 \frac{1}{1-\cos\nu}\right] \\ &= -2\left[\sqrt{\pi} x_{ij}\, \mathrm{erf}(x_{ij}) + e^{-x_{ij}^2}\right]\Big|_{i-1}^{i}\Big|_{j-1}^{j}, \end{aligned}$$

where $x_{ij} = (\rho_i - \rho_j)/(2\lambda_L\sqrt{1-\cos\nu})$ and $\mathrm{erf}(z) = (2/\sqrt{\pi}) \int_0^z e^{-t^2} dt$ is the error function.

Finally, performing the derivative with respect to temperature contained in $\omega^\star$ gives

$$\begin{aligned}
M_{ij} &= \frac{Ne^2}{T_{ion}}\,\bar{\rho}_i\left[\left(\frac{1}{\tau}+1\right)\Delta\rho_i\,\delta_{ij}\right. \\
&\quad \left.-\left\{\left[\frac{\omega_n}{\omega}\left(1-\frac{\eta}{2}\right)-1\right](W-1)+\frac{\omega_n}{\omega}\eta\frac{z^2}{2}W\right\}C_{ij}-\frac{\omega_n}{\omega}\eta(W-1)C'_{ij}\right], \qquad (3.34) \\
C_{ij} &= \frac{\lambda_L}{2\pi}\int_0^\pi d\nu\sqrt{\frac{1-\cos\nu}{\pi}}\exp\left[-(m\lambda_L/\,\bar{\rho}_i)^2(1-\cos\nu)\right]I_{ij}, \qquad (3.35) \\
C'_{ij} &= T_{ion}\frac{\partial}{\partial T_{ion}}C_{ij} = -\frac{\lambda_L}{2\pi}\int_0^\pi d\nu\sqrt{\frac{1-\cos\nu}{\pi}}\times \qquad (3.36) \\
&\quad \exp\left[-\left(\frac{m\lambda_L}{\bar{\rho}_i}\right)^2(1-\cos\nu)\right]\left[\left(\frac{m\lambda_L}{\bar{\rho}_i}\right)^2(1-\cos\nu)I_{ij}+\,e^{-x_{ij}^2}\Big|_{i-1}^{i}\Big|_{j-1}^{j}\right].
\end{aligned}$$

The integrals over ν in the definitions of the coupling matrices C_{ij} and C'_{ij} are computed using an extended trapezoidal rule. These matrices are sparse band as two elements Γ_i and Γ_j are coupled only if they are contained in the same interval of a few Larmor radii. The significant off-diagonal terms are therefore such that

$$C_{ij}, C'_{ij} \neq 0 \quad\Longleftrightarrow\quad \left|\bar{\rho}_i-\bar{\rho}_j\right| \overset{\sim}{<} l\lambda_L,$$

where typically $l \simeq 8$. In addition, note that these matrices are independent of ω and can therefore be precalculated.

The analytic continuation of the dispersion function to the whole complex plane can be expressed as

$$W(z) = 1 + i\sqrt{\frac{\pi}{2}}z\,e^{-z^2}\left[1+\mathrm{erf}(iz)\right],$$

where the complex error function can be computed efficiently using an algorithm by W.Gautschi [63].

3.2.2 Solving in Fourier Space

By performing a Fourier transform of Eq.(3.8), one obtains an equivalent equation for $\overset{\wedge}{\phi}(\kappa)$. Because the radial domain is finite, one can actually perform a Fourier series instead of a Fourier transform. This alternative is of interest as the equation then becomes naturally discrete with no singularity to be integrated:

$$\begin{aligned}\sum_{k'=-\infty}^{+\infty} \hat{M}_{kk'}(\omega)\,\hat{\phi}_{k'} &= \sum_{k'=-\infty}^{+\infty} \hat{\mathcal{K}}_{k-k',k'}(\omega)\,\hat{\phi}_{k'} = 0, && (3.37)\\ \phi(\rho) &= \sum_{k=-\infty}^{+\infty} \hat{\phi}_k \exp ik\frac{2\pi}{\Delta\rho}\rho, && (3.38)\end{aligned}$$

$$\hat{\mathcal{K}}_{k'',k'}(\omega) = \frac{1}{\Delta\rho}\int_{\rho_l}^{\rho_u} d\rho \frac{Ne^2}{T_i}\left[\frac{1}{\tau} + 1 - \hat{\mathcal{N}}\left(\rho, \kappa' = k'\frac{2\pi}{\Delta\rho};\omega\right)\right] \exp -ik''\frac{2\pi}{\Delta\rho}\rho,$$

where $\Delta\rho = \rho_u - \rho_l$ is the width of the considered radial interval. To compute the elements $\hat{\mathcal{K}}_{k''k'}(\omega)$, an equidistant mesh $\{\rho_i\}_{i=0,\ldots,n_\rho}$ was taken so that fast Fourier transform algorithms could be applied. This gives rise to n_ρ non-zero elements $\hat{\mathcal{K}}_{k''k'}$, $-n_\rho/2 \lesssim k'' \lesssim n_\rho/2$, i.e. $\hat{M}$ is a band matrix with $\sim n_\rho/2$ sub- and super-diagonals. As opposed to the required mesh density when solving in configuration space, note that here the radial mesh need only resolve equilibrium quantities. Therefore, the number of off-diagonals in $\hat{M}$ increases with the inhomogeneity of equilibrium. However, the sums over k and k' in Eq.(3.37) and (3.38) related to the Fourier series of the perturbing electrostatic potential are truncated at $\pm k_{max}$ such that

$$k_{max}\frac{2\pi}{\Delta\rho}\lambda_L \sim 1, \tag{3.39}$$

in agreement with gyro-ordering.

When solving over the whole radial interval $[0, a]$, note that the boundary conditions (3.24) and (3.26) are still contained in Eq.(3.37) but in Fourier representation now read

$$\begin{aligned}&\lim_{\rho\to 0}\sum_k \hat{\phi}_k \exp ik\frac{2\pi}{a}\rho = 0, \qquad \text{if} \qquad m \neq 0,\\ &\lim_{\rho\to a}\sum_k \hat{\phi}_k \exp ik\frac{2\pi}{a}\rho = 0.\end{aligned}$$

Unlike the approach in configuration space (in particular to obtain Rel.(3.14)), no assumption has yet been made concerning drifts. Although this requires two additional velocity integrals, and for typical physical values leads only to minor corrections of ITG-instabilities, drifts can be considered here with no further difficulty. Keeping these terms and defining the dimensionless velocity variable $\vec{\mathsf{v}} = \vec{v}\,/v_{th\,i}$, Eq.(3.37) has to be solved with $\overset{\wedge}{\mathcal{N}}$ given by

$$\begin{aligned}\overset{\wedge}{\mathcal{N}}(\rho,\kappa;\omega) &= \int_0^{+\infty} d\mathsf{v}_\perp \mathsf{v}_\perp J_0^2\left(\sqrt{\kappa^2+k_\theta^2}\,\lambda_L \mathsf{v}_\perp\right) e^{-\mathsf{v}_\perp^2} \times \\ &\frac{1}{\sqrt{2\pi}}\int_{-\infty}^{+\infty} d\mathsf{v}_\parallel \frac{z - \frac{\omega_n}{|k_\parallel| v_{th\,i}}\left[1+\frac{\eta}{2}\left(\mathsf{v}_\parallel^2+\mathsf{v}_\perp^2-3\right)\right]}{z - \mathsf{v}_\parallel - \omega_g(\mathsf{v}_\parallel,\mathsf{v}_\perp)/|k_\parallel| v_{th\,i}} e^{-\mathsf{v}_\parallel^2}.\end{aligned} \tag{3.40}$$

The Gaussian velocity distribution allows one to approximate the integration boundaries at ±∞ by finite values $\pm\mathsf{v}_{max\parallel,\perp} \sim 5$. Extended trapezoidal rules are applied for these numerical quadratures. One must still point out that unless performing an integration along a contour in the complex $\mathsf{v}_\parallel$ plane, so as to avoid, in agreement with causality, the poles related to the resonant denominator, relation (3.40) is only valid for frequencies such that $\Im m(\omega) > 0$. This is assumed here, as it greatly simplifies the velocity integration, however it restricts the study to unstable modes.

Some details on the computer implementation itself appear in the next chapter where the more general toroidal system is considered.

3.2.3 Searching for the Eigenfrequencies

Once the eigenvalue equation has been cast in one of the matrix forms (3.31) or (3.37), the problem of finding the eigenfrequencies can be written:

$$D(\omega) = det\, M(\omega) = 0. \tag{3.41}$$

This equation was first solved by sampling the determinant over a Cartesian mesh grid in the complex frequency plane and obtaining approximate intersection points of the contours

$$\begin{cases} \Re e D(\omega) &= 0, \\ \Im m D(\omega) &= 0. \end{cases}$$

These results were then refined using Newton's root finding method. This approach is time consuming as it requires a two-dimensional scan.

Solving (3.41) was greatly optimized by applying a practical method proposed by Davies [40], which takes advantage of the fact that $D(\omega)$ is analytic. Suppose $h(z)$ is an analytic function inside a closed positively oriented contour C. Having determined the number N of enclosed zeros $\{a_i\}_{i=1,\ldots,N}$ using the principle of argument, the method is then based on the evaluation of an equivalent number of integrals:

$$S_n = \frac{1}{2\pi i}\int_C z^n \frac{h'(z)}{h(z)} dz \qquad n = 1, \ldots, N, \tag{3.42}$$

which have the property

$$S_n = \sum_{i=1}^{N} a_i^n \qquad n = 1, \ldots, N. \tag{3.43}$$

The set of equations (3.43) is then solved finding the roots of the associated polynomial defined by

$$P_N(z) = \prod_{i=1}^{N}(z - a_i) = \sum_{i=0}^{N} A_i z^{N-i}. \tag{3.44}$$

A recursive relation enables to calculate the coefficients A_n from S_n:

$$\begin{aligned} S_1 &+ A_1 = 0 \\ S_2 &+ A_1 S_1 + 2A_2 = 0 \\ S_k &+ A_1 S_{k-1} + A_2 S_{k-2} + \ldots + kA_k = 0 \quad k = 1, \ldots, N. \end{aligned}$$

The numerical technique by Davies is developed for circular contours. We have generalized this algorithm to allow for more elongated curves in the frequency plane. This is achieved by applying the above method along a unit circle to the function $D(z) = D(\omega(z))$ with $\omega(z)$ being a conformal transformation of the unit disc at origin. We chose

$$\omega(z) = \tilde{\omega} + r\, z(Ez^2 + 1), \tag{3.45}$$

transforming the unit circle in the z-plane to a more oval-shaped curve in the ω-plane centered at $\tilde{\omega}$ with average radius r. The elongation and orientation are defined by the complex parameter E ($|E| \lesssim 0.1$).

The advantage of this method lies in the fact that the determinant must only be evaluated along a contour. Furthermore, up to ten roots inside a single curve with usually more than four significant digits can directly be obtained, so that no further refinement is necessary. To achieve this accuracy the number of sampling points, equidistant along the unit circle, is increased until the maximum jump in the argument of $D(\omega(z))$ is less then $\pi/2$.

Having identified an eigenfrequency ω_i, the corresponding eigenmode is computed by considering an inhomogeneous right hand side in (3.31) or (3.37) with $\omega = \omega_i$ then solving for ϕ. The initial right hand side is chosen as a first guess of the eigenvector structure. This process is then repeated iteratively until convergence is attained. This approach is inspired by the inverse iterative method for solving standard eigenvalue problems.

Let us still point out that when considering FLR effects to all orders, i.e. solving the integral equation, the spectrum contains no spurious modes.

3.3 Results

As an illustration, a hydrogen plasma with the following parameters is considered: major radius $R = 1$ m, minor radius $a = 0.2$m, magnetic field on axis $B_0 = 2$ Tesla, safety factor profile $q_s(s) = 1 + 2s^2$, density profile $N(s)/N_0 = 1 - s^2$, electron temperature profile $T_e(s)/T_{e0} = (1 - s^2)^2$, ion temperature profile $T_i(s)/T_{i0} = (1 - s^2)^3$, temperatures on axis $T_{e0} = T_{i0} = 2$ keV. Here $s = \rho/a$ stands for the normalized radial variable. The average ion Larmor radius is $\lambda_{Li} \simeq 1.5 \cdot 10^{-3}$m so that $\epsilon = \lambda_{Li}/a \simeq 7.5 \cdot 10^{-3}$. In the frame of our model, the plasma can exhibit slab-like ITG instabilities. As seen in section 2.6, for fixed mode numbers (m, n) the plasma is locally unstable if $\eta_i > \eta_{ic} \simeq 1$ around the corresponding mode rational surface. Thus the plasma considered here is unstable at any mode rational surface as $\eta_i(s) \equiv 3$.

Fig.3.2 shows the unstable spectrum in the complex frequency plane for mode numbers $(m = 8, n = 5)$. All frequencies are normalized with respect to $\omega_{norm} = T_{i0}/(eB_0a^2) =$

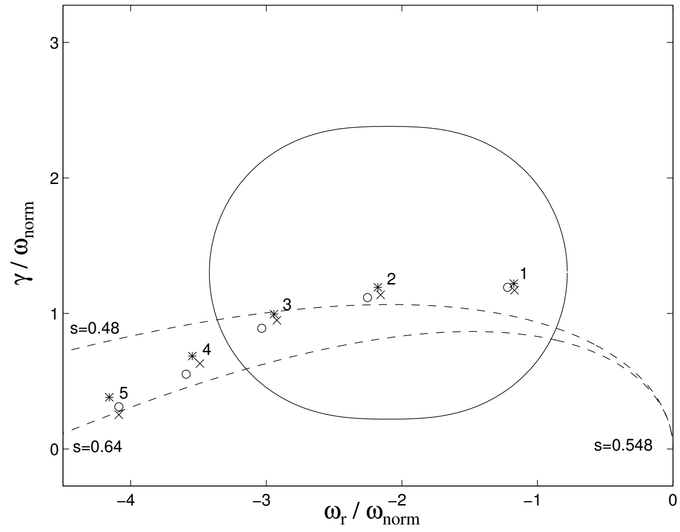

Figure 3.2: Spectrum in complex frequency plane of highest growing global modes ($m = 8, n = 5$). Circles are results obtained solving in configuration space, stars and crosses were computed in Fourier space with and without considering GC drifts respectively. A typical path for sampling the determinant of the system is drawn in full line. The solution to the local dispersion relation, parameterized by the radial variable s, is plotted with a dashed line.

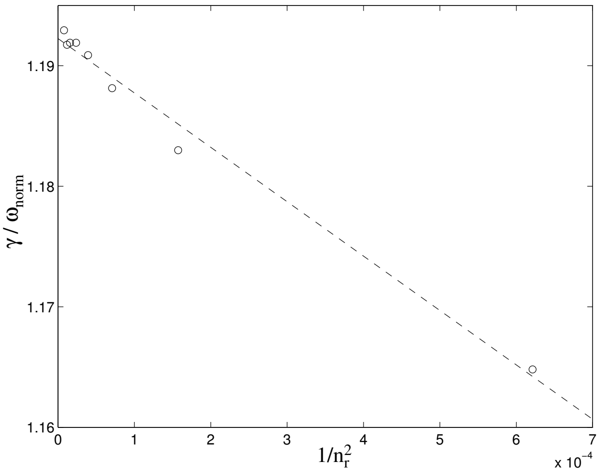

Figure 3.3: Convergence of growth rate for the most unstable mode ($m = 8, n = 5$) versus $1/n_\rho^2$ obtained by the method in configuration space.

$2.5\,10^4 s^{-1}$. Results obtained with the numerical method in configuration space are represented with circles, results computed with the Fourier approach without considering GC drifts are plotted with crosses. The slight differences result essentially from the fact that in the first technique the symmetry (3.23) has been enforced as it translates easily to the corresponding matrix as shown by relation (3.33). This has not been carried out for the second technique where this property appears less explicitly. The spectrum found by the Fourier method when taking into account GC drifts is reproduced with stars. Neglecting the GC drifts is indeed a good approximation, however their effect is always destabilizing as the magnetic curvature in a cylindrical geometry is everywhere unfavorable. The solution to the local dispersion relation (3.20), parameterized with respect to the radial variable s, is drawn with a dashed line. An oval-shaped path defined by the conformal transformation (3.45) of the unit disc with $\tilde{\omega}\ /\omega_{norm} = -2.1 + 1.3\,i$, $r/\omega_{norm} = 1.2$, $E = 0.1$, allowing one to localize simultaneously the three most unstable modes, appears in full line. The radial computation domain is taken $0.4 < s < 0.7$, so as to be centered on the mode rational surface $s_0 = 0.548$ ($q_s(s_0) = m/n$). When solving in configuration space, typically $n_\rho = 100$ finite elements are needed and $n_\nu = 50$ points for the ν integrations appearing in the coupling elements, to obtain good convergence (accuracy of $\sim 1\%$) of the most unstable mode. Fig.3.3 shows the convergence of the growth rate of the most unstable mode. Fig.3.4 a) depicts the corresponding mode computed in radial Fourier space, Fig.3.4 b) the same field transformed to configuration space and Fig.3.4 c) the poloidal structure. When solving in Fourier space, equilibrium is sampled with typically $n_\rho = 64$ points and the perturbation is represented with $2k_{max} + 1 = 121$ radial Fourier components. Considering GC drifts, the velocity integrals were performed using 10-20 points per thermal velocity. When approaching marginal stability the number of points must be increased so as to integrate correctly the resonant denominator.

In Fig.3.5 the mode numbers (m, n) are increased proportionally so as to hold the ratio $m/n = 1.6$ unchanged and the mode localized around the same rational surface.

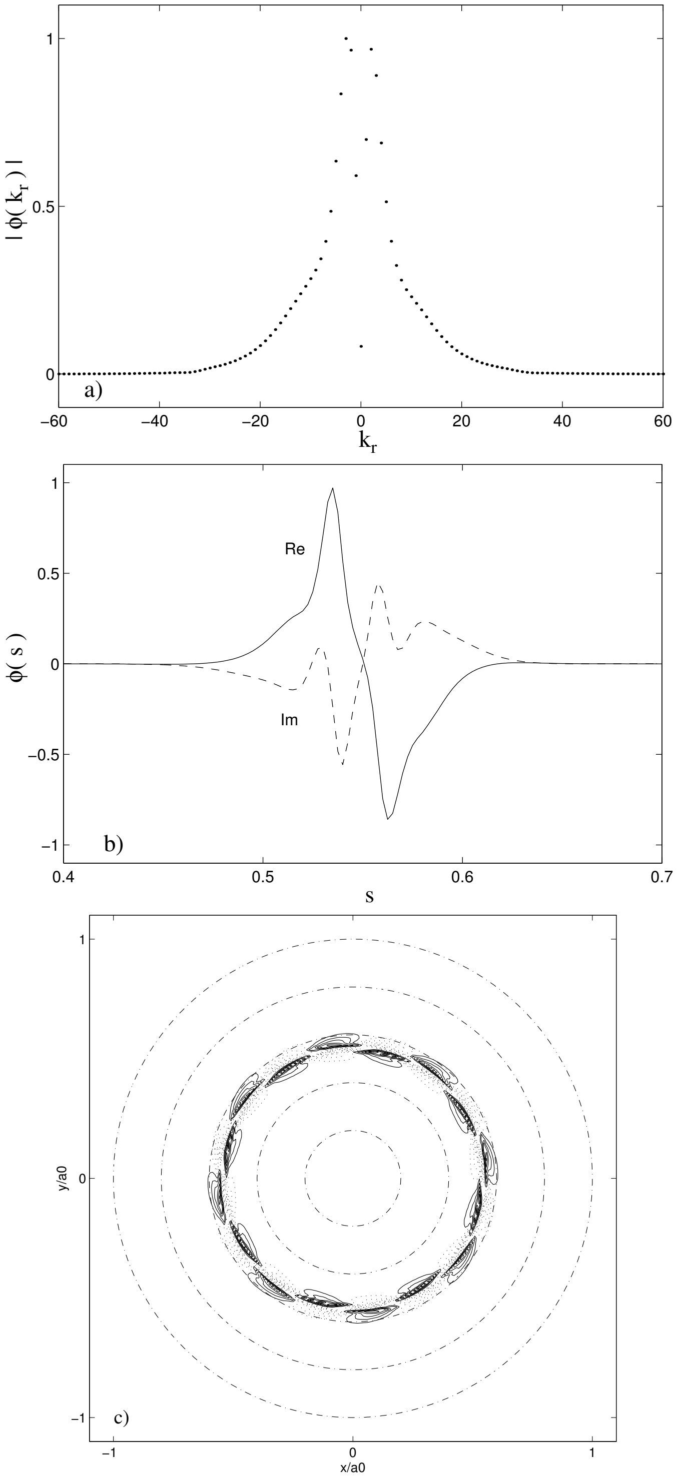

Figure 3.4: a) Radial Fourier representation of the most unstable mode (m=8, n=5). b) The same field transformed to configuration space. Full and dashed lines are respectively real and imaginary part. c) Corresponding poloidal structure. These results were obtained using the method in Fourier space.

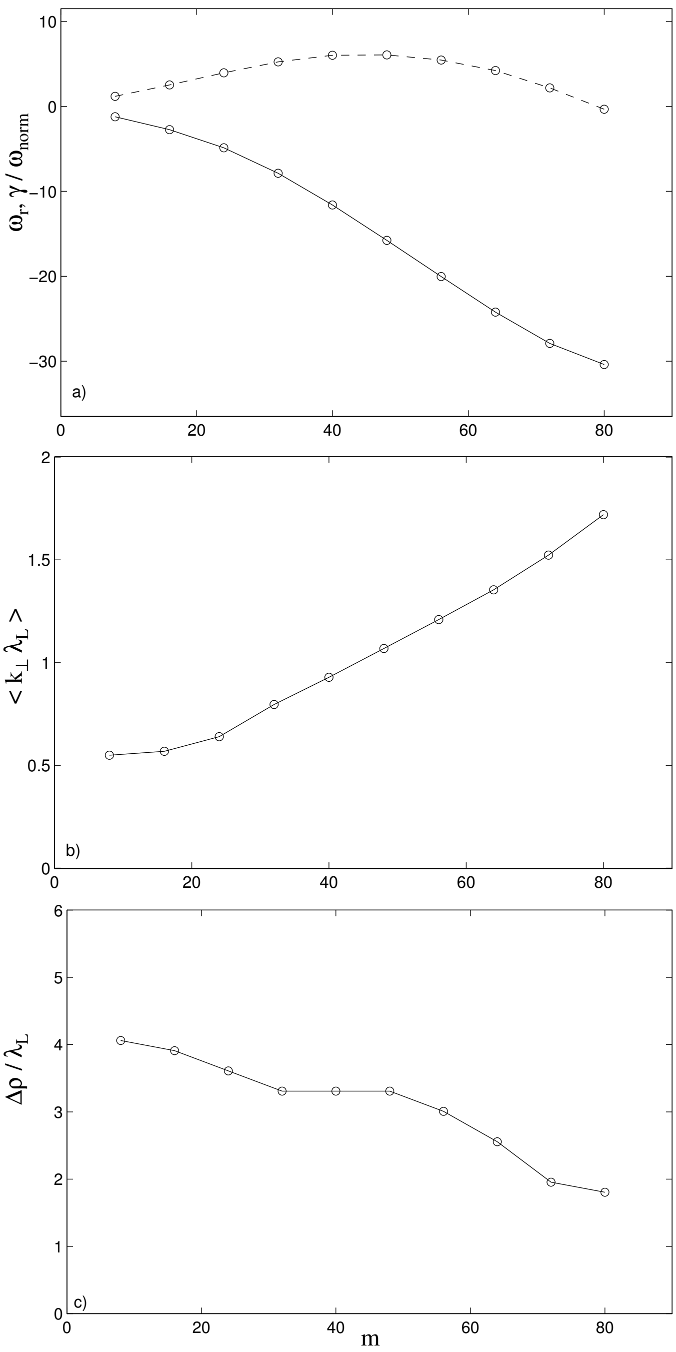

Figure 3.5: a) Normalized frequency and growth rate of the most unstable mode with respect to m holding $m/n = 1.6$ fixed. b) Average value of $k_\perp \lambda_{Li}$. c) Radial width normalized to λ_{Li}. These results were obtained with the method in configuration space and checked with the Fourier approach.

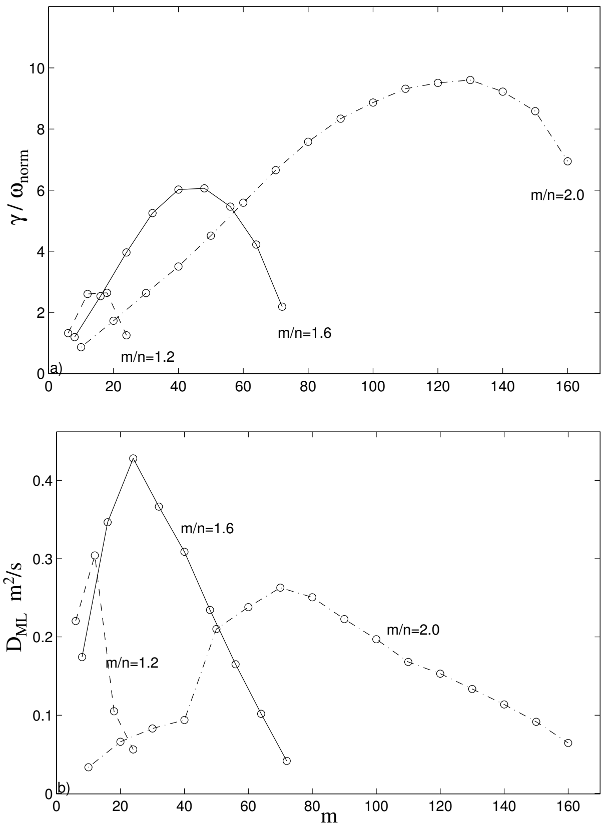

Figure 3.6: a) Growth rate of the most unstable mode with respect to m holding successively $m/n = 1.2, 1.6, 2.0$ fixed. b) Corresponding mixing length estimate $D_{ML} = \gamma/k_\perp^2$ for diffusion coefficient.

Fig.3.5 a) shows the normalized frequency and growth rate as a function of m. The perpendicular wave number normalized with respect to the ion Larmor radius is averaged over the eigenfunction of the most unstable mode and plotted in Fig.3.5 b). The growth rate peaks as $< k_\perp \lambda_{Li} >$ goes through 1, typical for slab-ITG instabilities. The root mean squared width, normalized with respect to λ_{Li}, is given in Fig.3.5 c). Similar scans were repeated for two other rational surfaces $s_0 = 0.316$ ($m/n = 1.2$) and $s_0 = 0.707$ ($m/n = 2.0$). The growth rates of the most unstable modes are plotted in Fig.3.6 a) and the diffusion coefficient $D_{ML} = \gamma/k_\perp^2$ based on the mixing length estimate[64] in Fig.3.6 b). All these values were computed in configuration space and checked by the Fourier space method.

Chapter 4

Going to Torus

The goal of this chapter is to show how the methods developed in cylinder can be generalized to a toroidal model. Trapped particles are neglected here so that the only toroidal effect retained are the drifts induced on the GC trajectories of circulating particles. This defines an appropriate model for studying the transition from slab- to toroidal-ITG instabilities. Numerical results are benchmarked with a global, linear, time evolution code and compared with parameter scans obtained using a ballooning representation approximation.

4.1 A Simple Model for Toroidal-ITG Instabilities

Let us consider the large aspect ratio equilibrium with circular cross-section (2.6). Furthermore the modulation of the magnetic field along the GC trajectories is neglected here, so that the velocity components $(v_\parallel, v_\perp)$ remain constant. Thus trapped particles are not taken into account and the only remaining toroidal effect are the toroidal GC drifts which are essentially vertical:

$$\vec{v}_d = \frac{1}{\Omega}\left(\frac{v_\perp^2}{2} + v_\parallel^2\right)\frac{1}{R}\,\vec{e}_z = v_{dz}\,\vec{e}_z,$$

the cyclotron frequency $\Omega = qB_0/m$ being evaluated with the magnetic field on axis. The much smaller drifts related to the finite safety factor profile are neglected.

The eigenvalue equation for the electrostatic potential will again be formulated through the quasineutrality relation

$$\tilde{n}_e = \tilde{n}_i, \tag{4.1}$$

and the electron contribution reduced to the adiabatic response:

$$\tilde{n}_e = \frac{e\phi}{T_e} N.$$

Non-adiabatic electron dynamics will be considered in the next chapter. The perturbed ion density, derived from the GKE and expressed in terms of the propagator $\mathcal{P}$, is given by Eq.(A.13):

$$\tilde{n}_i = \frac{e}{T_i} \left[-N\phi - \int d\vec{k}\, e^{i\vec{k}\cdot\vec{r}}\, \hat{\phi}(\vec{k}) \int d\vec{v}\, J_0^2(x_L) F_M \left(\omega - \omega^\star\right) i\mathcal{P} \right],$$

defining $x_L = k_\perp v_\perp / \Omega$.

As in cylinder, the plane wave decomposition of $\phi(\vec{r})$ is transcribed to a representation more adapted to the magnetic geometry. Thus, a toroidal wave decomposition is chosen:

$$\int d\vec{k}\, e^{i\vec{k}\cdot\vec{r}}\, \hat{\phi}(\vec{k}) \longrightarrow \sum_{(k,m)} \hat{\phi}_{(k,m)} \exp i(\kappa\rho + m\theta + n\varphi), \tag{4.2}$$

where the toroidal wave number n can be fixed due to axisymmetry. In view of solving the final eigenvalue equation in Fourier space, a Fourier series in the radial direction is chosen from the start instead of a Fourier transform. The local wave vector therefore reads:

$$\vec{k} \longrightarrow \kappa\nabla\rho + m\nabla\theta + n\nabla\varphi = \kappa\, \vec{e}_\rho + k_\theta\, \vec{e}_\theta + k_\varphi\, \vec{e}_\varphi,$$

with $\kappa = k2\pi/\Delta\rho$, $\Delta\rho = \rho_u - \rho_l$ being the width of the considered interval, $k_\theta = m/\rho$ and $k_\varphi = n/R$. What remains to be evaluated is the propagator Eq.(A.10):

$$\mathcal{P} = \int_{-\infty}^{0} dt \exp i \left[\vec{k} \cdot (\vec{R}' - \vec{R}) - \omega t \right].$$

When calculating the phase

$$\vec{k} \cdot (\vec{R}'(t) - \vec{R}) \longrightarrow \int_0^t dt'\, \vec{k} \cdot \vec{v}_g\, (\vec{R}'(t')),$$

the drifts $\vec{v}_d$ appearing in the GC velocity $\vec{v}_g = v_\parallel \vec{e}_\parallel + \vec{v}_d$ are at first neglected, so that the trajectories follow the magnetic field lines. In toroidal coordinates these lowest order trajectories are trivial to integrate as $v_\parallel$ is assumed constant:

$$\left\{\begin{array}{lcl} \rho' & = & \rho \\ \theta' & = & \theta - \omega_t t \\ \varphi' & = & \varphi + \frac{v_\parallel}{R} t \end{array}\right. \tag{4.3}$$

where $\omega_t = v_\parallel / R q_s$ is the transit frequency. The contribution to the phase factor coming from drifts is then evaluated iteratively by integrating along (4.3):

$$\begin{aligned} \vec{k} \cdot (\vec{R}' - \vec{R}) &= k_\parallel v_\parallel t + \int_0^t dt' \, \vec{k} \cdot \vec{v}_d = k_\parallel v_\parallel t - \int_0^t dt' k_\perp v_{dz} \cos(\theta' + \theta_{\vec{k}}) \\ &= k_\parallel v_\parallel t + \frac{k_\perp v_{dz}}{\omega_t} \left[\sin(\theta' + \theta_{\vec{k}}) - \sin(\theta + \theta_{\vec{k}}) \right], \end{aligned}$$

having used

$$k_z = -(\kappa \sin\theta + k_\theta \cos\theta) = -k_\perp \cos(\theta + \theta_{\vec{k}}), \tag{4.4}$$

with $k_\parallel = (n q_s - m)/R q_s$, $k_\perp = \sqrt{\kappa^2 + k_\theta^2}$ and $\theta_{\vec{k}}$ such that

$$\cos\theta_{\vec{k}} = \frac{k_\theta}{k_\perp}, \qquad \sin\theta_{\vec{k}} = -\frac{\kappa}{k_\perp}.$$

The drift term gives rise to the actual finite orbit width (FOW) effects as it is proportional to $x_t = k_\perp v_{dz}/\omega_t \sim k_\perp \lambda_t$, with $\lambda_t = q_s \lambda_L$ the average radial GC excursion. These effects induce poloidal mode number coupling as well as radial coupling related respectively to the θ and κ dependence in (4.4). With the help of relation [60]:

$$\exp(iz \sin\theta) = \sum_{p=-\infty}^{+\infty} J_p(z) e^{ip\theta},$$

the propagator can be integrated:

$$\begin{aligned} \mathcal{P} &= \int_{-\infty}^{0} dt \exp i \left[(k_\parallel v_\parallel - \omega) t + x_t \left(\sin(\theta' + \theta_{\vec{k}}) - \sin(\theta + \theta_{\vec{k}}) \right) \right] && (4.5) \\ &= \sum_{p,p'=-\infty}^{+\infty} \frac{J_p(x_t) J_{p'}(x_t)}{i(k_\parallel v_\parallel - p\omega_t - \omega)} \exp i(p - p')(\theta + \theta_{\vec{k}}). && (4.6) \end{aligned}$$

The resonances now appear explicitly. A particle will resonate with a wave component $(\vec{k}, \omega)$ if its motion along the magnetic line is in phase or if it feels a Doppler shifted frequency equal to a harmonic of the transit frequency ω_t. This is comparable to cyclotron harmonic resonances at the level of the Larmor rotation, except that here one is dealing with the large scale periodic motion of the GC in the poloidal plane. In appendix B, (4.6) is rederived from the general relation for the propagator obtained by solving Eq.(A.12) in an arbitrary toroidal system.

It was shown in the previous chapter that solving the eigenvalue equation in Fourier instead of configuration space has various advantages. This choice is even more crucial here due to the more complicated trajectories. Hence, writing the quasineutrality condition in this representation after having inserted (4.6) or (4.5) in $\widetilde{n}_i$ leads to the eigenvalue equation

$$\sum_{(k',m')} M_{(k,m),(k',m')}(\omega) \overset{\wedge}{\phi}_{(k',m')} = 0, \tag{4.7}$$

where the matrix elements $M_{(k,m),(k',m')}$ are either given by

$$\begin{aligned} M_{(k,m),(k',m')}(\omega) = \frac{1}{\Delta\rho} \int_{\rho_l}^{\rho_u} d\rho e^{-i(\kappa-\kappa')\rho} \Bigg[& \left(\frac{1}{\tau} + 1\right) \delta_m^{m'} \\ + \quad e^{i(m-m')\theta_{\vec{k}'}} & \int d\vec{v}\, J_0^2(x_L') \frac{F_M}{N} (\omega - \omega^\star) \sum_{p=-\infty}^{+\infty} \frac{J_p(x_t') J_{p'=p-m+m'}(x_t')}{k_\parallel' v_\parallel - p\omega_t - \omega} \Bigg], \end{aligned} \tag{4.8}$$

when using the harmonic decomposition, or by

$$\begin{aligned} M_{(k,m),(k',m')}(\omega) = {} & \frac{1}{\Delta\rho} \int_{\rho_l}^{\rho_u} d\rho e^{-i(\kappa-\kappa')\rho} \Bigg[\left(\frac{1}{\tau} + 1\right) \delta_m^{m'} \\ + \quad & e^{i(m-m')(\theta_{\vec{k}'} - \frac{\pi}{2})} i \int_{-\infty}^{0} dt e^{-i\omega t} \int d\vec{v}\, J_0^2(x_L') \frac{F_M}{N} (\omega - \omega^\star) \cos(\bar{k}_\parallel\, v_\parallel t) J_{m-m'}(x_t' \omega_t t \,\mathrm{sinc} \frac{\omega_t t}{2\pi}) \Bigg], \end{aligned} \tag{4.9}$$

when keeping the time integration. The following definitions have been used, $\tau = T_e/T_i$, $\bar{k}_\parallel = [nq_s - (m + m')/2] / Rq_s$ and $\mathrm{sinc}(x) = \sin(\pi x)/\pi x$.

When unbending the torus in order to recover the cylindrical system of chapter 3, the major radius R is increased while holding

$$Rq_s = \text{const}, \qquad \frac{n}{R} = \text{const} \qquad \text{and} \qquad a = \text{const},$$

as well as all other equilibrium profiles. As expected, the FOW $\lambda_t = q_s \lambda_L$ vanishes so that the poloidal coupling disappears and relation (4.7) reduces to (3.37) for each poloidal mode number m.

4.2 Numerical Method

Equation (4.7) defines a two-dimensional eigenvalue equation in Fourier space (k, m). Owing to the Fourier series decomposition, the system is already discretized and cast in matrix form. One must however still reduce this infinite system by identifying the finite number of significant matrix elements $M_{(k,m),(k',m')}$.

The numerical implementation of the time integration form (4.9) is delicate as it must produce all the resonances that appear explicitly in (4.8). For computation we shall therefore choose the harmonic decomposition although relation (4.9) will be useful for interpretation as it is more transparent in other respects.

Radial Mode Components

Concerning the significant radial Fourier components and their coupling, the situation is basically the same as in cylinder (see Sect.3.2.2). However, k_{max} can often be reduced from condition (3.39) when computing for toroidal-ITG instabilities as they usually have a smoother radial dependence then slab-ITG. The numerical integration over ρ is again performed on an equidistant mesh using an FFT algorithm.

Poloidal Mode Components

As $|k_\parallel|\lambda_L \ll 1$ for both the slab- and toroidal-ITG instability, the significant poloidal mode components are those for which the corresponding mode rational surface $\rho = \rho_m$ ($q_s(\rho_m) = m/n$), lies inside the unstable region. A good estimate of this radial interval is obtained on the basis of the local stability conditions discussed in chapter 2. The coupling between a poloidal mode component and its neighboring values appears explicitly in (4.9) where the FOW effects are gathered compactly in the form of a single Bessel function of order $m - m'$ and average argument $\sim k_\perp \lambda_t$. Hence, the poloidal coupling is dominant between mode numbers m and m' such that

$$|m - m'| \overset{\sim}{<} k_\perp \lambda_t,$$

since $J_p(x)$ is a decreasing function of p for $p > x$. Convergence studies have shown that one should typically retain matrix elements with $|m - m'| \leq \Delta m_{max} = 4 k_\perp \lambda_t$.

Harmonics of Transit Frequency

To determine which orders of the harmonic decomposition must be taken into account, one must not only consider the resonant denominators but also the weight of the numerators corresponding to the bulk response. A particle with average parallel velocity $< v_\parallel > \sim \sigma v_{th\,i}$ will resonate with the harmonic of order

$$p = p_r \simeq -\sigma \frac{\omega_r}{< \omega_t >} \pm 1,$$

using the fact that $k_\parallel \simeq \pm 1/Rq_s$ for toroidal ITG-instabilities and the notations $< \omega_t >= v_{th\,i}/Rq_s$ for the average transit frequency and $\omega_r = \Re e(\omega)$. The estimate $\omega_r \sim \omega^\star \sim v_{th\,i} k_\theta \lambda_{L\,i}/L$ leads to $|p_r| \sim k_\theta \lambda_{L\,i} R q_s / L$, L being a characteristic length of equilibrium. The numerators however are dominant for

$$|p| \overset{\sim}{<} k_\perp \lambda_t.$$

Combining these two conditions, one typically considers the harmonics

$$\min\left(-\sigma \frac{\omega_r}{< \omega_t >} - \Delta p_{extra}, -4 k_\perp \lambda_t\right) < p < \max\left(-\sigma \frac{\omega_r}{< \omega_t >} + \Delta p_{extra}, 4 k_\perp \lambda_t\right)$$

for particles with $\mathrm{sign}(v_\parallel) = \sigma$, the term $\Delta p_{extra} \sim 3$ chosen so as to ensure convergence.

Velocity Integrals

Tackling the velocity integrals, the infinite domain is again reduced to a sphere $\mathsf{v} < \mathsf{v}_{max} \sim 5$, with $\vec{\mathsf{v}} = \vec{v}\,/v_{th\,i}$, and an extended trapezoidal rule is applied in both the parallel and perpendicular direction. Note that when $v_\parallel$ tends to zero for finite $v_\perp$, the Bessel functions $J_p(x_t)$ oscillate rapidly. Although the parallel velocity integral is well defined in this limit, as shown clearly by Eq.(4.9), it makes numerical implementation more difficult. To avoid this problem, only the actual circulating particles are considered so that $v_\parallel > \sqrt{B_{max}/B - 1}\, v_\perp$, where $B(\rho, \theta)$ is replaced by its surface averaged value B_0, and $B_{max}(\rho)/B_0 = (1 + A^{-1})$ is the maximum field on the considered surface. Consequently, the adiabatic response must be weighted by the fraction of circulating particles:

$$\alpha_t = 1 - \sqrt{1 - B_0/B_{max}(\rho)}.$$

Final Numerical Form

Taking into account the above, the matrix elements are evaluated as follows:

$$\begin{aligned} & M_{(k,m),(k',m')}(\omega) = \\ & \quad \frac{1}{\Delta\rho} \int_{\rho_l}^{\rho_u} d\rho e^{-i(\kappa-\kappa')\rho} \left\{ \alpha_t \left(\frac{1}{\tau} + 1 \right) \delta_m^{m'} + e^{i(m-m')\theta_{\vec{k}'}} \frac{1}{\sqrt{2\pi}} \sum_{\sigma=\pm 1} \int_0^{\mathsf{v}_{max}} d\mathsf{v}_\parallel e^{-\frac{1}{2}\mathsf{v}_\parallel^2} \times \right. \\ & \quad \left. \sum_{p=p_{min}(\sigma)}^{p_{max}(\sigma)} \left. \frac{\left[\omega - \omega_n \left(1 + \eta(\mathsf{v}_\parallel^2 - 3)/2\right)\right] \hat{I}_0(p,p') - \omega_n \eta \hat{I}_1(p,p')/2}{< \omega_t > (n q_s - m' - p)\sigma \mathsf{v}_\parallel - \omega} \right|_{p'=p-m+m'} \right\}, \qquad (4.10) \end{aligned}$$

all equilibrium quantities being function of ρ. As the perpendicular velocity integrals are independent of frequency, they can be precalculated:

$$\begin{aligned} \hat{I}_n\left(q_s, \tilde{k}_\perp', \sigma\mathsf{v}_\parallel, p, p'\right) &= \int_0^{\mathsf{v}_{\perp max}(\rho)} \mathsf{v}_\perp^{2n+1} d\mathsf{v}_\perp e^{-\frac{1}{2}\mathsf{v}_\perp^2} J_0^2(x_L') J_p(x_t') J_{p'}(x_t'), \qquad (4.11) \\ x_L' &= \tilde{k}_\perp' \,\mathsf{v}_\perp, \qquad x_t' = \tilde{k}_\perp' \, q_s \frac{1}{\sigma\mathsf{v}_\parallel} \left(\frac{\mathsf{v}_\perp^2}{2} + \mathsf{v}_\parallel^2 \right), \\ \mathsf{v}_{\perp max} &= \min(\mathsf{v}_\parallel/\sqrt{A^{-1}}, \mathsf{v}_{\ max}), \end{aligned}$$

with $\tilde{k}_\perp = k_\perp \lambda_L$.

The eigenvalues and corresponding eigenvectors of Eq.(4.7), using (4.10), are obtained applying the same methods which have first been tested in the cylindrical geometry (see section 3.2.3).

4.3 Computer Implementation

The central coding is written in FORTRAN 77. The NAG library provides subroutines for performing FFT and for evaluating most special functions. The LAPACK library is used for factorizing and evaluating the determinant of $M(\omega)$, considered as a full matrix, as well as for solving the corresponding linear system when computing the eigenvectors. Carrying out a frequency scan to determine the eigenvalues involves first precalculating the perpendicular velocity integrals (4.11) followed by building the matrix and calculating the corresponding determinant at each point. With respect to the main parameters the number of operations, and thus on a scalar machine the time spent for building the matrix, scales approximately as

$$\sim n_\rho n_k n_m (2\Delta m + 1) n_p n_{v_\|},$$

and for evaluating the determinant

$$\sim (n_k n_m)^3,$$

with

n_ρ: # of radial points for sampling equilibrium,

n_k: # of radial Fourier components for representing ϕ,

n_m: # of poloidal Fourier components,

Δm: coupling width between poloidal mode numbers,

n_p: # of harmonics of transit frequency,

$n_{v_\|}$: # of parallel velocity points for integration.

Presently the code is run on a Silicon Graphics Indigo 2 with a R10000 processor operating at 175 MHz. A typical toroidal run with $n_\rho = 64$, $n_k = 50$, $n_m = 15$, $\Delta_m = 5$, $n_p = 8$,

$n_{v_\parallel} = 60$ takes $\sim 25s$ cpu time for computing the matrix and $\sim 10s$ for evaluating the determinant. To identify a full spectrum this must be repeated for tens to hundreds of frequency points, so that heavy runs can last a few hours. It follows from the above scalings that in a cylindrical case these numbers can be divided by a factor ~ 500.

In toroidal cases the time spent for precalculating the perpendicular velocity integrals $\hat{I}_n$, $n = 0, 1$ is of the same order as building $M(\omega)$ and calculating $\det M(\omega)$ at one frequency point and therefore becomes negligible over such a scan. As shown in relation (4.11), the values of these integrals can be stored in a table parameterized by $(q_s, \tilde{k}_\perp, v_\parallel, p, p')$. This table is then read using a zero order interpolation rule with respect to q_s and $\tilde{k}_\perp$. Some evident symmetry properties of $\hat{I}_n$ such as the invariance under the permutation of p and p' or others related to the parity of the Bessel function allow one to reduce the number of values to be calculated and stored. Nevertheless, they occupy the main part of the memory required, followed by the space needed for storing the matrix itself so that altogether typically $\sim$ 100Mbytes must be available.

The raw data provided by the central code is analyzed and visualized using the MATLAB application.

4.4 Results

4.4.1 Benchmarking with Time Evolution PIC Codes

As already mentioned, the spectral method presented here is being developed simultaneously with another global linear code, which uses a time evolution, particle in cell (PIC) approach[35]. The starting equations for these two techniques are basically the same: a gyrokinetic equation for ions, assuming at this stage of the discussion adiabatic electrons and closure with the quasineutrality condition. This has been useful for benchmarking. The frequency, growth rate and field structure given by the time evolution code must match, asymptotically in time, the eigenfrequency with the highest growth rate of the spectrum as well as the corresponding eigenmode. However these comparisons must be carried out carefully as for practical reasons different approximations have been made. The PIC code contains trapped ion dynamics, which are neglected in the spectral approach. This naturally leads to disagreements at frequencies near or below the average ion bounce frequency. On the other hand the eigenvalue code retains all FLR effects of ions while the time evolution approach only retains these terms to second order. This simplification is reasonable for a toroidal-ITG instability whose growth rate peaks at $k_\perp \lambda_{L\,i} \sim 0.5$ but becomes marginal for a slab-ITG peaking at $k_\perp \lambda_{L\,i} \sim 1$. Nevertheless, there is a large common range of parameters within these different approximations. Some of these comparisons will be shown in the following results, more details are given in reference[37].

In one particular case results of the linear stage of the non-linear PIC code written by Sydora, Decyk and Dawson[34, 33] containing full ion dynamics are also presented. For the sake of the comparisons appearing in this chapter non-adiabatic trapped electron dynamics, usually contained in these simulations, have been suppressed.

4.4.2 Comparing with Local Ballooning results

Results by Dong et al. in references [24] and [41] are useful as they have considered locally on a magnetic surface - applying the ballooning approximation - the same model as we do, that is a large aspect ratio torus, neglecting trapped ions as well as the modulation of the parallel velocity of circulating ions. As will be shown, comparisons with their parameter scans have allowed further validation of our global results but also bring to the fore the limits of the ballooning approximation. By normalizing the frequency with respect to $v_{th\,i}/L_n$, these ballooning results can be parameterized by the six independent parameters q_s, $\hat{s}$, $\tau = T_e/T_i$, $\epsilon_n = L_n/R$, $\eta_i = L_n/L_{T_i}$ and $\tilde{k}_\theta = n q_s \lambda_{L\,i}/\rho_0$ (see Eq.(2.46)), emphasizing that all these quantities are evaluated locally on a magnetic surface $\rho = \rho_0 =$const. However a global mode simulation, by the choice of the different profiles, has infinite degrees of freedom. Indeed, (4.10) shows that such a spectrum is determined by fixing the magnetic geometry with the major radius R, the minor radius a, the safety factor profile $q_s(s)$, by giving density and temperature profiles $N(s)$, $T_e(s)$, $T_i(s)$ and finally by fixing the toroidal mode number n. Note that once the frequency has been normalized for instance with respect to $v_{thi,0}/a$, where $v_{thi,0}$ is the ion temperature at a point of reference, varying the magnetic field on axis B_0 is equivalent to varying the amplitude of the ion temperature and therefore is not an additional independent parameter. For comparison these profiles must match the local ballooning parameters at $\rho = \rho_0$. Furthermore for the local results to be relevant, the global modes must actually be localized around this magnetic surface[20]. This is obtained by peaking the η_i profile in this region. Ideally one would compare the most unstable global eigenmode and eigenfrequency with a set of ballooning results relative to different radial positions, which may give a better idea of how these local results must be interpreted. This has not yet been done as it would require specific results from such a code.

4.4.3 Equilibrium Profiles

The profiles defined here have been used for all results presented in this chapter and the following.

For density and temperature the same type of dependence is chosen:

$$\frac{N(s)}{N_0} = \exp\left(-\frac{a\Delta s_n}{L_{n0}}\tanh\frac{s-s_0}{\Delta s_n}\right), \tag{4.12}$$

$$\frac{T(s)}{T_0} = \exp\left(-\frac{a\Delta s_T}{L_{T0}}\tanh\frac{s-s_0}{\Delta s_T}\right), \tag{4.13}$$

where $s = \rho/a$ is the normalized radial variable and Δs the radial width over which these profiles vary. L_0 stands for the characteristic length of variation at $s = s_0$, as shown explicitly in the case of density by

$$\left(\frac{d\ln N}{d\rho}\right)^{-1} = -L_{n0}\cosh^2\frac{s-s_0}{\Delta s_n}.$$

The η dependence thus is given by

$$\eta(s) = \frac{d \ln T}{d \ln N} = \frac{L_{n0}}{L_{T0}} \frac{\cosh^2 \frac{s-s_0}{\Delta s_n}}{\cosh^2 \frac{s-s_0}{\Delta s_T}},$$

which peaks at s_0 if $\Delta s_n > \Delta s_T$. Examples of such profiles are given in Fig.4.14.

For the safety factor a fourth order polynomial of the form

$$q_s(s) = q_s(0) + as^2 + bs^3 + cs^4,$$

gives a good fit for many cases including central negative shear scenarios. It allows for instance fixing the safety factor on axis $q_s(0)$, on the edge $q_s(1)$ as well as its value $q_s(s_0)$ and shear $\hat{s}(s_0)$ at an intermediate point s_0 as shown in Fig.4.19.

4.4.4 Analyzing Mode Structures

As already illustrated in cylinder, it is of interest to evaluate different physical values averaged over the eigenmode structure $\phi(\rho, \theta)$. This is naturally done as follows:

$$< \mathcal{O} > = < \phi | \mathcal{O} \phi >,$$

where $\mathcal{O}$ is an appropriate operator, possibly Hermitian with respect to the scalar product $< | >$, and ϕ normalized so that $< \phi | \phi > = 1$.

In this way the average perpendicular wavelength is defined as

$$< k_\perp > \equiv \sqrt{< k_\rho >^2 + < k_\theta >^2},$$

with

$$< k_\rho >^2 \equiv < \phi | \frac{\partial^2}{\partial \rho^2} \phi >, \quad \text{and} \quad < k_\theta >^2 \equiv < \phi | \frac{1}{\rho^2} \frac{\partial^2}{\partial \theta^2} \phi >,$$

using the scalar product

$$< f | g > = \int_{\rho_l}^{\rho_u} d\rho \int_0^{2\pi} d\theta f^\star g,$$

consistent with the approximation discussed in sec.3.1.3.

However the average guiding center drift frequency

$$< \omega_g > \equiv < \phi | \frac{2T}{qB_0} \frac{1}{R} \frac{1}{i} \frac{\partial}{\partial z} \phi >,$$

is calculated with the usual scalar product

$$< f|g > = \int_{\rho_l}^{\rho_u} \rho d\rho \int_0^{2\pi} d\theta f^\star g. \tag{4.14}$$

In this last case one can also separate the contribution from the radial and poloidal wavelengths:

$$< \omega_g > = < \omega_{g\rho} > + < \omega_{g\theta} >,$$

but one must take

$$\begin{aligned} < \omega_{g\rho} > &\equiv \Re e < \phi | - \frac{2T}{qB_0} \frac{1}{R} \frac{\sin\theta}{i} \frac{\partial}{\partial \rho} \phi >, \\ < \omega_{g\theta} > &\equiv \Re e < \phi | - \frac{2T}{qB_0} \frac{1}{R} \frac{\cos\theta}{i} \frac{1}{\rho} \frac{\partial}{\partial \theta} \phi >, \end{aligned}$$

as these last operators, taken separately, are not Hermitian with respect to (4.14).

4.4.5 Aspect Ratio Scan

To make the connection with the results presented in the previous chapter let us show how the global eigenmodes transform when going from cylinder to torus. Our reference case is a toroidal plasma with inverse aspect ratio $A^{-1} = a/R = 0.18$, its magnetic geometry being given by

$$B_0 = 1.\text{Tesla}, \qquad R = 1.19m, \qquad a = 0.21m, \qquad q_s(s) = 1.25 + 3s^2.$$

Density and electron temperatures are flat, the ion temperature is of the form (4.13) with

$$T_{i0} = T_e = 1.keV, \qquad L_{T_i 0} = 0.16m, \qquad \Delta s_{T_i} = 0.31, \qquad s_0 = 0.5.$$

At $s = s_0$, where the modes tend to be localized, one thus has the local values

$$q_s = 2, \quad \hat{s} = 0.75, \quad \tau = 1, \quad \epsilon_{T_i} = 0.13, \quad \eta_i = \infty, \quad \overset{\sim}{k_\theta} = k_\theta \lambda_{L\,i} = n \cdot 0.06, \quad \frac{a}{\lambda_{L\,i}} = 65.$$

Here frequencies are normalized with respect to

$$\omega_{norm} = \frac{T_{i0}}{eB_0} \frac{1}{a^2} = 2.27 \cdot 10^4 s^{-1}.$$

The ion transit and bounce frequency estimates at $s = s_0$ are then of the order $\omega_{ti} \sim 6\,\omega_{norm}$ and $\omega_{bi} \sim 2\,\omega_{norm}$. This configuration which we call full torus is unbent into a cylinder by increasing R and holding Rq_s, n/R and a constant as well as all other equilibrium profiles. Two particular intermediate states labeled half torus and quarter torus have respectively half and quarter inverse aspect ratio of full torus.

Real frequency ω_r and growth rate γ of the most unstable eigenmodes are plotted in Fig.4.1 as a function of the inverse aspect ratio and labeled by the value of the toroidal mode number n in full torus. Here $n = 4, 7, 10$ are considered. All parameter scans are performed by first computing the full unstable spectrum for the initial, final and a limited number of intermediate values of the parameter. This allows us to identify which eigenmode is the most unstable in each of the so-defined intervals. Two spectra can then be linked by slowly incrementing the parameter and following the eigenvalues of interest with Newton's root finding method. For the scan considered here the full spectra at the four particular aspect ratios mentioned above are recorded in Fig.4.2 for the different toroidal mode numbers. One must in fact specify what is meant by full unstable spectrum. As already mentioned, an increasing number of velocity points are required for integrating the resonant denominator as one approaches marginal stability. Therefore one usually only considers growth rates down to $\gamma/|k_\parallel|v_{th\,i} \simeq 1/20$ which corresponds here for $|k_\parallel| = 1/Rq_s$ to $\gamma \simeq 0.3\,\omega_{norm}$. Starting in cylinder the set of slab-ITG instabilities, localized on the different mode rational surfaces, have similar growth rates and form a well packed spectrum (small circles). With toroidicity these modes couple together and for all n there appears an isolated eigenmode whose growth rate increases faster then all other values. Simultaneously some eigenfrequencies already start to be damped. The prominence of this mode corresponds to the transition to the toroidal-ITG instability.

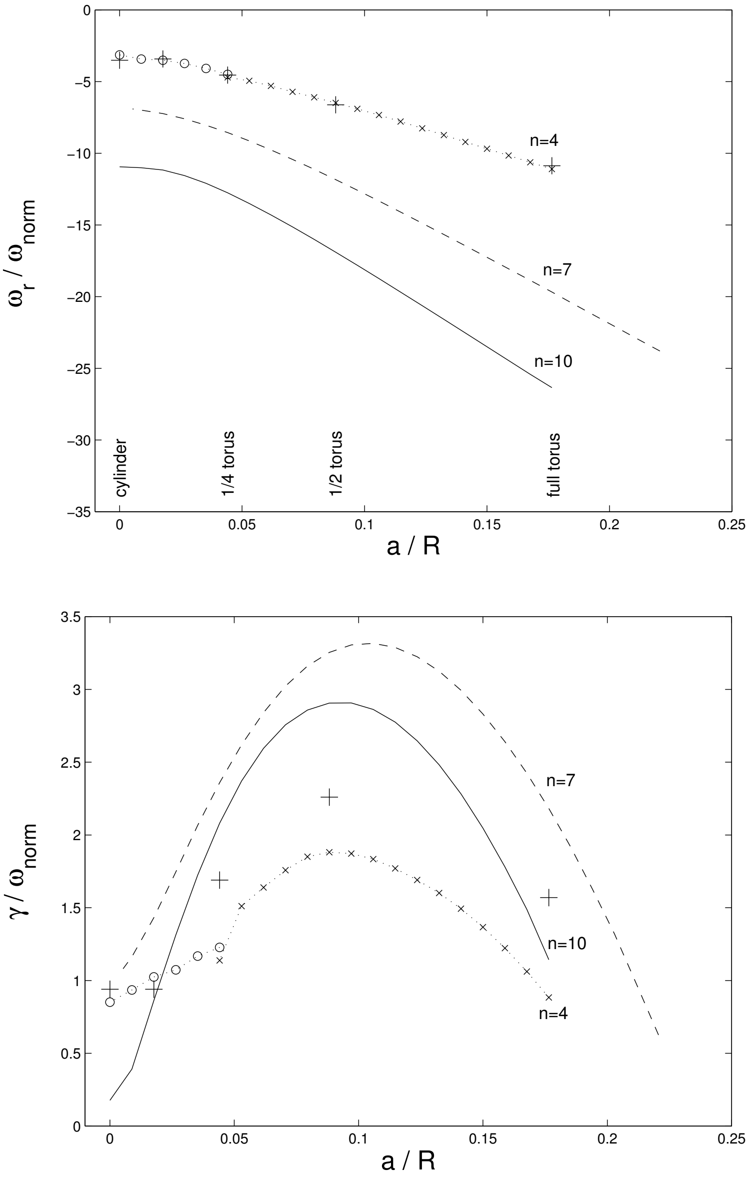

Figure 4.1: Real frequency ω_r and growth rate γ of highest growing eigenmode going from torus to cylinder. At inverse aspect ratio $a/R = 0.18$ called 'full torus' toroidal mode numbers $n = 4, 7, 10$ have been considered. In the case $n = 4$, the line segment from 'cylinder' to '1/4 torus' labeled with circles corresponds to a first eigenmode whose growth rate at $a/R \simeq 0.05$ is taken over by a second eigenmode corresponding to the segment labeled with crosses. For $n = 7, 10$ the most unstable eigenmode remains the same throughout the scan. '+' represent results from the linear PIC code in the case $n = 4$. Here $\omega_{norm} = 2.27 \cdot 10^4 s^{-1}$.

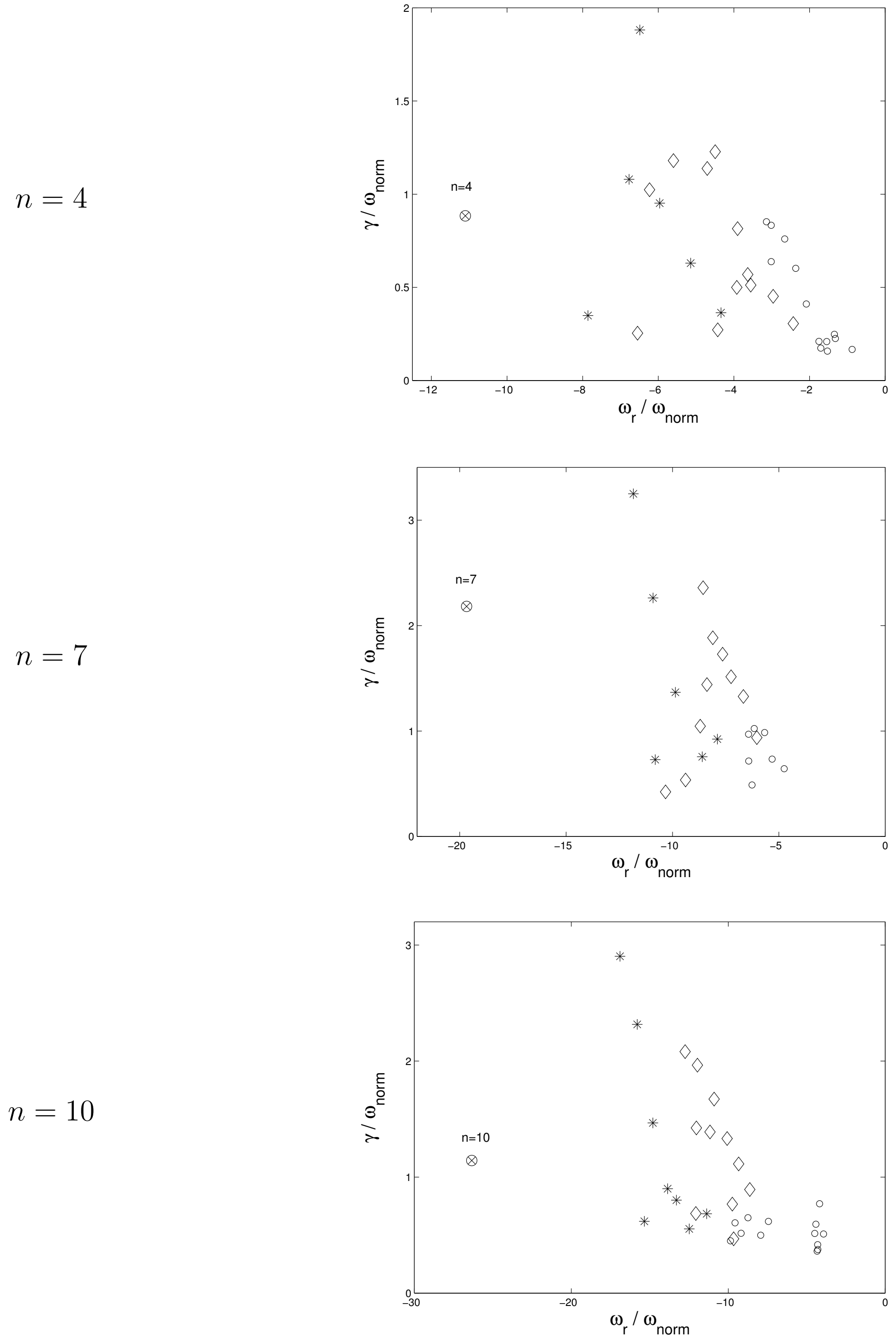

Figure 4.2: Evolution of unstable spectra with varying aspect ratio. Starting in cylinder (small circles) the slab-like eigenmodes couple together with increasing toroidicity. At the transition to the toroidal-ITG instability a particular eigenmode is singled out and is the only one to remain in full torus (large crossed circles). This is observed in all cases $n = 4, 7, 10$. Intermediate spectra are 'quarter torus' (diamonds) and 'half torus' (stars).

As can be seen in Fig.4.2 this occurs after quarter torus for $n = 4$, contrary to $n = 7$ and $n = 10$ which have already undergone transition at this point. This is confirmed by applying the rough estimate (2.36) to the parameters considered here, which would have predicted this conversion to occur at $A^{-1} = 0.10$, 0.03, 0.02 for $n = 4$, 7, 10 respectively as shown in Fig.4.5. In all the cases the highest growth rate is reached near half torus. With even stronger curvature the unstable spectra are limited to the single toroidal-ITG eigenmode whose growth rate also begins to decrease. This is illustrated in Fig.4.2 with the single crossed circle for the full torus state spectra.

For $n = 4$ results of the comparison with the linear PIC[35] code have been plotted in Fig.4.1 with '+' symbols. The two methods agree perfectly on the real part of the frequency, even in cylinder where $k_\perp \lambda_{L\,i} > 1$. Differences in the growth rate of the order 20% appearing in the toroidal-ITG stage are discussed to some extent in the next study.

Notice that for $n = 7$, which is most unstable for all aspect ratios, the scan has been pushed beyond full torus so as to obtain an estimate of the marginal value $\epsilon_{T_ic} \simeq 0.18$, which is somewhat lower then the value $\epsilon_{T_ic} \simeq 0.3$ obtained with the local kinetic dispersion relation in section 2.7 with Fig.2.8.

Plots on the left of Fig.4.3 represent for $n = 4$ the radial dependence of the poloidal Fourier components with increasing toroidicity. Also indicated are the positions of the mode rational surfaces. Plots on the right-hand side give the corresponding structure in configuration space. The dash-dotted lines are the magnetic surfaces $s = 0.2, 0.4, \ldots, 1$. In cylinder the most unstable eigenmode turns out to have poloidal mode number $m = 7$. Quarter torus is the onset of transition where the poloidal modes are already coupled by pairs. At this stage a second eigenmode takes over and gives rise to the true toroidal-ITG instability of half and full torus, nicely centered at $s = s_0 = 0.5$. Coherent radial structures called 'fingers' have now appeared in the unfavorable curvature region where the mode balloons. Their twisting can easily be explained by the increasing of the safety factor towards the edge and using the constant phase relation $q_s(s)\theta =$const from ballooning

Cylinder. The highest growing mode has poloidal wave number $m = 7$ and is centered on the corresponding mode rational surface.

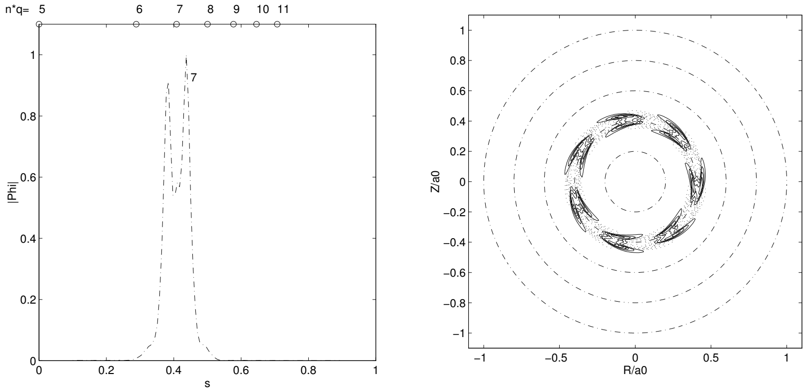

Quarter Torus. The poloidal Fourier components couple by pairs between the corresponding rational surfaces. In configuration space this leads to a broader but very corrugated radial dependence of the eigenmode.

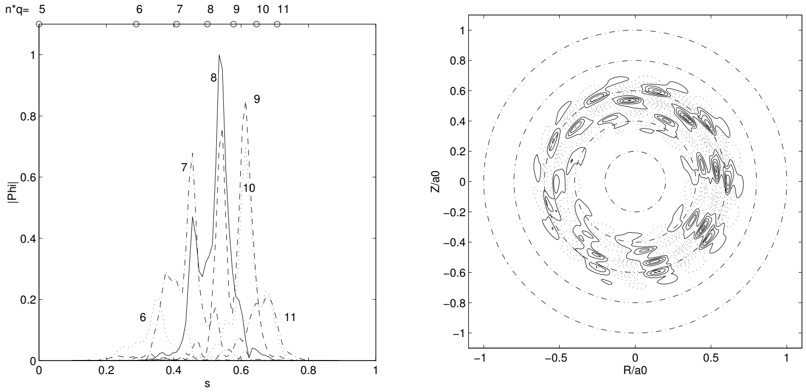

Half Torus. Higher order coupling between the poloidal Fourier components leads to more coherent structures of the eigenmode called 'fingers'. The mode balloons in the unfavorable curvature region. These are the signatures of a toroidal-ITG mode.

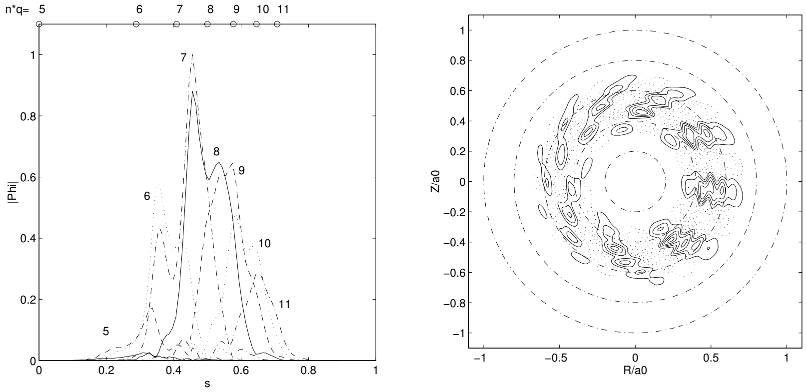

Full torus. The toroidal-ITG characters are confirmed.

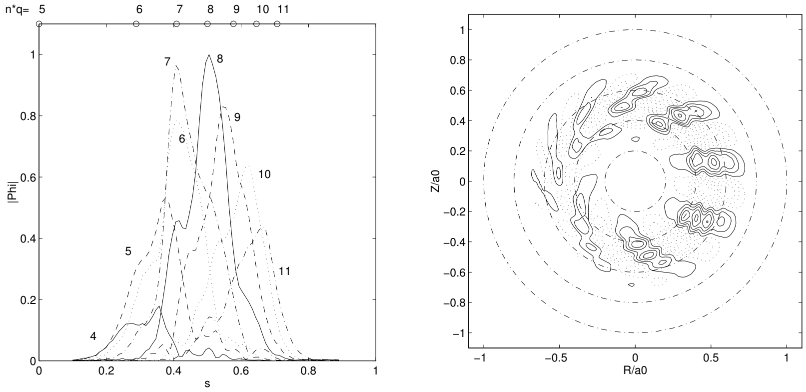

Figure 4.3: Comparing poloidal mode decomposition and mode structures in poloidal plane for toroidicity scan, starting in cylinder and ending in full torus.

representation. Fig.4.4 shows how in cylinder the perpendicular wave number of the order $k_\perp \lambda_{Li} \sim 1.5$ is essentially determined by the narrow radial width of the slab-ITG and decreases as one goes to torus where the radial structure becomes broader and smoother. The average poloidal mode number is $m \simeq nq_s(s_0) = 8$ throughout the scan so that the average poloidal component $k_\theta \lambda_{Li}$ remains approximately constant.

4.4.6 Toroidal Wave Number Scan

Let us first complete the scan in the toroidal wave number for the full torus configuration considered in section 4.4.5. The real frequencies and growth rates from the global spectral code are represented in Fig.4.6 with diamonds. The dotted lines are the least mean square parabolic fits. The growth rate indeed peaks for $n = 7$ where the perpendicular wave number recorded in Fig.4.7 is of the order $k_\perp \lambda_{Li} \simeq 0.5$. For higher toroidal mode numbers $k_\perp$ increases this time essentially as the poloidal component $k_\theta \sim m = nq_s(s_0)$. The corresponding FLR effects suppress the instability for $n \geq 11$. This is confirmed by the PIC results labeled with '+' symbols for the linear code[35] and circles for the linear stage of the non-linear code[34, 33]. For $n = 3$, which from the estimate given in Fig.4.5 corresponds to the transition to the slab-ITG, the spectral calculation resolved no instability. However PIC results measure a growth rate down to $n = 2$. This mismatch for low n may be explained by the appearance of trapped ion effects as the real frequency $\omega_r \sim \omega_g \sim n$ approaches the ion bounce frequency ω_{bi}, even though at $n = 4$ one still has $\omega_r \sim 5\,\omega_{bi}$. The eigenmodes for $n = 4, 7, 10$ are depicted in Fig.4.8. Again the ballooning structure is confirmed as one moves upward from the transition value $n = 3$: the instability is always more localized in the unfavorable curvature region and the radial corrugation indicating the position of the mode rational surfaces, still apparent for n=4, disappears. The set of poloidal Fourier components are then contained under a smooth envelope with decreasing radial width.

A second toroidal wave number scan has been performed with the main goal of illus-

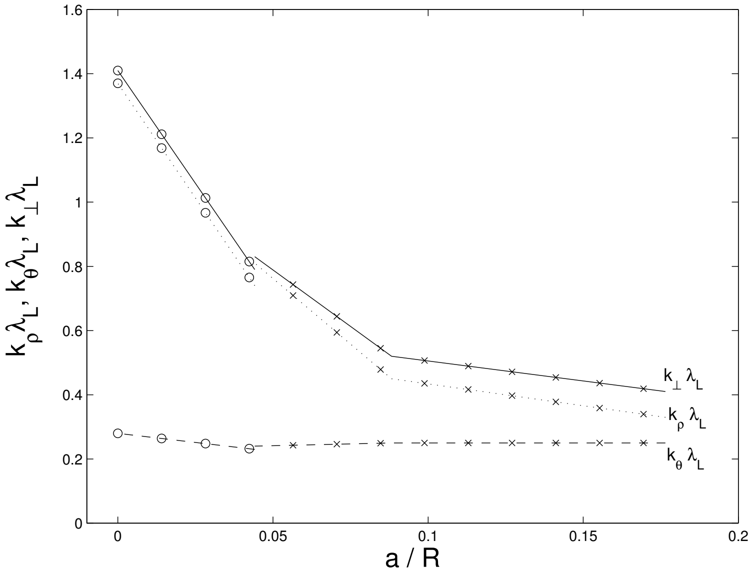

Figure 4.4: Average value of $k_\perp \lambda_{L\,i}$ as a function of the inverse aspect ratio a/R (full line). Also plotted are the average components $k_\rho \lambda_{L\,i}$ (dotted line) and $k_\theta \lambda_{L\,i}$ (dashed line). These results are for toroidal wave number $n = 4$ in full torus. As in Fig.4.1 the segments labeled with circles and crosses correspond to two different eigenmodes.

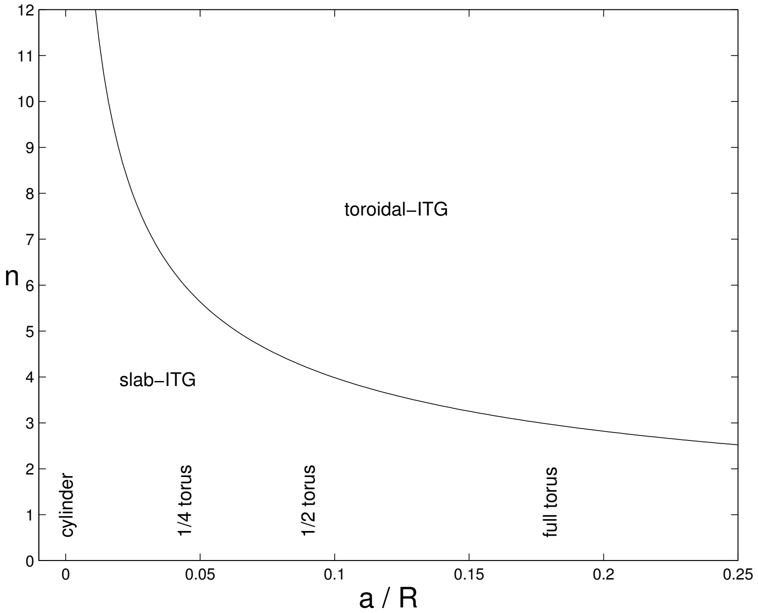

Figure 4.5: Estimate for the transition from slab- to toroidal-ITG instability using the relation $\epsilon_T^{1/2} = \tilde{k}_\theta\ q_s$ for varying inverse aspect ratio a/R and different toroidal wave numbers n in full torus.

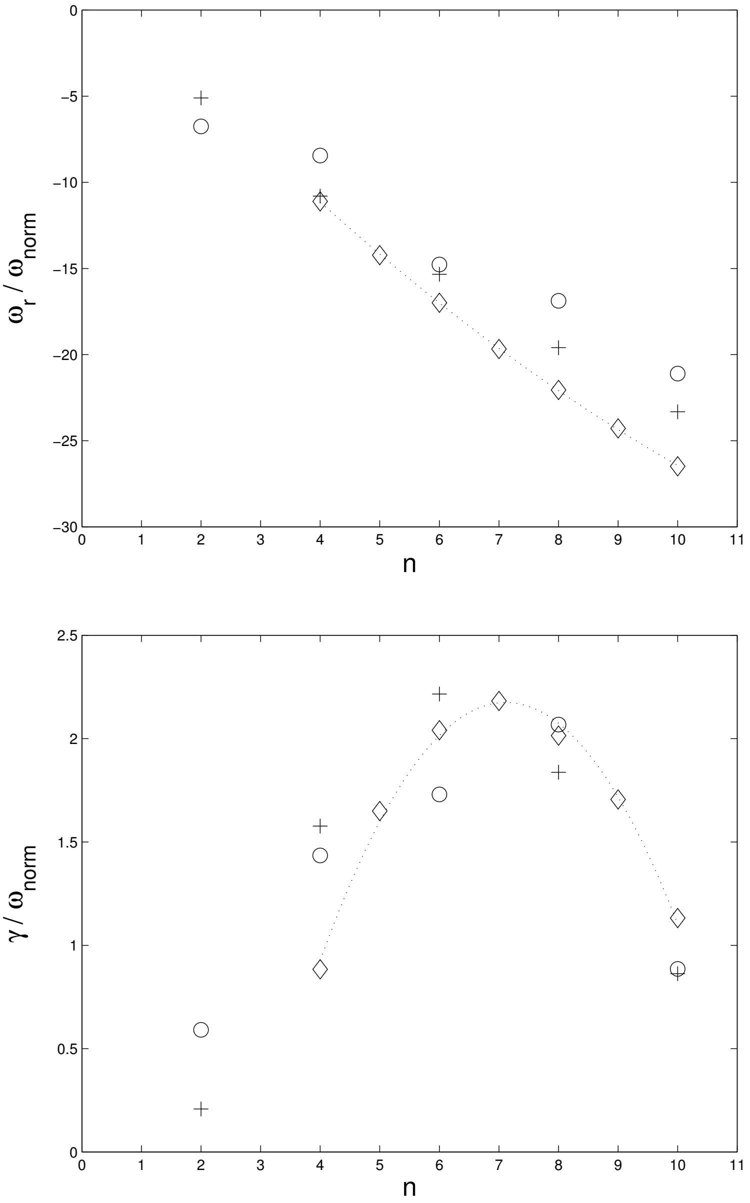

Figure 4.6: Real frequencies ω_r and growth rate γ of most unstable eigenmode for increasing toroidal mode numbers in the full torus configuration of the previous aspect ratio scan. Diamonds represent spectral results, '+' plot linear PIC code results, circles the linear stage of the non-linear PIC code results.

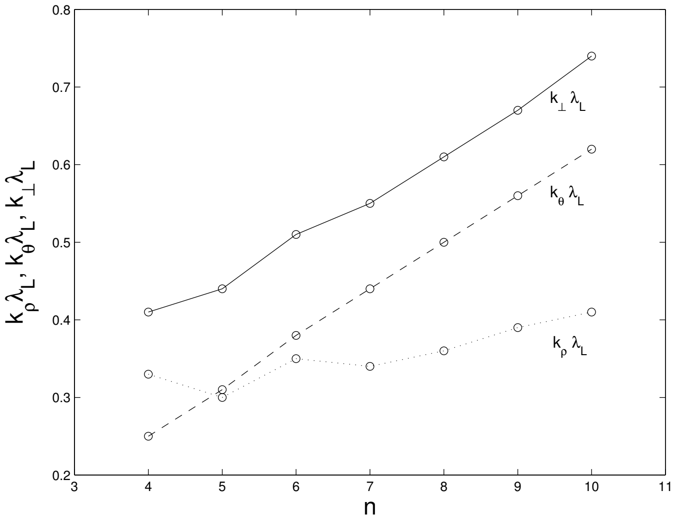

Figure 4.7: Average value of $k_\perp \lambda_{L\,i}$ (full line) as a function of the toroidal wave number n in the full torus configuration. Also plotted are the average components $k_\rho \lambda_{L\,i}$ (dotted line) and $k_\theta \lambda_{L\,i}$ (dashed line).

trating the limits of the local ballooning approximation. For this the $k_\theta \rho^\star$ scan of Fig.3 from reference [24] with parameters $q_s = 2$, $\hat{s}= 1$, $\tau = 1$, $\epsilon_n = 0.2$, $\eta_i = 2$ was chosen. Mind the different normalizations: $k_\theta \rho^\star = \sqrt{2\tau} k_\theta \lambda_{L\,i}$. To perform this comparison a plasma with dimensions similar to DIII-D and matching the local ballooning parameters at $s = s_0 = 0.6$ is defined. Thus the following magnetic geometry is chosen:

$$B_0 = 1.\text{Tesla}, \qquad R = 2.m, \qquad a = 0.5m, \tag{4.15}$$

with a safety factor profile

$$q_s(s) = 1.25 + 0.67s^2 + 2.38s^3 - 0.06s^4,$$

which besides verifying $q_s(s_0) = 2$, $\hat{s}\ (s_0) = 1$ has values $q_s(0) = 1.25$ on the axis and $q_s(1) = 4.25$ on the edge. The density profile is determined by

$$L_{n0} = 0.4m, \qquad \Delta s_n = 0.35, \qquad s_0 = 0.6,$$

and the identical electron and ion temperature variations by

$$L_{T0} = 0.2m, \qquad \Delta s_T = 0.2, \qquad s_0 = 0.6.$$

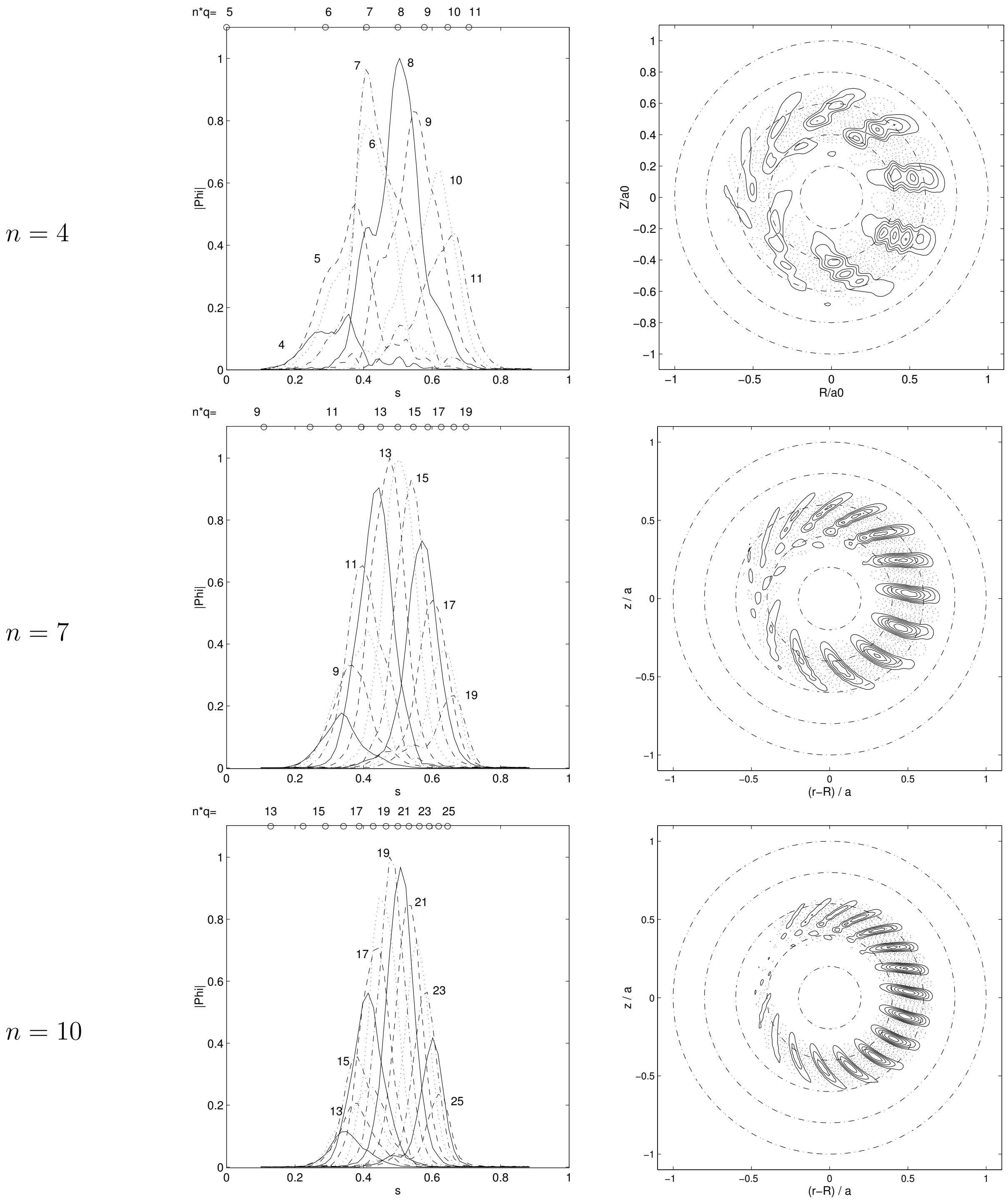

Figure 4.8: Comparing poloidal mode decomposition and structure in poloidal plane for increasing toroidal mode number $n = 4, 7, 10$ in full torus configuration.

In fact two values of temperature at s_0 are considered:

$$\left\{ \begin{array}{lll} \text{high temperature} & : & T_{e0} = T_{i0} = 7.5keV \\ \text{low temperature} & : & T_{e0} = T_{i0} = 1.875keV \end{array} \right. \text{ so that} \left\{ \begin{array}{l} a/\lambda_{L\,i} = 56.5 \\ a/\lambda_{L\,i} = 113.0 \end{array} \right. \text{at } s = s_0.$$

For instance the high temperature scenario with $n = 6$ and the low temperature case with $n = 12$ both lead to $k_\theta \lambda_{L\,i} = n q_s \lambda_{L\,i}/as = 0.35$ at s_0 and thus represent two isodynamical states in the frame of the local ballooning approximation. Real frequency and growth rate, normalized with respect to $\omega_{ne}/k_\theta \lambda_{L\,i} = \tau v_{th\,i}/L_n$ evaluated at s_0, are plotted in Fig.4.9, circles and stars corresponding respectively to the high and low temperature. This notation holds for all the following graphs. Again the growth rate peaks around $k_\theta \lambda_{L\,i} \simeq 0.5$. One must point out here that the abscissa stands for $k_\theta \lambda_{L\,i} = n q_s \lambda_{L\,i}/as$ at $s = s_0$ which may slightly differ from its average value. Ballooning results are reproduced with a dashed line. The solution to the local kinetic dispersion relation (2.33) with $\tau = 1$, $\epsilon_n = 0.2$, $\eta_i = 2.0$, $\tilde{k}_\parallel = k_\parallel L_n \simeq \epsilon_n / q_s(s_0) = 0.1$, $\tilde{k}_\perp = k_\perp \lambda_{L\,i} \simeq \tilde{k}_\theta$ is represented with a dotted line. This shows how useful this simple calculation can be, although it contains no magnetic shear effects, for estimating the position in the complex frequency plane of the global mode spectrum. As expected the global results and the ballooning solution agree for sufficiently high values of the toroidal mode number ($n \geq 10$), i.e. $k_\theta \lambda_{L\,i} \simeq 0.6$ (respectively $k_\theta \lambda_{L\,i} \simeq 0.3$) at high (respectively low) temperature, which corresponds to $n q_s' \Delta s_T a \geq 10$ mode rational surfaces inside the region of temperature variation. Near the transition to the slab-ITG at $k_\theta \lambda_{L\,i} = 0.15$, in good agreement with estimate (2.36), the global and ballooning results are qualitatively different especially concerning the growth rate, showing clearly that the latter approach is inadequate in this regime. Fig.4.10 illustrates the effect of this transition on the average value of $k_\perp \lambda_{L\,i}$. For $k_\theta \lambda_{L\,i} < 0.15$ there is an abrupt increase of the perpendicular wave number towards the typical slab-ITG value $k_\perp \lambda_{L\,i} \simeq 1$. For $k_\theta \lambda_{L\,i} > 0.15$ the dependence is approximatively linear and applying the ballooning relation $\tilde{k}_\perp = \tilde{k}_\theta \sqrt{1 + (\hat{s}\,\theta)^2}$ one obtains a slowly decreasing average poloidal angle width of the order $\theta \simeq \pi/4$. The mixing length estimate for the diffusion coefficient

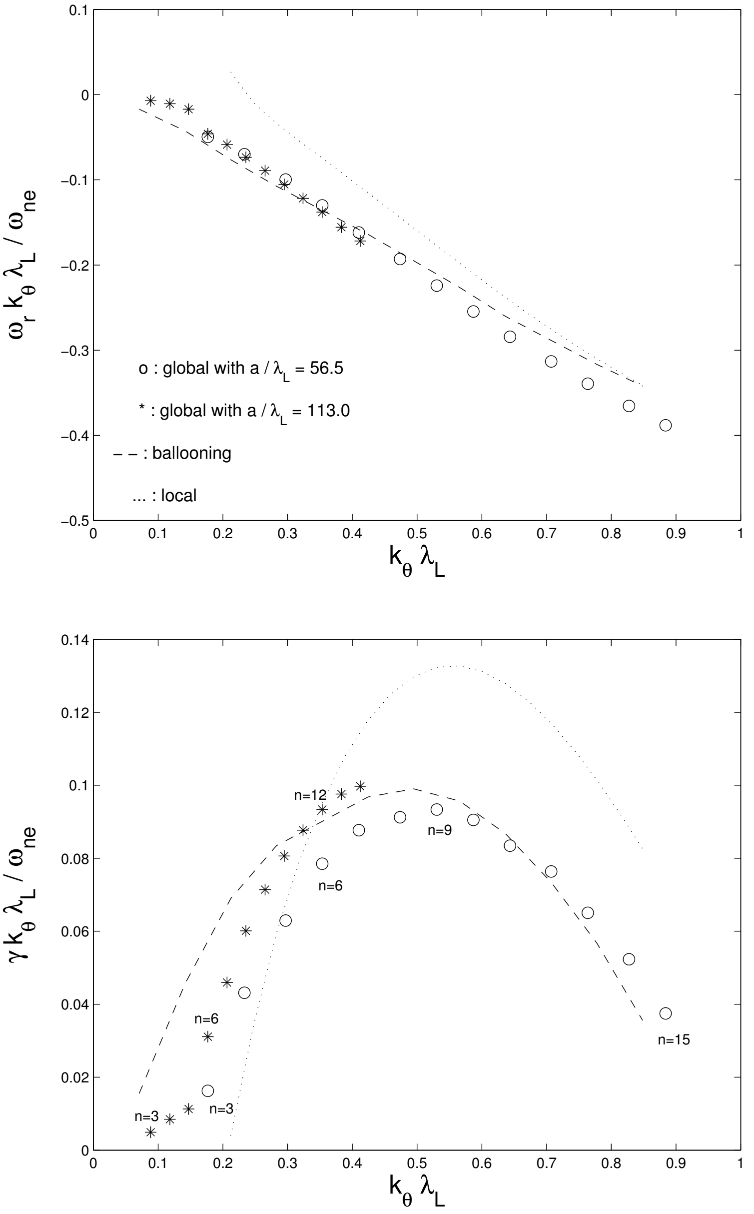

Figure 4.9: Real frequencies ω_r and growth rate γ as a function of $k_\theta \lambda_{Li}$. Circles and stars represent global results for $a/\lambda_{Li} = 56.5$ and $a/\lambda_{Li} = 113.0$ respectively. Labels below the circles and above the stars indicate the corresponding toroidal wave number. For comparison ballooning results are plotted with dashed lines and the solution to the local dispersion relation with dotted lines.

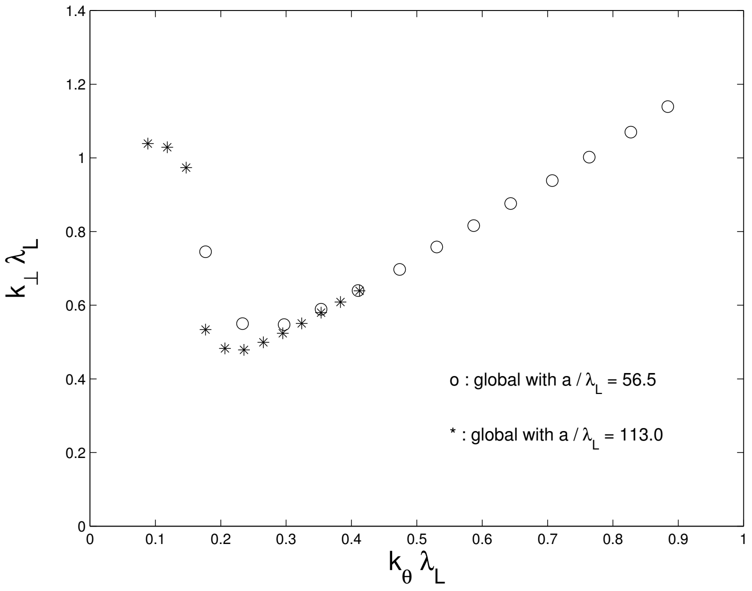

Figure 4.10: Average value of $k_\perp \lambda_{L\,i}$ as a function of $k_\theta \lambda_{L\,i}$ for $a/\lambda_{L\,i} = 56.5$ (circles) and $a/\lambda_{L\,i} = 113.0$ (stars).

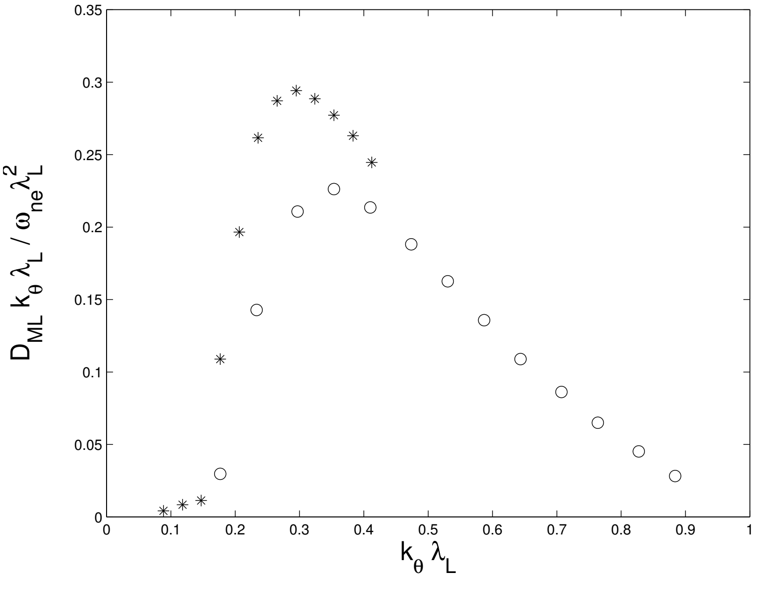

Figure 4.11: The same as previous figure but plotting mixing length estimate D_{ML} of diffusion coefficient normalized with respect to $\omega_{ne}\lambda_{L\,i}^2/k_\theta\lambda_{L\,i}$.

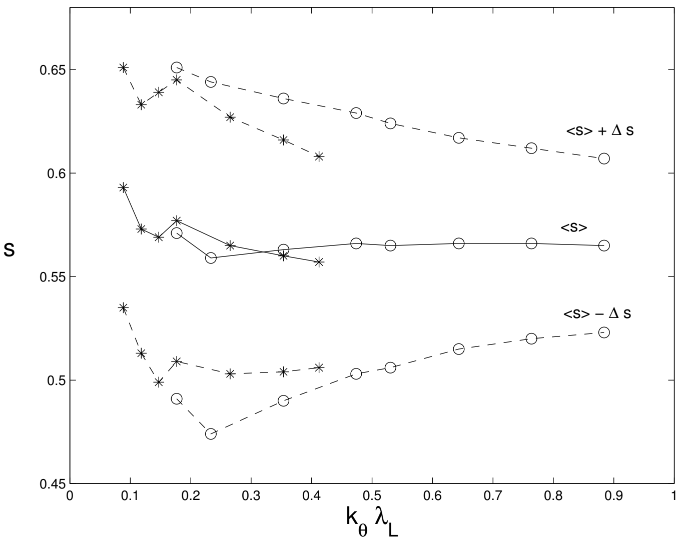

Figure 4.12: Average position $< s >$ (full line) and the limits of the double root mean squared width $2\Delta s$ (dashed line) as a function of $k_\theta \lambda_{L\,i}$. Results for $a/\lambda_{L\,i} = 56.5$ are labeled with circles, and those for $a/\lambda_{L\,i} = 113.0$ with stars.

$D_{ML} = \gamma/k_\perp^2$ [64], normalized with respect to $\omega_{ne}\lambda_{L\,i}^2/k_\theta\lambda_{L\,i} = \tau v_{th\,i}\lambda_{L\,i}^2/L_n$ evaluated at s_0, is given in Fig.4.11 and peaks for both temperatures at $\overset{\sim}{k_\theta} \simeq 0.3$, i.e. for definitely longer wavelengths then the most unstable mode. In this regime the ballooning approximation is still valid for the low temperature scenario, however it has broken down for the high temperature case yielding a difference of 25%. This gives an idea of the error which can be made using ballooning results beyond their applicability. Fig.4.12 represents in full line the average radial position and with dashed lines the double root mean squared width of the global modes as a function of $k_\theta \lambda_{L\,i}$. Note how the toroidal-ITG modes are centered at $s \simeq 0.57$, which is somewhat off the intended position $s = s_0 = 0.6$. This may in part explain the small differences still remaining with the ballooning approach even for high toroidal wave numbers. Again the toroidal-ITG becomes narrower with decreasing wavelength.

Some eigenmode structures are presented in Fig.4.13. The modes $n = 6$ (frame b.) and $n = 3$ (frame d.) as well as $n = 12$ (frame c.) and $n = 6$ (frame e.) for the cases $a/\lambda_{L\,i} = 113.0$ and $a/\lambda_{L\,i} = 56.5$ respectively, which would be iso-dynamical in

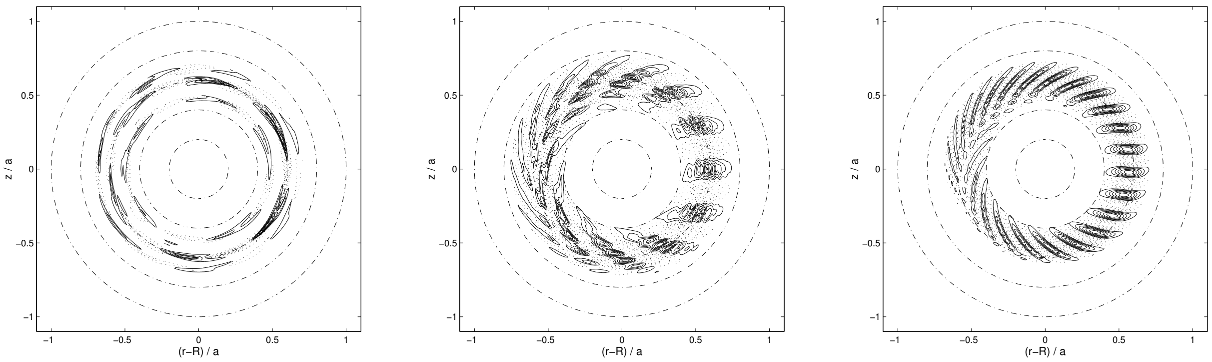

a.) $a/\lambda_{L\,i} = 113.0$, $n = 3$. b.) $a/\lambda_{L\,i} = 113.0$, $n = 6$. c.) $a/\lambda_{L\,i} = 113.0$, $n = 12$.

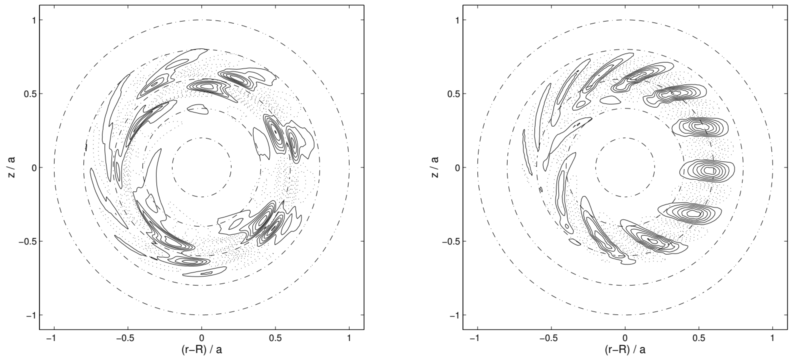

d.) $a/\lambda_{L\,i} = 56.5$, $n = 3$. e.) $a/\lambda_{L\,i} = 56.5$, $n = 6$.

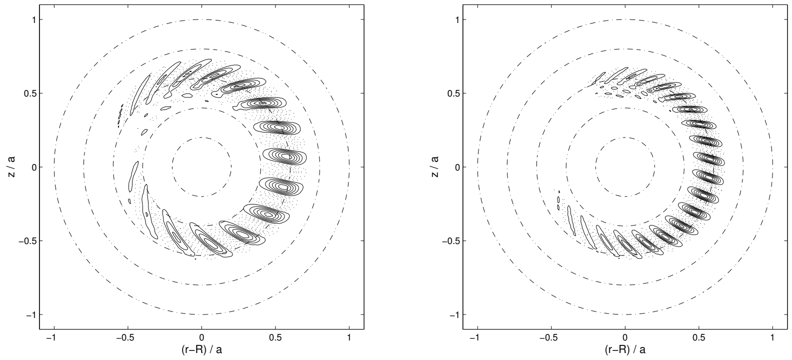

f.) $a/\lambda_{L\,i} = 56.5$, $n = 9$. g.) $a/\lambda_{L\,i} = 56.5$, $n = 15$.

Figure 4.13: Eigenmode structures in poloidal plane for $n = 3, 6, 12$ in the case $a/\lambda_{L\,i} = 113.0$ and $n = 3, 6, 9, 15$ in the case $a/\lambda_{L\,i} = 56.5$. Modes b.) and d.) as well as c.) and e.) are iso-dynamical with respect to the local ballooning approximation.

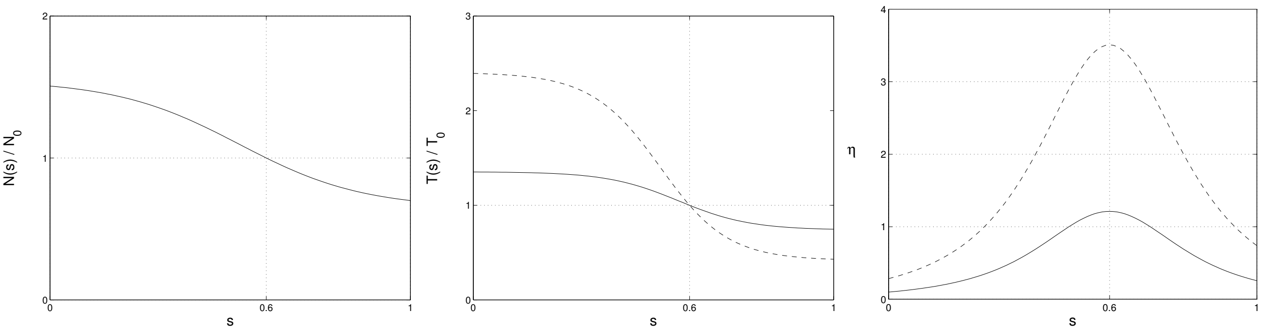

Fixed density profile as a function of $s = \rho/a$.

Temperature profiles. Full line (resp. dashed) corresponds to $\eta = 1.2$ (resp. $\eta = 3.5$) at $s_0 = 0.6$.

Corresponding η profiles.

Figure 4.14: Profiles for η_i scan.

ballooning approximation, are arranged one above the other. Notice that their envelopes indeed exhibit similarities. The mode $n = 3$ at low temperature illustrates a typical slab-ITG instability with fluctuations localized on the mode rational surfaces relative to $m = nq_s(s_r) = 5, 6, 7$. The high temperature modes $n = 6$ (frame e.) and $n = 9$ (frame f.) correspond respectively to the highest mixing length estimate and growth rate for that scenario. For the same temperature mode $n = 15$ (frame g.) shows explicitly the pronounced ballooning and narrowing of the radial extent at high toroidal wave numbers.

4.4.7 η_i Scan

Carrying on with the high temperature scenario of the DIII-D type configuration defined in the previous section, the toroidal wave number is now fixed to $n = 9$ so that $k_\theta \lambda_{L\,i} = 0.53$ at s_0. The characteristic lengths $L_{T_i 0} = L_{T_e 0}$ of ion and electron temperatures are however varied so as to find the critical value of $\eta_i = L_{n0}/L_{T_i 0}$ relative to marginal stability. The previous study showed that $n = 9$ is near the limit of applicability of the ballooning approximation for $\eta_i = 2$. The temperature dependence for different gradients at $s = s_0$ and the corresponding η profiles are plotted in Fig.4.14 as well as the fixed density profile. η_i is always peaked at s_0 so that when approaching marginal state, this point remains the last to be unstable. The global results for the real frequency ω_r and growth rate γ, normalized this time with respect to $\omega_{ne} = \tau v_{th\,i} k_\theta \lambda_{L\,i}/L_n$ at s_0, are presented in Fig.4.15 with full lines. The local ballooning results from Fig.1 of reference [24] are reproduced with dashed lines. There is perfect agreement between the global and ballooning results at the critical gradient and for this configuration give $\eta_{ic} = 1.17$, showing that a global mode appears as soon as the plasma is unstable locally on a magnetic surface. The solution to the local dispersion relation (2.33) for $\tau = 1$, $\epsilon_n = 0.2$, $\tilde{k}_\perp \simeq \tilde{k}_\theta = 0.53$ and $\tilde{k}_\parallel = k_\parallel L_n \simeq \epsilon_n / q_s(s_0) = 0.1$ is plotted with dotted lines and provides a weaker stability threshold $\eta_{ic} = 0.82$. For increasing growth rates the global and ballooning approaches diverge slightly by approximately 10%, which can again in part be explained by the fact that the average position of the global modes drifts off the intended value $s = s_0 = 0.6$ as the radial unstable region broadens, so that for $\eta_i = 3.5$ the eigenmode is centered at $s = 0.53$. This appears explicitly on the mode structures relative to $\eta_i = 1.2$ and $\eta_i = 3.5$ given in Fig.4.16 and $\eta_i = 2.$ appearing as case f.) in Fig.4.13. At the limit of stability the envelope of the mode becomes less ballooned and corrugation appears. As an effect the average radial component k_ρ of the wave vector increases to the point that $k_\perp \lambda_{L\,i} > 1$ as shown in Fig.4.17. Thus full FLR effects are necessary to resolve such a marginal state correctly. Notice also how the average poloidal component $k_\theta \lambda_{L\,i}$ departs from its intended value $k_\theta \lambda_{L\,i} = 0.53$ with increasing η_i so as to reach $k_\theta \lambda_{L\,i} = 0.6$ at $\eta_i = 3.5$. Finally Fig.4.18 plots $|z| = |\omega / k_\parallel v_{th\,i}|$ as a function of η_i, where $|k_\parallel| v_{th\,i}$ is averaged over the mode. Near η_{ic} one has $|z| \sim 1$, illustrating the necessity of a kinetic model in this regime.

4.4.8 Magnetic Shear Scan

This scan is carried out taking again a DIII-D type plasma (4.15). The local parameters are however fixed this time at $s_0 = 0.4$ which enables realistic safety factor profiles to give rise to many different values of shear at this point. The safety factor itself is held at

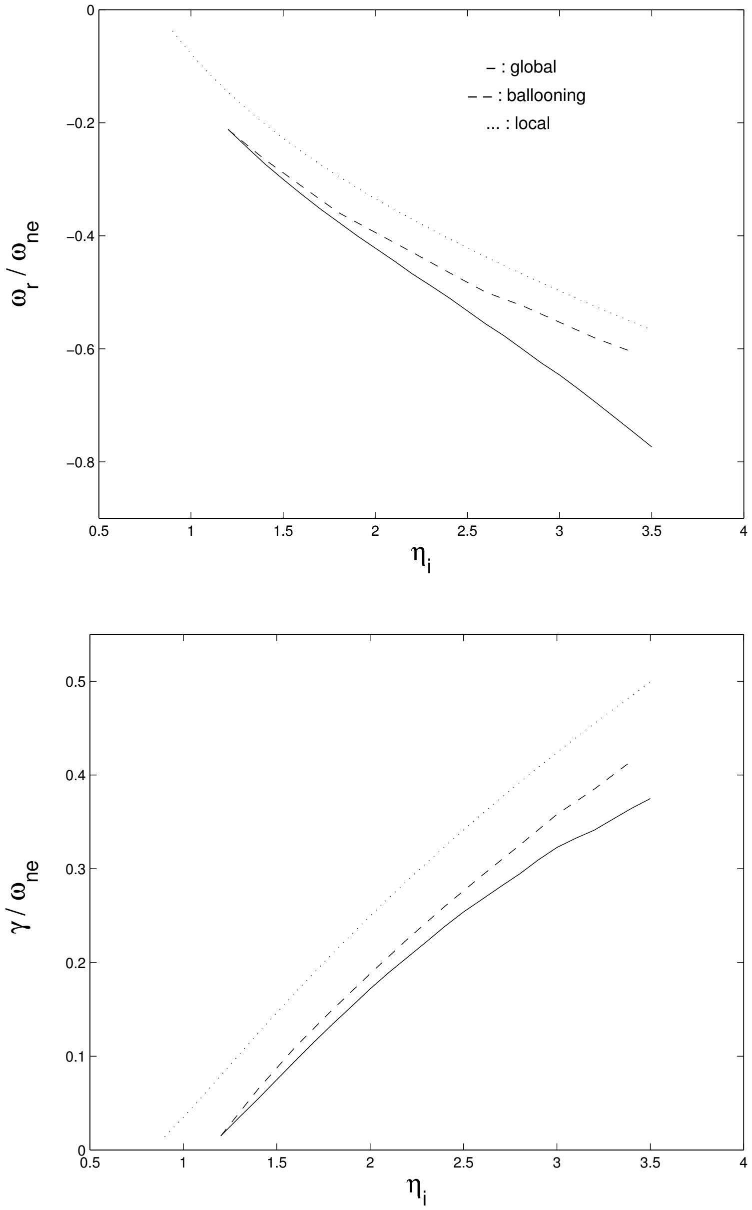

Figure 4.15: Real frequencies ω_r and growth rates γ as a function of η_i. Global results are plotted with full line, ballooning results with dashed line and solution to the local dispersion relation with dotted line.

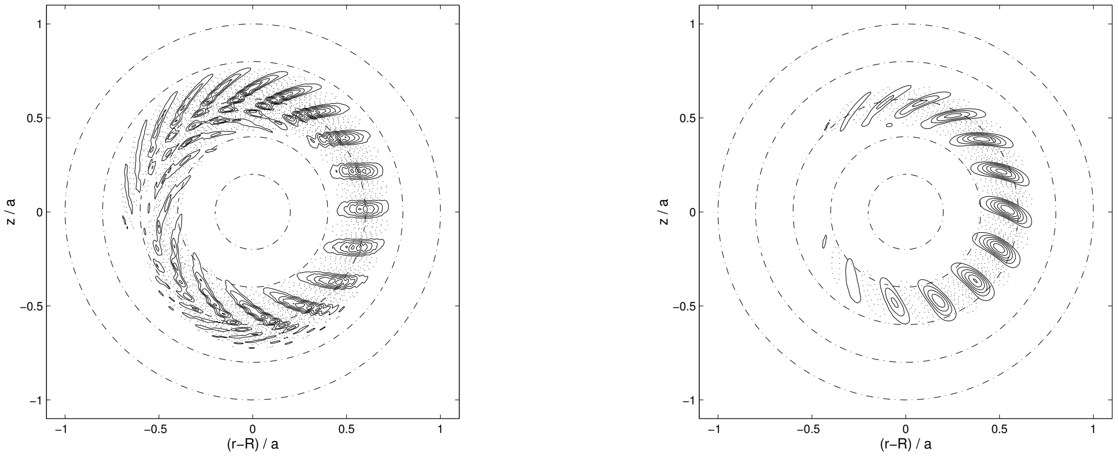

$\eta_i = 1.2$ $\eta_i = 3.5$

Figure 4.16: Evolution of mode structure along the η_i scan. Nearing the critical value $\eta_i = \eta_{ic} = 1.17$ the mode becomes less ballooned and radial corrugation appears.

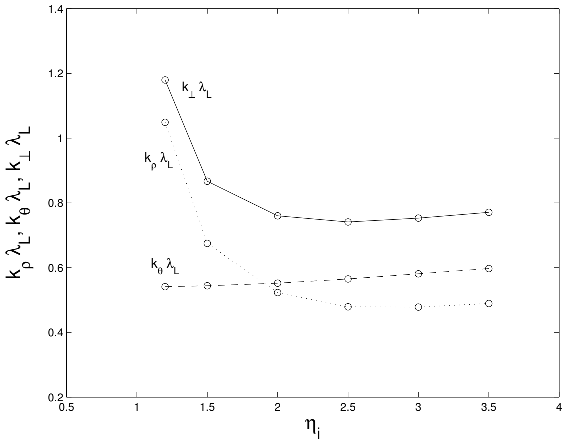

Figure 4.17: Average value of $k_\perp \lambda_{L\,i}$ (full line) as a function of η_i. Also plotted are the average components $k_\rho \lambda_{L\,i}$ (dotted line) and $k_\theta \lambda_{L\,i}$ (dashed line).

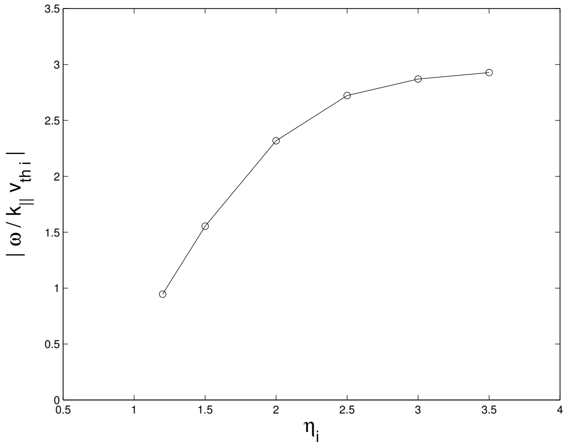

Figure 4.18: Average value of $|z| = |\omega/k_{\|} v_{th\,i}|$ as a function of η_i.

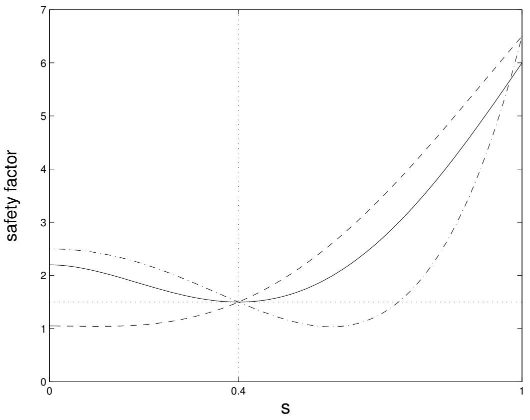

Figure 4.19: Safety factor profiles with fixed value $q_s = 1.5$ and shear $\hat{s}= +1$ (dashed line), $\hat{s}= 0$ (full line), $\hat{s}= -1$ (dash-dotted line) at $s_0 = 0.4$.

$q_s(s_0) = 1.5$. Positive shear cases up to $\hat{s}\,(s_0) = +1$ are obtained by convex combinations $q_s = xq_s^{\#1} + (1-x)q_s^{\#2}$, $0 < x < 1$ of profiles:

$$\begin{array}{lllll} q_s^{\#1} : & \hat{s}\,(s_0) = +1., & q_s(s_0) = 1.5, & q_s(0) = 1.05, & q_s(1) = 6.5, \\ q_s^{\#2} : & \hat{s}\,(s_0) = 0, & q_s(s_0) = 1.5, & q_s(0) = 2.2, & q_s(1) = 6.0. \end{array}$$

Negative shear configurations down to $\hat{s}= -1$ are modeled by convex combinations of $q_s^{\#2}$ and $q_s^{\#3}$:

$$q_s^{\#3} \;:\; \hat{s}\,(s_0) = -1., \quad q_s(s_0) = 1.5, \quad q_s(0) = 2.5, \quad q_s(1) = 6.5.$$

These three profiles are plotted in Fig.4.19 with respectively dashed, full and dash-dotted lines. Density as well as equal electron and ion temperature dependences are given by

$$\begin{array}{llll} L_{n0} = 0.5m, & \Delta s_n = 0.35, & s_0 = 0.4, & \\ L_{T0} = 0.2m, & \Delta s_T = 0.2, & s_0 = 0.4, & T_{e0} = T_{i0} = 2.13keV, \end{array}$$

so that again η_i peaks at s_0. Furthermore, fixing the toroidal wave number to $n = 10$, the different local ballooning parameters take the values

$$q_s = 1.5, \quad \tau = 1, \quad \epsilon_n = 0.25, \quad \eta_i = 2.5, \quad \overset{\sim}{k_\theta}= 0.35,$$

which are the same as for the shear scan in Fig.7 of reference [41].

Real frequency and growth rate, normalized with respect to ω_{ne} evaluated at $s = s_0$, of the different unstable eigenmodes computed with the global code are represented in

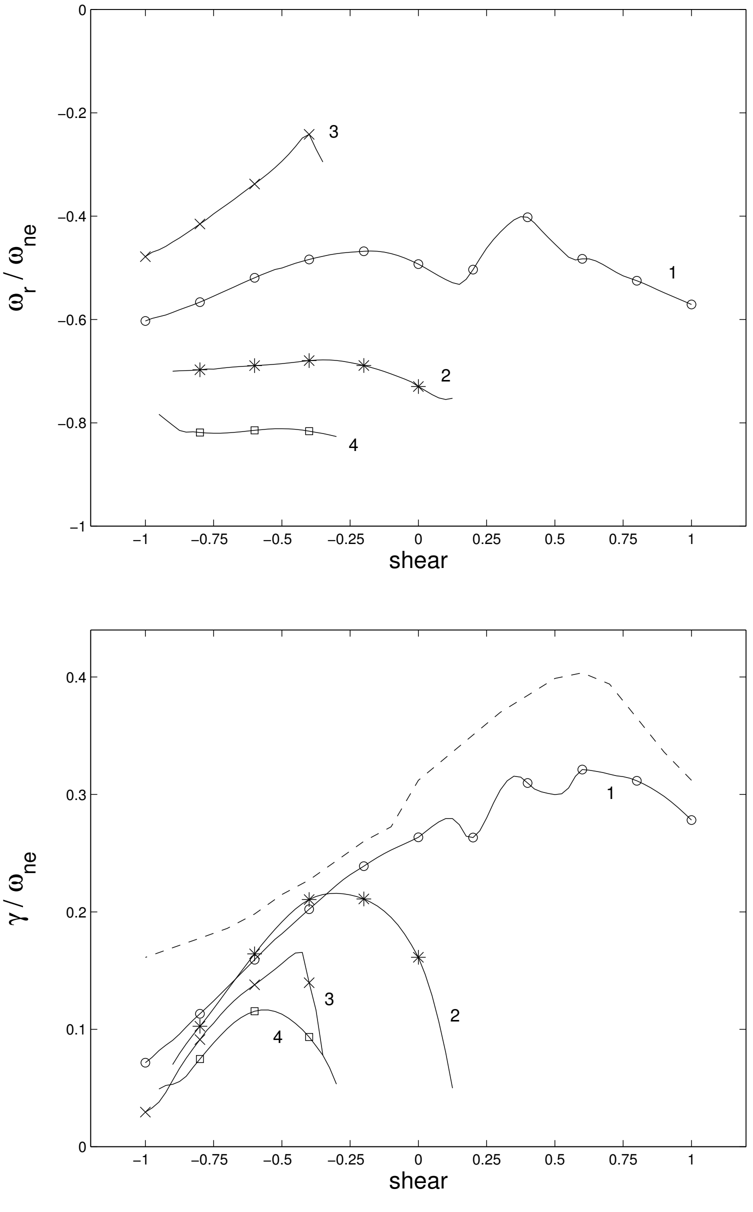

Figure 4.20: Real frequencies ω_r and growth rates γ as a function of shear $\hat{s}$. With decreasing shear the toroidal mode (1) becomes slab-like and new instabilities (2), (3), (4) appear. Growth rate of the local ballooning approximation results are reproduced with a dashed line.

Fig.4.20 with full lines. The growth rate from the local ballooning approximation is drawn with a dashed line. The evolution of this spectrum can be mainly explained through relation (2.42), which shows in the frame of ballooning representation how shear affects the GC drift frequency:

$$\omega_g = \omega_{g\theta} + \omega_{g\rho} = -k_\theta v_{dz}(\cos\theta + \hat{s}\,\theta\sin\theta).$$

Thus for a mode which is not too localized around $\theta = 0$, decreasing shear partly suppresses this toroidal drive. In this respect a shear scan is similar to the toroidicity scan presented in section 4.4.5. Hence, for $\hat{s} < 0.5$ the growth rate of the unstable eigenmode decreases when lowering shear to the point where at $\hat{s} = -0.5$ the average value of ω_{gi} is insufficient to sustain the toroidal-ITG instability and the transition to a slab-like regime is induced. Typical for such a state, a whole set of new unstable eigenmodes appear with growth rates of the same order. Mode 2 actually takes over mode 1 for the interval $-0.7 \lesssim \hat{s} \lesssim -0.3$. The roll over of γ at $\hat{s} = 0.5$ results in part from toroidal drive which has become too strong, as in Fig.4.1 for configurations with too low aspect ratio. This is confirmed by Fig.4.21 which shows how the average radial contribution $\omega_{gi\,\rho}$, varying linearly, cancels the total GC drift frequency ω_{gi} while the poloidal contribution $\omega_{gi\,\theta}$ remains approximately constant. However, as plotted in Fig.4.22, $\hat{s} = 0.5$ also corresponds to the point where $\tilde{k}_\perp \simeq 0.5$ is reached, that is the typical value at which the growth rate of the toroidal-ITG maximizes. This is an additional effect of shear as $k_\perp = \sqrt{k_\theta^2 + k_\rho^2}$ with the variation of the radial component being given in the toroidal-ITG regime by the ballooning relation $k_\rho = k_\theta\,\hat{s}\,\theta$. In the slab-ITG regime, i.e. for $\hat{s} \lesssim -0.5$, the perpendicular wave number blows up to the typical value $k_\perp \lambda_{L\,i} \simeq 1$.

As the safety factor profile varies from $q_s^{\#1}$ to $q_s^{\#2}$ its minimum value simultaneously increases while moving from the magnetic axis towards $s_0 = 0.4$. Consequently mode rational surfaces disappear inside the unstable region, which leads to a periodic rearrangement of the instability over the remaining resonant surfaces, avoiding the gap left

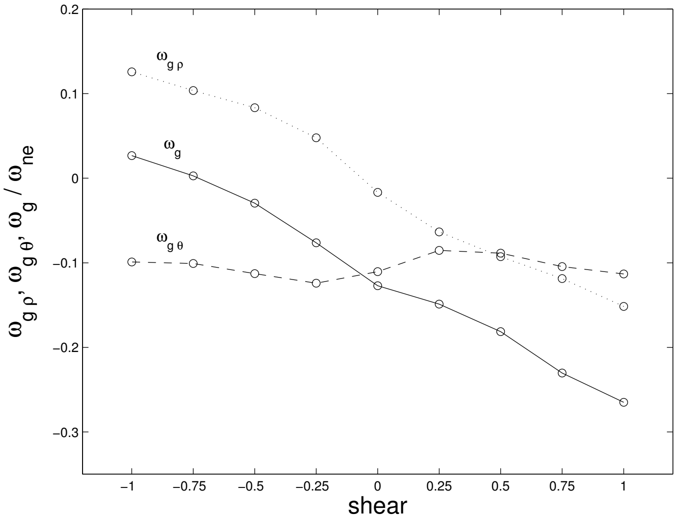

Figure 4.21: Average GC drift frequency ω_g (full line) split into the radial contribution $\omega_{g\rho}$ (dotted line) and the poloidal contribution $\omega_{g\theta}$ (dashed line). With decreasing shear $\omega_{g\rho}$ finally inverts the sign of ω_g which stabilizes the toroidal-ITG instability.

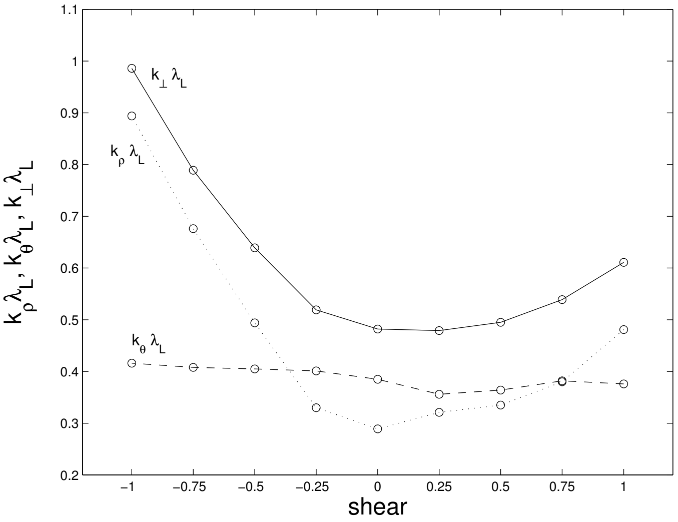

Figure 4.22: Average value of $k_\perp \lambda_{L\,i}$ (full line) as a function of shear. Also plotted are the average values of $k_\rho \lambda_{L\,i}$ (dotted line) and $k_\theta \lambda_{L\,i}$ (dashed line).

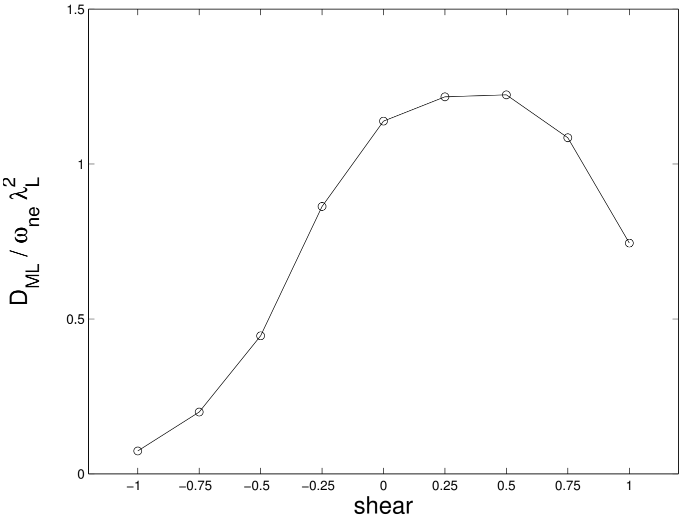

Figure 4.23: Mixing length estimate D_{ML} of diffusion coefficient normalized with respect to $\omega_{ne}\lambda_{L\,i}^2$ as a function of shear.

around the shear-less point. This mechanism explains the bumpy behavior of the growth rate for $0 \overset{\sim}{<} \hat{s} \overset{\sim}{<} 0.75$ and the discrepancy with the ballooning result which does not contain such a non-local effect.

The attenuation of γ by a factor ~ 4.5 between $\hat{s}= 0.5$ and $\hat{s}= -1.0$ observed for the global results is significantly more important then the factor ~ 2.5 over the same interval from the ballooning results. This is not astonishing as the local ballooning approximation is inappropriate for describing the slab-ITG regime at negative shear and tends to overestimate the instability. The effect of reversed shear is emphasized in Fig.4.23 giving the mixing length estimate of the diffusion coefficient. Fig.4.24 illustrates the evolution of the structure of the most unstable eigenmode when varying shear from $\hat{s}= +1.$ to $\hat{s}= -1.$ at $s = s_0 = 0.4$. Notice how the radial structures start to twist in the opposite direction as the reversed shear enters the unstable region. At $\hat{s}= -1., -0.5$ the structure has essentially lost its ballooning envelope and its radial extent is much diminished indicating a slab-like character.

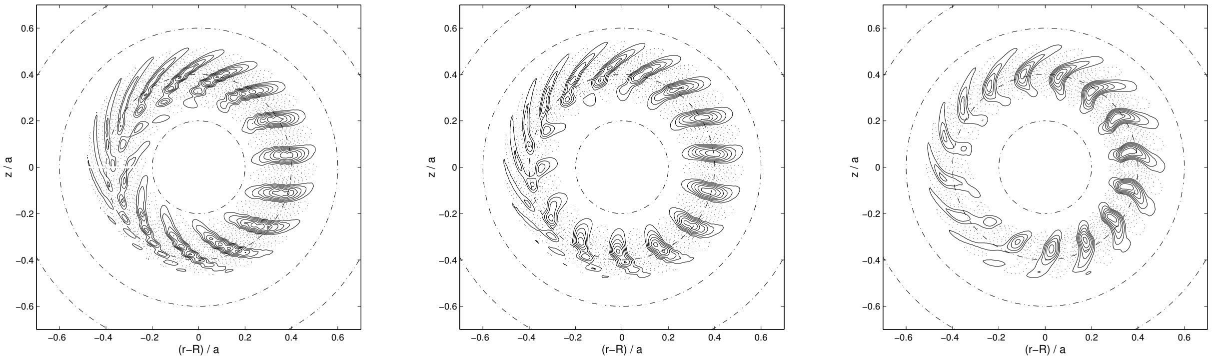

a.) $\hat{s}= +1$. b.) $\hat{s}= +0.5$. c.) $\hat{s}= 0$.

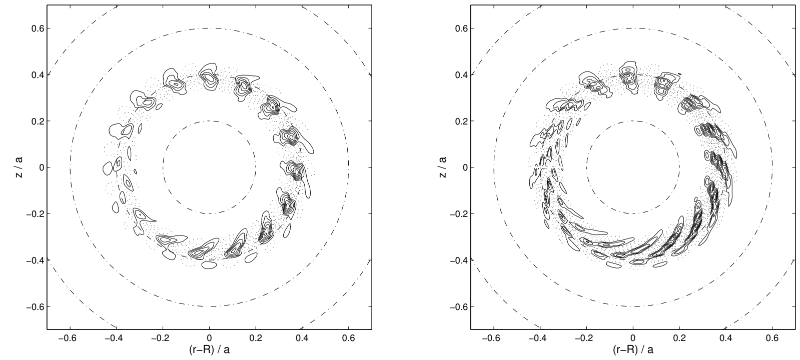

d.) $\hat{s}= -0.5$. e.) $\hat{s}= -1$.

Figure 4.24: Mode structure of most unstable mode along shear scan $\hat{s}= +1.\dots -1$.

Chapter 5

Adding Trapped Electrons

Trapped electron dynamics is modeled with a bounce-averaged kinetic equation and implemented in the global toroidal code. This improved model allows us to study how these particles affect the ITG-type instabilities including the possible transition to the trapped electron mode.

5.1 Bounce-Averaged Model for Trapped Electrons

In this section the non-adiabatic contribution of trapped electrons to the eigenvalue equation cast in Fourier representation (4.7) is calculated. From the solution (C.8) to the bounce-averaged DKE derived in appendix C, one can evaluate the non-adiabatic contribution to the density fluctuation of trapped electrons:

$$\tilde{n}_e^{n.a.} = -\frac{e}{T_e} \int_{trap} d^3v F_{Me} \frac{\omega - \omega_e^\star}{\omega - n <\dot{\varphi}>_e} < \phi >_b, \tag{5.1}$$

where the integration over velocity space is limited to trapped particles. For the circular, large aspect ratio torus considered here, the bounce averaged potential is given by

$$\begin{aligned} < \phi >_b &= \bar{\phi}\, e^{in(\varphi + q_s\theta)}, \\ \bar{\phi}\,(\rho, \lambda) &= \frac{\sqrt{2\lambda A^{-1}}}{4\boldsymbol{K}(X)} \int_{\theta_1}^{\theta_2} d\theta \frac{1}{\sqrt{1 - \lambda(1 - A^{-1}\cos\theta)}} \phi(\rho, \theta) e^{-inq_s\theta}, \end{aligned}$$

having used the definition $\theta_2 = -\theta_1 = 2 \arcsin\sqrt{X}$ for the turning point angles, $X = (1 - \lambda B_{min}/B_0)/2\lambda A^{-1}$ and relation (C.6) for the bounce period. Inserting the toroidal wave decomposition (4.2) leads to the definition of the coefficients C_m:

$$\bar{\phi} = \frac{1}{2\boldsymbol{K}(X)} \sum_{(k,m)} \phi_{(k,m)} e^{i\kappa\rho} C_m,$$
$$C_m(\rho, X) = \int_0^{\theta_2} d\theta \frac{\cos(m - nq_s)\theta}{\sqrt{X - \sin^2(\theta/2)}}.$$

Note that Eq.(5.1) is local to a magnetic surface as finite banana width effects have been neglected for electrons. Adding this term to the left hand side of the quasineutrality equation (4.1) and projecting on the Fourier component $\exp i(\kappa\rho + m\theta + n\varphi)$ provides the contribution of trapped electrons to the matrix (4.8):

$$M^{n.a.}_{e(k,m),(k',m')} = -\frac{1}{\Delta\rho}\int_{\rho_l}^{\rho_u} d\rho e^{-i(\kappa-\kappa')\rho} \frac{1}{2\pi}\int_{-\pi}^{\pi} d\theta e^{-i(m-nq_s)\theta} \int_{trap} d^3v \frac{1}{\tau}\frac{F_{Me}}{N} \frac{\omega - \omega_e^\star}{\omega - n <\dot{\varphi}>_e} \frac{C_{m'}}{2\boldsymbol{K}(X)}.$$

Working with velocity variables $(\mathcal{E}, X)$ so that

$$\int_{trap} d^3v = 2\pi A^{-1} \frac{B}{B_0} \sum_{\sigma=\pm 1} \int_{\sin^2\theta/2}^{1} dX \frac{\lambda^2}{\sqrt{1 - \lambda B/B_0}} \int_0^\infty d\mathcal{E}\sqrt{2\mathcal{E}}, \tag{5.2}$$

and permuting the integrals with respect to θ and X:

$$\begin{aligned} M^{n.a.}_{e(k,m),(k',m')} &= -\frac{1}{\Delta\rho}\int_{\rho_l}^{\rho_u} d\rho e^{-i(\kappa-\kappa')\rho} \frac{1}{\tau} \times \\ & \frac{1}{2\pi}\int_0^1 dX \lambda\sqrt{2\lambda A^{-1}} \frac{C_m C_{m'}}{\boldsymbol{K}(X)} \frac{1}{\sqrt{2\pi}} \int_0^\infty \frac{d\mathcal{E}\sqrt{2\mathcal{E}}}{v_{th\,e}^3} e^{-\mathcal{E}/v_{th\,e}^2} \frac{\omega - \omega_e^\star}{\omega - n <\dot{\varphi}>_e}, \end{aligned}$$

having approximated $B/B_0 \simeq 1$ in the numerator of (5.2). Let us rewrite the result (C.7) obtained for the toroidal drift:

$$\begin{aligned} <\dot{\varphi}>_e &= \frac{\mathcal{E}}{v_{th\,e}^2} <\dot{\varphi}>_{e0}, \\ <\dot{\varphi}>_{e0}(\rho, X) &= -\frac{v_{th\,e}^2}{\Omega_e}\frac{1}{R}\frac{q_s}{\rho} 4\lambda \left\{ \hat{s}\left[(X-1) + \frac{\boldsymbol{E}(X)}{\boldsymbol{K}(X)}\right] + \frac{1}{2}\left[\frac{\boldsymbol{E}(X)}{\boldsymbol{K}(X)} - \frac{1}{2}\right]\right\}. \end{aligned}$$

The integrals with respect to $E = \mathcal{E}/v_{th\,e}^2$ can actually be expressed in terms of the dispersion function (2.26), being careful with causality:

$$\begin{aligned} \frac{1}{\sqrt{2\pi}}\int_0^\infty dE\sqrt{2E} \frac{e^{-E}}{E - \omega/n <\dot{\varphi}>_{e0}} &= \frac{2}{\sqrt{2\pi}}\int_0^\infty dy \frac{y^2 e^{-y^2/2}}{(y+z)(y-z)} \\ &= \frac{1}{\sqrt{2\pi}}\int_0^\infty dy \left(\frac{y}{y+z} + \frac{y}{y-z}\right) e^{-y^2/2} = W(z), \end{aligned}$$

having performed the change of variable $E = y^2/2$ and defined $z = \text{sign}(n{<}\dot{\varphi}{>}_{e0})\sqrt{2\omega/n <\dot{\varphi}>_{e0}}$. In the same way

$$\frac{1}{\sqrt{2\pi}}\int_0^\infty dE\sqrt{2E}\frac{Ee^{-E}}{E-\omega/n <\dot{\varphi}>_{e0}} = \frac{\omega}{n <\dot{\varphi}>_{e0}}W(z)+\frac{1}{2}.$$

Finally, the non-adiabatic contribution of trapped electrons reads

$$\begin{aligned} M^{n.a.}_{e(k,m),(k',m')} &= \frac{1}{\Delta\rho}\int_{\rho_l}^{\rho_u} d\rho e^{-i(\kappa-\kappa')\rho}\frac{1}{\tau}\frac{1}{2\pi}\int_0^1 dX\lambda\sqrt{2\lambda A^{-1}} \times \\ & \frac{C_m C_{m'}}{n <\dot{\varphi}>_{e0}\,\boldsymbol{K}(X)}\left\{\left[\omega-\omega_{ne}(1-\frac{3}{2}\eta_e)\right]W(z)-\omega_{ne}\eta_e\left[\frac{\omega}{n <\dot{\varphi}>_{e0}}W(z)+\frac{1}{2}\right]\right\}. \end{aligned}$$

5.2 Numerical Solution.

The computation of these matrix elements is quite straightforward.

The coefficients $C_m(\rho, X)$ are independent of frequency and can therefore be precalculated. The corresponding integration with respect to θ has an inverse square root singularity at the boundary $\theta = \theta_2$, which is removed through the change of variable $\nu = \sqrt{\theta-\theta_2}$, so that the form

$$C_m(\rho, X) = 2\int_0^{\sqrt{\theta_2}} d\nu\nu\left.\frac{\cos(m-nq_s)\theta}{\sqrt{X-\sin^2\theta/2}}\right|_{\theta=\theta_2-\nu^2},$$

is actually implemented using an extended midpoint rule [65] with 100 mesh points. In the limit of deeply trapped particles ($X = 0$) the integration domain vanishes while the integrand diverges resulting in a finite value of these coefficients:

$$\lim_{X\to 0+} C_m(\rho, X) = \lim_{X\to 0+} 2\boldsymbol{K}(X) = \pi.$$

To avoid this particular evaluation as well as the logarithmic singularity from $C_m C_{m'}/\boldsymbol{K}(X)$ for $X \to 1$ (barely trapped), the integration with respect to X is reduced to the interval $0 < X < \sin^2\theta_{max}/2$ and carried out using an extended midpoint rule with typically 50 mesh points. θ_{max} represents the maximum considered turning point angle. With

$\theta_{max} = 0.95\pi$, more then 99% of the trapped particles are taken into account. The integration over ρ is again performed with an FFT algorithm. The evaluation of the dispersion function $W(z)$ was already explained in chapter 3.

5.3 Results

In the following the first calculations performed with this extended version of the global code are commented. We shall essentially reconsider certain scans presented in the previous chapter so as to clearly illustrate the effect of non-adiabatic trapped electron dynamics.

5.3.1 η_i Scan

Except for the characteristic lengths $L_{T_i 0}$ and $L_{T_e 0}$, which will be varied independently here, all other profile parameters are held constant and are identical to the high temperature DIII-D type scenario of section 4.4.7. The toroidal wave number considered is again $n = 9$, giving a local value $k_\theta \lambda_{L\,i} = 0.53$ at the reference point $s = s_0 = 0.6$ where $\eta_i(s)$ and $\eta_e(s)$ peak. In fact the electron temperature profile will be fixed by taking $L_{T_e 0} = 0.2m$ so that $\eta_e(s_0) = 2$=const.

Frequencies and growth rates from the local kinetic dispersion relation (2.48) with parameters taking the local values at $s = s_0$, i.e. $\tau = 1.0$, $\epsilon_n = 0.2$, $\alpha_b = \sqrt{2A^{-1}} = 55\%$, $\eta_e = 2$, $G = 1.2$, $\tilde{k}_\perp = k_\perp \lambda_{L\,i} = 0.53$ and $\tilde{k}_\parallel = k_\parallel L_n \simeq \epsilon_n / q_s = 0.1$ (the value for G is taken from Fig.C.1 with $A^{-1}(s_0) = 0.15$ and $\hat{s} = 1$), are plotted in Fig.5.1 with dotted lines. As already shown in chapter 2, for $\eta_e > 2/3$ and sufficiently low ϵ_n the local dispersion relation reveals two instabilities over a certain range of η_i. This is the case here from $\eta_i \simeq 1$ up to $\eta_i \simeq 5$ (not included in Fig.5.1). Over and above this interval the solution labeled with circles, which will be designated as mode 1, propagates in the ion diamagnetic direction and corresponds essentially to the toroidal-ITG perturbed by trapped electrons. Mode 2, labeled with stars, propagates essentially in the electron diamagnetic direction. In this case, contrary to the situation presented in Fig.2.10, it is actually mode 2 which

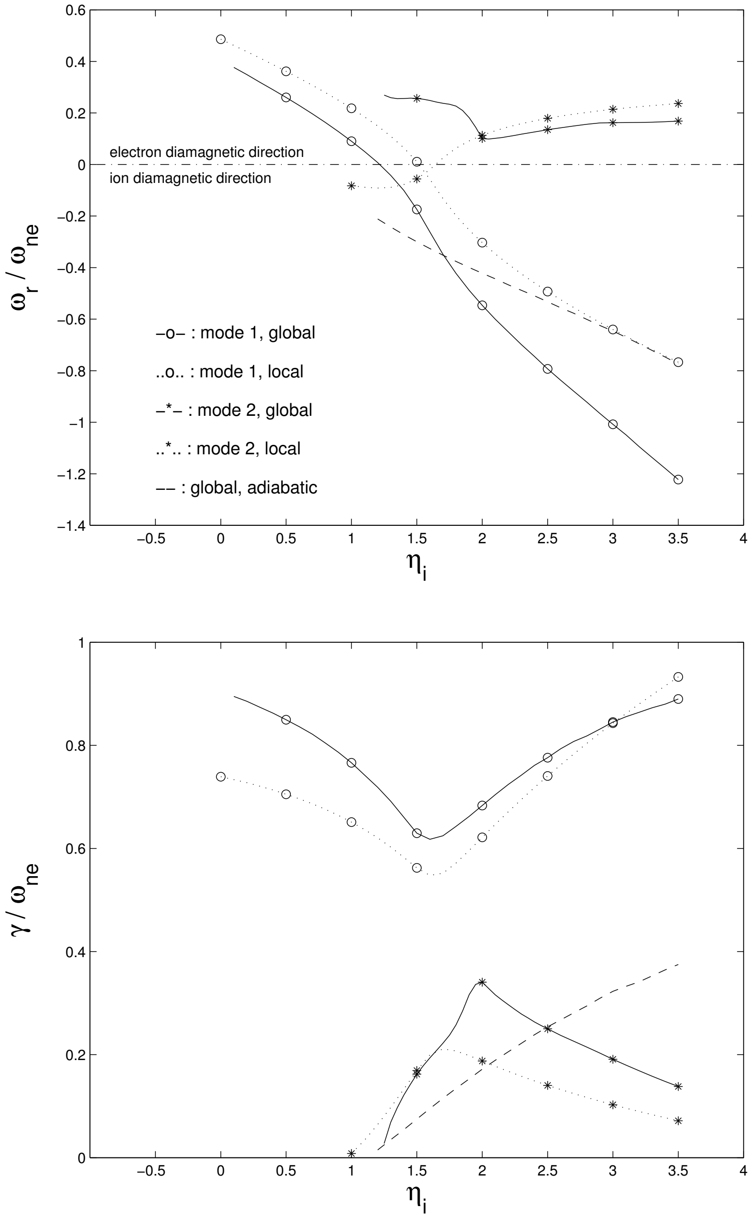

Figure 5.1: Real frequencies ω_r and growth rates γ as a function of η_i holding $\eta_e = 2$ =const. The eigenfrequencies of the most unstable eigenmodes computed with the global code are plotted with full lines and the solution to the local dispersion relation with dotted lines. The local analysis predicts a transformation of the toroidal-ITG to a predominantly TEM (mode 1), thus removing the threshold on η_i. This mechanism is confirmed by the global results as well as the presence, over a limited η_i interval, of a weaker instability propagating essentially in the electron diamagnetic direction (mode 2). For comparison the global results with only the adiabatic electron response are reproduced with dashed lines.

is stabilized for $\eta_i \stackrel{\sim}{<} 1$ while mode 1 undergoes a transition to the TEM and thus starts to propagate in the electron diamagnetic direction with increasing growth rate.

Concerning the global calculations, the highest growing eigenmode propagating in the ion diamagnetic direction as well as the most unstable one propagating in the electron diamagnetic direction were first identified at $\eta_i = 3.5$. The corresponding eigenfrequencies were then followed decreasing η_i down to 0.1 ($L_{T_i 0} = 0.11m \longrightarrow 4.0m$) and are given in Fig.5.1 with full lines and labeled using the same notations as for the local solutions. Computing the spectra at intermediate values showed that these modes remain the most unstable for each direction of propagation. Except for ω_r of mode 2, which remains positive with the global calculations down to the marginal state $\eta_i = 1.25$, frequencies and growth rates vary as predicted by the local analysis, in fact there is an astonishingly good quantitative agreement. Hence, for flat ion temperature profiles the global spectra only contains TEM-type eigenmodes propagating in the electron diamagnetic direction while it includes both positive and negative frequencies immediately above $\eta_i \simeq 1$ as the toroidal-ITG appears. As a reference the global results with only the adiabatic electron response are reproduced in Fig.5.1 with a dashed line. The growth rate of the toroidal-ITG instability at $\eta_i = 3.5$ shows an increase by a factor ~ 2 due to non-adiabatic trapped electron dynamics.

Structures in the poloidal plane of eigenmodes 1 and 2 are displayed in Fig.5.2 for $\eta_i = 0.1, 2.0, 3.5$. The envelope of mode 1 stays nearly unchanged, contrary to the toroidal-ITG computed with adiabatic electrons and shown in Fig.4.16 which lost most of its ballooning feature near marginal stability at $\eta_i = 1.2$. As mode 1 undergoes transition from the toroidal-ITG (frame c. of Fig.5.2) to the TEM (frame a.) the non-twisted 'finger' moves from the poloidal position $\theta_0 \simeq \pi/4$ to $\theta_0 \simeq -\pi/4$, at the same time the average radial position shifts slightly outward where the fraction $\alpha_b \simeq \sqrt{2A^{-1}}$ of trapped particles is larger. At $\eta_i = 2.0$ eigenmode 2 (frame e.) exhibits simultaneously these TEM and toroidal-ITG features giving rise to a radially large but less coherent structure, which is

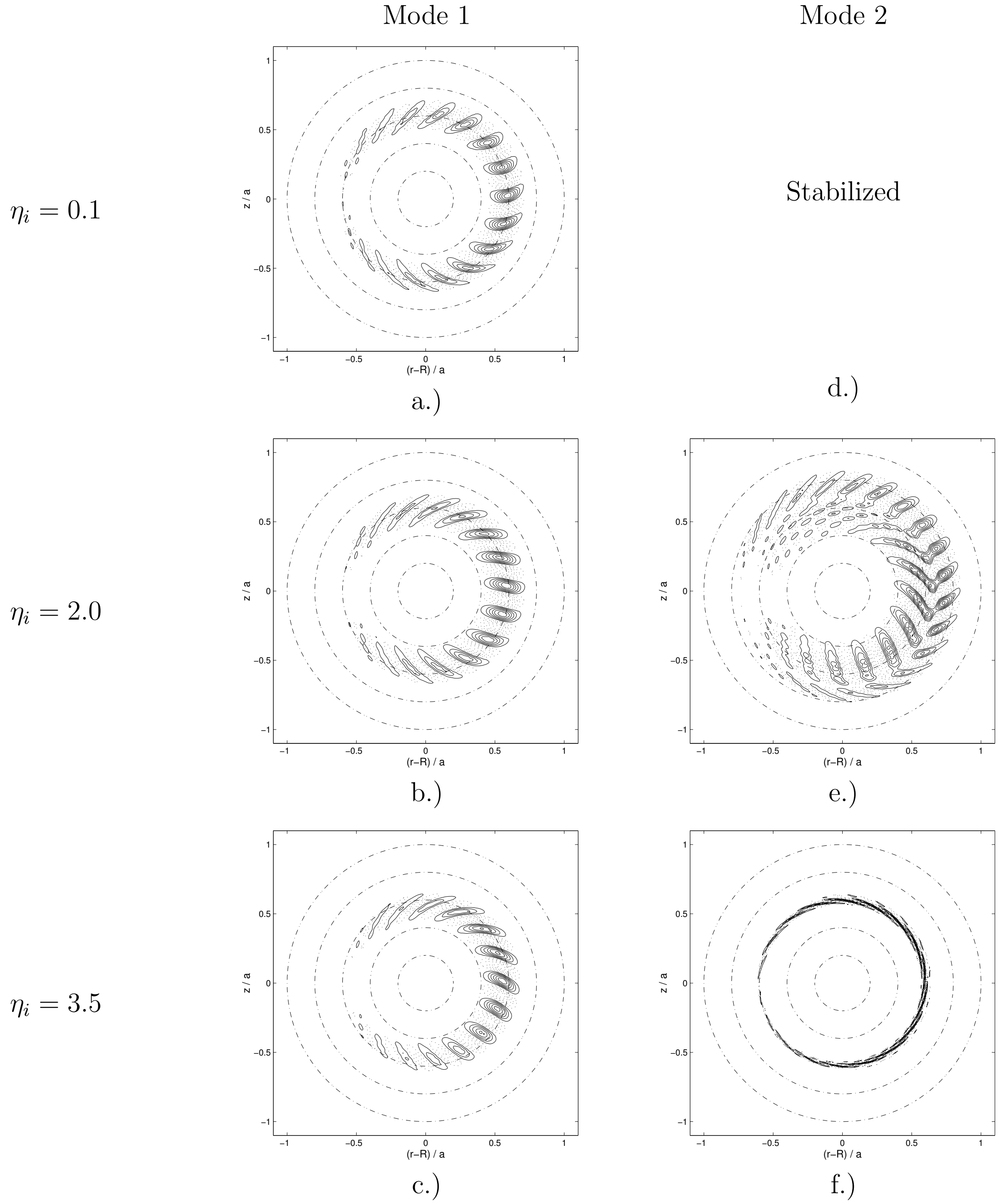

Figure 5.2: Evolution of eigenmodes 1 & 2 for varying η_i, holding $\eta_e = 2.0$ =const.

probably related to the fact that this instability remains marginal. Approaching the lower marginal state at $\eta_i = 1.25$, the average radial position of this mode has drifted to $s = 0.73$, i.e. significantly off the reference surface $s = s_0$, thus explaining the disagreement in this region on ω_r with the local results. For $\eta_i = 3.5$ (frame f.), where this mode nears the upper marginal state, a very narrow radial extent and wavelength are measured giving an average value $k_\perp \lambda_{L\,i} \sim 5$. In such a regime ion dynamics naturally becomes quite weak through FLR effects, however they still provide the only radial coupling as finite banana widths of electrons have been neglected in our model. This approximation may be questioned here.

5.3.2 Magnetic Shear Scan

Let us now study the contribution of trapped electrons when varying magnetic shear. For this purpose the equilibria is transformed exactly as in section 4.4.8 and the toroidal wave number is again fixed to $n = 10$. This leads to a local value $k_\theta \lambda_{L\,i} = 0.35$ at the reference surface $s = s_0 = 0.4$ where the $\eta_i(s) \equiv \eta_e(s)$ and $\epsilon_n(s)$ profiles reach there maximum value $\eta_i = \eta_e = 2.5$ and $\epsilon_n = 0.25$ respectively. A fraction $\alpha_b = 45\%$ of trapped particles is found at the low field side of this magnetic surface.

The spectrum at $\hat{s} = +1.0$ is represented in Fig.5.3. The high number of eigenfrequencies is in contrast with the single unstable toroidal-ITG eigenmode appearing in Fig.4.20 for the same value of shear. In particular the spectrum contains a set of very densely packed points for the modes propagating in the electron diamagnetic direction. Their identification becomes tedious as the root finding method can handle at most ten eigenvalues inside a single sampling curve. The complex frequency plane must therefore be paved with many such paths. For this reason, this part of the spectrum was only computed for $\gamma/\omega_{ne} \gtrsim 0.25$. Additional eigenmodes are also found propagating in the ion diamagnetic direction. Their growth rates are however such that the most unstable toroidal-ITG-type instability stays well isolated. For each direction of propagation, only

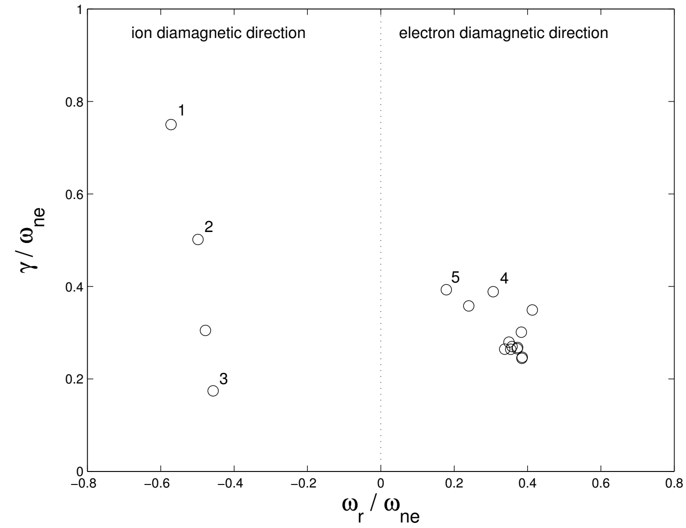

Figure 5.3: Spectrum for $\hat{s}= +1.0$. The eigenfrequencies which have been followed along the shear scan are labeled with the same numbers as in Fig.5.4. The high density of eigenfrequencies relative to modes propagating in the electron diamagnetic direction ($\omega_r > 0$) makes the identification of this part of the spectrum difficult and is therefore limited to $\gamma/\omega_{ne} \overset{\sim}{>} 0.25$.

the eigenmodes which turn out to dictate the highest growth rate during one part or the other of the scan have been followed. These are labeled in Fig.5.3 with the same numbers as in Fig.5.4 where the real and imaginary part of their eigenfrequencies are plotted for varying shear.

The TEM-type eigenmodes (essentially mode 4 & 5) are progressively damped when going to negative shear so that no positive frequency is found at $\hat{s}= -1.0$. This can naturally be explained by the decrease of the average amplitude of the toroidal precessional drift which drives these instabilities, from $G \simeq 1.2$ at $\hat{s}= +1.$ to $G \simeq 0.2$ at $\hat{s}= -1.0$ (estimates from Fig.C.1).

Throughout the scan the highest growth rate over all eigenvalues is always determined by the ITG-type instabilities (mode 1, 2 & 3). Except for the fact that more then one of these eigenmodes are already present at $\hat{s}= +1.0$, the qualitative behavior of this part of the spectrum along the scan is quite analogous to the one in Fig.4.20. Quantitative comparison shows that trapped electron dynamics increases the maximum growth rate

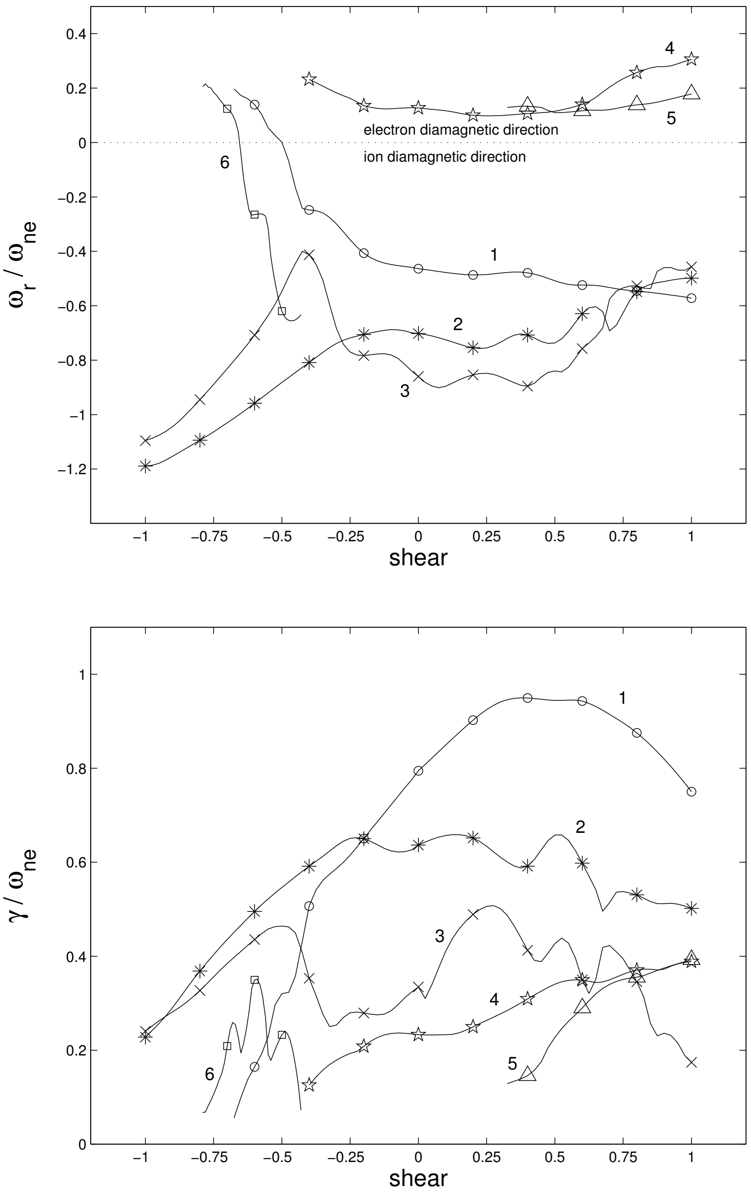

Figure 5.4: Real frequencies ω_r and growth rates γ as a function of shear $\hat{s}$. For $\hat{s}= +1.0$ the unstable spectrum contains simultaneously positive and negative frequencies. At $\hat{s}= -1.0$ only the ITG-type modes remain destabilized, however with a significantly reduced growth rate compared with the highest one around $\hat{s}= +0.5$.

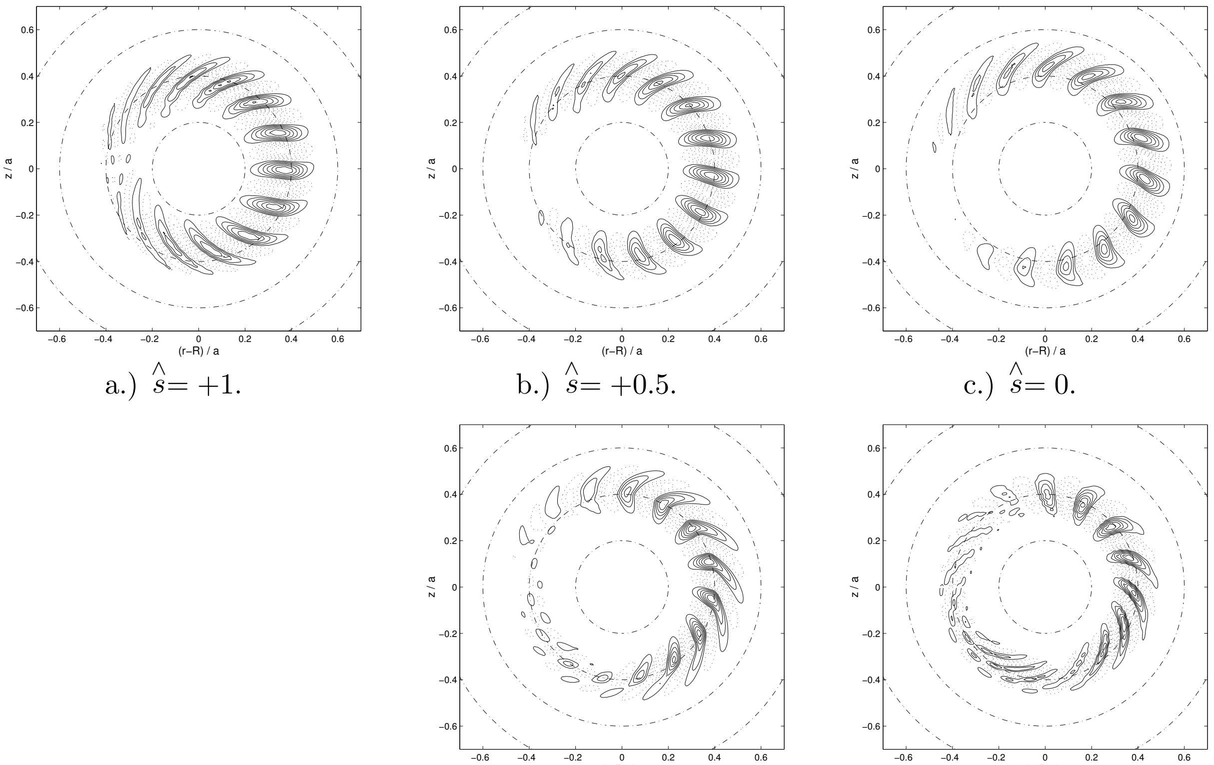

a.) $\hat{s}= +1$. b.) $\hat{s}= +0.5$. c.) $\hat{s}= 0$.

d.) $\hat{s}= -0.5$. e.) $\hat{s}= -1$.

Figure 5.5: Mode structure of most unstable mode along shear scan $\hat{s}= +1. \ldots -1$.

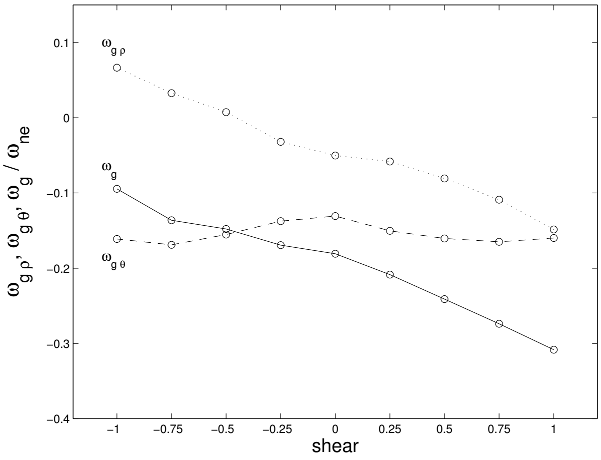

Figure 5.6: Average GC drift frequency ω_g (full line) split into the radial contribution $\omega_{g\rho}$ (dotted line) and the poloidal contribution $\omega_{g\theta}$ (dashed line). Due to the increased ballooning of the eigenmodes in the unfavorable curvature region, ω_g is less sensitive to shear then in Fig.4.21 where only the adiabatic response of electrons is considered. ω_g thus remains negative down to $\hat{s}= -1.0$, allowing a more effective ion drive.

for all values of shear. An enhancement factor of ~ 3.0 (respectively ~ 3.4) is measured at $\hat{s}= +1.0$ (respectively $\hat{s}= -1.0$) so that in relative values these particles have a slightly more destabilizing effect at negative shear. Thus the attenuation factor of γ through negative shear between $\hat{s}\simeq 0.5$ and $\hat{s}= -1.0$ is ~ 4.0 instead of ~ 4.5 with adiabatic electrons. These observations can in part be explained by the local analysis in Fig.2.13 illustrating how the toroidal ITG instability is destabilized for all positive values of the precessional drift amplitude but mostly for $G \simeq 0$, corresponding to negative shear cases.

An additional, non-local effect of trapped electrons is the increased ballooning of the eigenmode in the unfavorable curvature region where these particles are localized, clearly visible by comparing the mode structures in Fig.5.5 with those in Fig.4.24. This leads to an average GC drift frequency ω_g (plotted in Fig.5.6) which is less sensitive to shear then in the absence of trapped electrons (see Fig.4.21) and thus remains negative even for $\hat{s}= -1.0$. In this way non-adiabatic electrons enhance the ion drive so that the eigenmodes never undergo a full transition to the more stable slab-like ITG instability. This is illustrated by comparing frames d.) and e.) of Fig.5.5 to those in Fig.4.24.

5.3.3 Toroidal Wave Number Scan

In a last study we have recomputed the n scan for the high temperature DIII-D type equilibrium with identical parameters as in section 4.4.6. Let us recall that these are the same conditions as for the η_i scan of section 4.4.7 and 5.3.1 except that the temperature profiles are fixed so that $\eta_i = \eta_e = 2.0$ at $s = s_0 = 0.6$.

The values of ω_r and γ are plotted in Fig.5.7 as a function of $k_\theta \lambda_{Li} = nq_s\lambda_{Li}/as$ evaluated at $s = s_0$. The global results including trapped electron dynamics are given with full lines. Circles and stars identify the modes with dominant toroidal-ITG and TEM-type character respectively. The solutions from the local kinetic dispersion relation with input parameters $\tau = 1.0$, $\epsilon_n = 0.2$, $\eta_i = \eta_e = 2.0$, $\alpha_b = 55\%$, $G = 1.2$, and $\tilde{k}_\parallel= 0.1$ are again represented with dotted lines. The growth rate from the global calculations

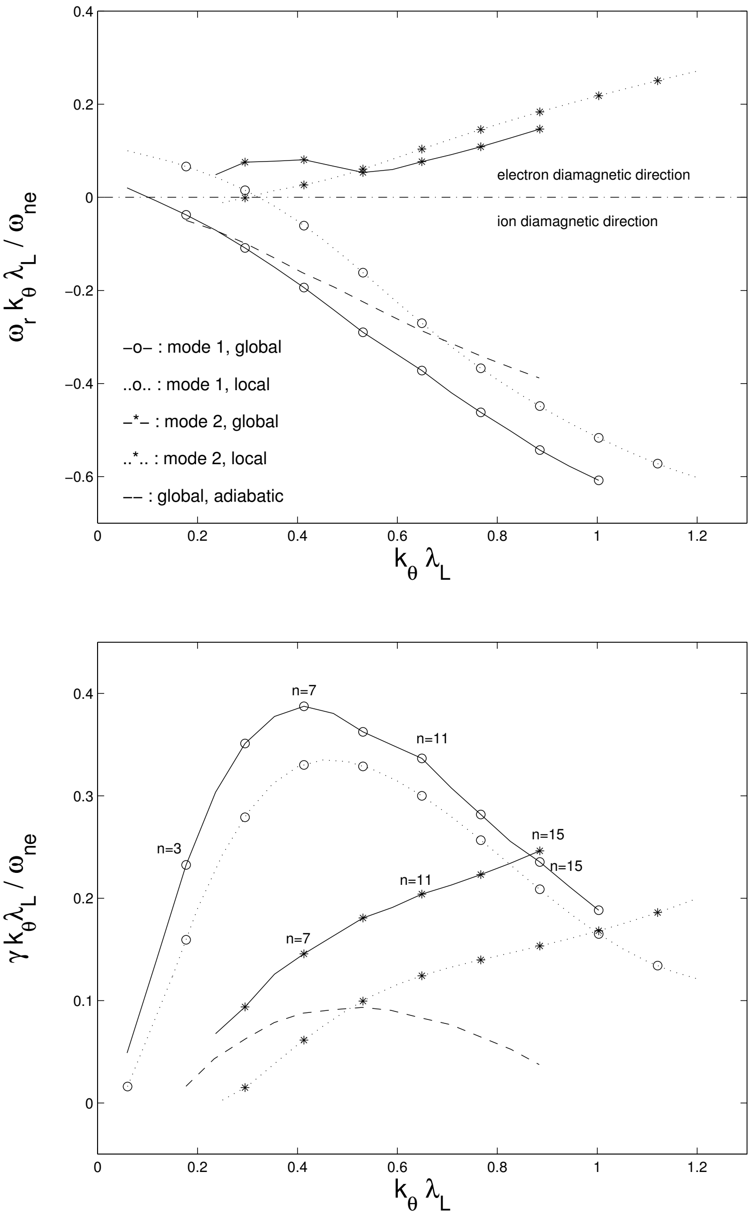

Figure 5.7: Real frequencies ω_r and growth rates γ as a function of $k_\theta \lambda_{L\,i} (\sim n)$. Global results are plotted with full lines and the solution to the local dispersion relation with dotted lines. The mode having essentially an ITG (respectively TEM) character is identified with circles (respectively stars). For comparison global calculations considering only the adiabatic response of electrons are represented with dashed lines.

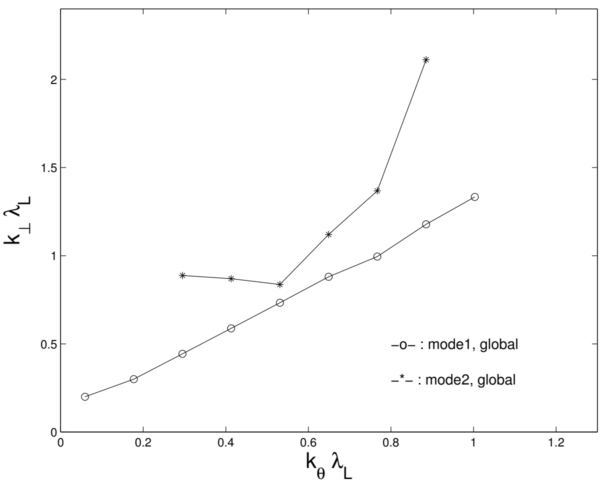

Figure 5.8: Average value of $k_\perp \lambda_{L\,i}$ as a function of $k_\theta \lambda_{L\,i}$ for modes 1 & 2.

with the adiabatic electron approximation is reported from Fig.4.9 with a dashed line.

As shown clearly in Fig.5.1 for $k_\theta \lambda_{L\,i} = 0.53$, $(\epsilon_n = 0.2, \eta_i = 2.0)$ corresponds to a relatively marginal state for the toroidal-ITG without trapped electrons, while the same mode including their dynamics remains well destabilized before conversion to the TEM. This explains why the effect of non-adiabatic electrons is very much emphasized along this n scan. The peak of the growth rate, reached here for $n = 7$ $(k_\theta \lambda_{L\,i} = 0.41)$, thus is enhanced by a factor ~ 4. The roll over of γ for values of $n \geq 8$ $(k_\theta \lambda_{L\,i} \gtrsim 0.5)$, reveals that the character of mode 1 is still predominantly determined by ions even though its growth rate is significantly increased by electrons. However for low toroidal wave numbers the mode slows down to the point where for $n = 1$ $(k_\theta \lambda_{L\,i} = 0.06)$ it starts propagating in the electron diamagnetic direction, showing a tendency to convert to a TEM-type instability instead of a slab-ITG. Structures of mode 1 appear in frames a.), b.), and c.) of Fig.5.9 for $n = 1, 7$ and 15 respectively, $n = 7$ being the most unstable. Note the ballooning and radially large coherent structures which are maintained down to $n = 1$ in contrast with the slab-like structure in frame d.) of Fig.4.13 when trapped electrons are neglected.

Mode 2, always propagating in the electron diamagnetic direction, is not attenuated by FLR effects of ions and its growth rate therefore keeps increasing up to the range

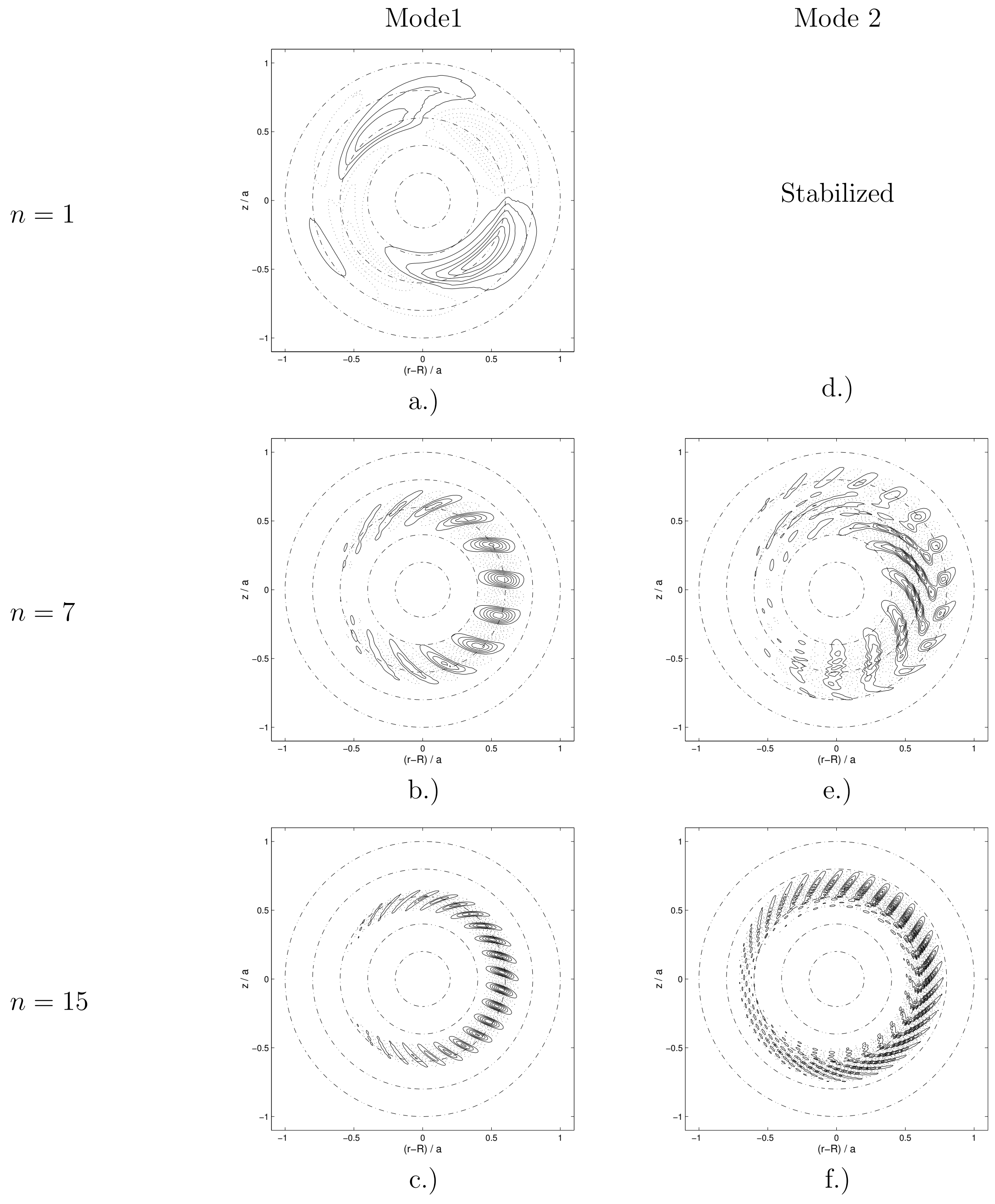

Figure 5.9: Structures of modes 1 & 2 for toroidal wave numbers $n = 1, 7, 15$.

$k_\theta \lambda_{L\,i} \sim 1$ considered here, confirming its TEM-type character. In this regime $k_\perp \lambda_{Le} = \sqrt{\tau m_e/m_i} k_\perp \lambda_{L\,i} \ll 1$, so that the drift kinetic approximation for electrons is still perfectly justified. For $n = 15$ ($k_\theta \lambda_{L\,i} = 0.89$) mode 2 in fact becomes more unstable then the toroidal-ITG. The corresponding structure is shown in frame f.) of Fig.5.9 with an average radial position shifted to $s = 0.7 > s_0$ and a short radial wavelength leading to $k_\perp \lambda_{L\,i} = 2.1$ (see Fig.5.8).

Conclusions

A gyrokinetic eigenvalue code has been developed for computing electrostatic ITG-related microinstabilities in collisionless tokamak plasmas. The global approach we have chosen is different from most previous linear studies which have been carried out using the ballooning representation, valid only for sufficiently high toroidal wave numbers and usually applied only to lowest order, that is local to a magnetic surface. Finite Larmor radius and finite orbit width effects of ions have been considered to all orders contrary to the only other global kinetic spectral code by Marchand, Tang and Rewoldt [27][28], which is based on a second order banana width expansion. Besides being more general in this respect, our model avoids in this way having to deal with spurious modes. The eigenvalue problem is then formulated as a two-dimensional integral equation for the perturbation in the poloidal plane.

Practical methods for solving the non-Hermitian equation had first to be devised and tested. Making use of a Fourier decomposition appears naturally when solving the gyrokinetic equation for ions as it allows one to perform gyroaveraging procedures of the unknown perturbing fields analytically. Furthermore it enables to give an explicit relation for the kernel of the integral form. Fourier transformations had been applied in different former lower-dimensional work [16][17][18]. However we have shown that in a curved system a wave decomposition into basic modes compatible with the geometry of the magnetic surfaces turns out to be more practical then the commonly used plane wave decomposition.

Remaining in this particular Fourier space seemed to be the best choice for solving numerically the eigenvalue equation. Nevertheless it was first tested in a cylindrical geometry against a finite element method in configuration space. This allowed us to validate the application of this non-standard decomposition to a finite system with realistic equilibrium profiles. For its many advantages over solving in configuration space, such as avoiding singularities in the kernel, the Fourier method was finally adopted for toroidal geometry.

A practical algorithm proposed by Davies [40] for finding the zeros of an analytical function was also first tested in cylinder for identifying the unstable spectrum. By sampling the determinant of the system along a closed curve in the complex frequency plane, this elaborated Nyquist technique allows one to actually localize with great accuracy the eigenfrequencies enclosed by such a path. Initially developed for sampling along circles, we have generalized this method to more elongated curves using conformal transformations.

In this work a large aspect ratio torus with circular concentric magnetic surfaces has been considered. This simple configuration enabled us to carry out the analytical derivations further then in a more general geometry. In a first toroidal model the modulation of the velocity parallel to the magnetic field was neglected so that in particular trapped particle dynamics, as well for ions as for electrons, were discarded. Comparisons [37] with simulations from a linear, time evolution, particle in cell code [35] developed in parallel provided a useful benchmark. This system allowed us to study the transition from the slab-ITG to the more unstable interchange-like toroidal-ITG mode when bending a periodic cylinder into a torus. For fixed toroidal wave number the spectrum in cylinder is formed by many eigenmodes with a given poloidal wave number, radially localized on the corresponding mode rational surfaces. The ability to resolve FLR effects, possibly to all orders, is crucial for computing these slab-like perturbations as perpendicular wavelengths typically become of the same order or shorter then the ion Larmor radii. Furthermore they provide the only radial coupling in cylinder. Going to torus the eigenmodes couple together in such a way that a single one converts to the full toroidal-ITG, characterized by a ballooned envelope and radially large coherent structures covering many rational surfaces.

The slab- to toroidal-ITG transition was also studied in a fixed tokamak configuration by varying the toroidal wave number n. Local calculations by Dong et al. [24][41], using the same model, allowed us to compare our global results to the ballooning approximation. As expected, good agreement was obtained for high n, i.e. approximately ten mode rational surfaces inside the radially unstable region. Results however differ for lower n, in particular as the transition to the slab-ITG takes place. This illustrates how ballooning representation is not suited for modes without an interchange-like character. One must point out that had one considered trapped ion dynamics, a transition to the TIM would have occured instead. However even in this case the validity of applying the ballooning approximation remains questionable as discussed by Xu and Rosenbluth [23].

In a second stage non-adiabatic trapped electron dynamics was added to the global model using the bounce-averaged drift kinetic equation. Beforehand the basic effects of these trapped particles were analyzed solving a local kinetic dispersion relation similar to the one considered by Romanelli and Briguglio [8]. In general they contribute directly to the growth rate of the toroidal-ITG and by amplifying the ballooning in the unfavorable curvature region they further enhance the ion drive. For a non-uniform density profile (low ϵ_n), they also remove the threshold on the ion temperature gradient for the onset of instability. This is achieved by a transition of the toroidal-ITG to the TEM as the ion temperature flattens. In this transition region and for sufficiently strong electron temperature gradients the spectrum can contain simultaneously these two types of modes. For high toroidal wave numbers the toroidal-ITG is damped due to FLR effects of ions while the TEM keeps on growing. Ultimately this would require taking into account finite banana width and Larmor radii of electrons.

Following recent experimental observations of core transport barriers in NCS discharges, we have studied the stabilizing effect of negative magnetic shear. Not only does it reduce the growth rate of the toroidal-ITG but also the radial extension by inducing a transition to a more slab-like mode. In the absence of trapped electron dynamics our global calculations predict a stronger attenuation when going to negative shear then the local ballooning calculations[41]. This probably again illustrates the problem of applying this representation in a slab-like regime. When considering trapped electron dynamics, these particles destabilize the ITG-type mode for all values of shear. The enhancement factor is however larger for negative values so that the stabilizing effect of shear is slightly reduced. This is in contradiction to some conclusions drawn by Dong et al.[59] who also included non-adiabatic electron dynamics in their local ballooning calculations. Anyway, realistic negative magnetic shear alone can only account for the complete suppression of the TEM but not of the ITG instability and thus is not sufficient to explain the dramatic improvement of confinement in the core of NCS discharges. Experimental results [43] point towards the $\vec{E} \times \vec{B}$ flow shear for being responsible of the full stabilization of these modes [66].

To fully exploit the advantages of this spectral code, the trapped ion dynamics must still be added so as to be able to analyze the TIM. This instability appears at low toroidal wave numbers where our global approach finds its real justification. Handling trapped ions is somewhat more complicated then trapped electrons. Indeed, if one wants to describe correctly the transition from the toroidal-ITG to the TIM one must take into account the contribution of all harmonics of the bounce frequency so that a bounce-averaged equation is not sufficient. Furthermore their finite banana width is not negligible. The physical modeling of these particles has been presented in appendix B and we are confident that the numerical methods already developed allow for a straightforward implementation. This will be done in the near future.

Appendix A

Deriving the Linearized Gyrokinetic Equation

The main steps for deriving the linearized gyrokinetic equation are presented. This approach is based on the work by P.J.Catto [12]. The method consists essentially in expanding the Vlasov equation to different orders in the small gyro-ordering parameter ϵ defined in Sec.2.5. This scaling leads to a reduction of phase space through a well defined gyroaveraging process.

A.1 Larmor Expansion of the Vlasov Equation

Considering a collisionless plasma, one begins with the Vlasov equation

$$\left.\frac{D}{Dt}\right|_{t.p.} f = \left[\frac{\partial}{\partial t} + \vec{v}\cdot\frac{\partial}{\partial\vec{r}} + \frac{q}{m}\left(\vec{E} + \vec{v}\times\vec{B}\right)\cdot\frac{\partial}{\partial\vec{v}}\right] f = 0, \tag{A.1}$$

$f(\vec{r},\vec{v},t)$ being the distribution function of a given species having electrical charge q and mass m. $(\vec{E},\vec{B})$ are the total electromagnetic, self-consistent fields. This equation is linearized with respect to small electrostatic perturbations of the stationary state, defined by the magnetic field $\vec{B}$ and the distribution function $F(\vec{r},\vec{v})$:

$$\left.\frac{D}{Dt}\right|_{u.t.p.} \tilde{f} = \left[\frac{\partial}{\partial t} + \vec{v}\cdot\frac{\partial}{\partial\vec{r}} + \frac{q}{m}\,\vec{v}\times\vec{B}\cdot\frac{\partial}{\partial\vec{v}}\right] \tilde{f} = \frac{q}{m}\nabla\phi\cdot\frac{\partial}{\partial\vec{v}}F, \tag{A.2}$$

$\tilde{f}$ being the fluctuating part of the distribution function, ϕ the electrostatic potential and $\left.\frac{D}{Dt}\right|_{u.t.p.}$ the total time derivative along unperturbed trajectories of particles. F must be a function of the constants of motion. We will consider here the case of an axisymmetric toroidal system so that F can be chosen function of kinetic energy $\mathcal{E} = v^2/2$ and the canonical momentum conjugated to the φ direction $\psi_0 = \psi + mrv_\varphi/q$, ψ being the poloidal magnetic flux. One assumes that the plasma is close to a local equilibrium, so that F is essentially Maxwellian:

$$F = F_M(\psi_0, \mathcal{E}) = \frac{N(\psi_0)}{[2\pi T(\psi_0)/m]^{3/2}} \exp - \left(\frac{\mathcal{E}}{T(\psi_0)/m} \right), \tag{A.3}$$

where to zero order in ϵ, N is the density and T the temperature on the magnetic surface ψ. Keeping terms to first order in ϵ, the right hand side of Eq.(A.2) can be written

$$\left.\frac{D}{Dt}\right|_{u.t.p.} \tilde{f} = \left.\frac{D}{Dt}\right|_{u.t.p.} \left(-\frac{q}{T}\phi F_M \right) + \frac{q}{T}\frac{\partial \phi}{\partial t} F_M - r\frac{B_p}{B}\nabla_b \phi \frac{\partial F_M}{\partial \psi} + O(\epsilon^2), \tag{A.4}$$

where the fact that $\left.\frac{D}{Dt}\right|_{u.t.p.} qF_M/T = 0$ and the relation $\vec{e}_\varphi = (B_\varphi \, \vec{e}_\parallel - B_p \, \vec{e}_b)/B$ have been used. Note that in equation (A.4), F_M can now be considered a function of $(\psi, \mathcal{E})$. Subtracting the adiabatic part of $\tilde{f}$ by defining

$$\tilde{g} = \tilde{f} + \frac{q}{T}\phi F_M, \tag{A.5}$$

one obtains

$$\left.\frac{D}{Dt}\right|_{u.t.p.} \tilde{g} = \frac{q}{T}\frac{\partial \phi}{\partial t} F_M + \frac{1}{B}\nabla_b \phi \nabla_n F_M, \tag{A.6}$$

using $\nabla_n = -rB_p \partial/\partial\psi$. The right hand side of Eq.(A.6) now only contains terms of order $O(\epsilon)$. Inspired by guiding center theory [50], one performs the following change of variables :

$$\begin{array}{ccc} \text{particle variables} & \Longleftrightarrow & \text{guiding center variables} \\ (\vec{r}, \vec{v}) & & \left(\vec{R}, \mathcal{E}, \mu, \alpha, \sigma = \text{sign}(v_\parallel) \right), \end{array}$$

with the definitions $\vec{v} = v_\perp(\cos\alpha \, \vec{e}_n + \sin\alpha \, \vec{e}_b) + v_\parallel \, \vec{e}_\parallel$, $\vec{R} = \vec{r} + (\vec{v} \times \vec{e}_\parallel)/\Omega$ for the guiding center position and $\mu = v_\perp^2/2B$ for the magnetic moment. In these new variables one can write

$$\begin{aligned} \left.\frac{D}{Dt}\right|_{u.t.p.} &= -\Omega \frac{\partial}{\partial \alpha} + \mathcal{L}^{(1)}, \\ \mathcal{L}^{(1)} &= \frac{\partial}{\partial t} + \vec{v}_\parallel \cdot \frac{\partial}{\partial \vec{R}} + \vec{v} \cdot \left[\frac{\partial \mu}{\partial \vec{r}} \frac{\partial}{\partial \mu} + \frac{\partial \alpha}{\partial \vec{r}} \frac{\partial}{\partial \alpha} - \left(\frac{\partial}{\partial \vec{r}} \frac{\vec{e}_\parallel}{\Omega} \right) \cdot \left(\vec{v} \times \frac{\partial}{\partial \vec{R}} \right) \right], \end{aligned}$$

where $-\Omega\partial/\partial\alpha \sim O(\epsilon^0)$ and $\mathcal{L}^{(1)} \sim O(\epsilon^1)$. Writing Eq.(A.6) to order $O(\epsilon^0)$ simply gives

$$-\Omega\frac{\partial}{\partial\alpha}\tilde{g}^{(0)}=0 \implies \tilde{g}^{(0)}\neq\tilde{g}^{(0)}(\alpha),$$

and to order $O(\epsilon^1)$ reads:

$$-\Omega\frac{\partial}{\partial\alpha}\tilde{g}^{(1)}+\mathcal{L}^{(1)}\tilde{g}^{(0)}=\frac{q}{T}\frac{\partial\phi}{\partial t}F_M+\frac{1}{B}\nabla_b\phi\nabla_nF_M. \tag{A.7}$$

A.2 Gyroaveraging and the Gyrokinetic Equation (GKE)

Due to the periodicity in α, Rel.(A.7) imposes an additional condition on $\tilde{g}^{(0)}$. Indeed, averaging over this gyroangle leads to the gyrokinetic equation:

$$\left.\frac{D}{Dt}\right|_{u.t.g.}\tilde{g}^{(0)}=\frac{q}{T}\frac{\partial<\phi>}{\partial t}F_M+\frac{1}{B}\nabla_b<\phi>\nabla_nF_M$$

where $<\phi>$ is the gyroaveraged potential:

$$<\phi>=\frac{1}{2\pi}\int_0^{2\pi}d\alpha\phi(\vec{r}=\vec{R}-\frac{\vec{v}\times\vec{e}_\parallel}{\Omega},t).$$

Hereafter the superscript (0) of $\tilde{g}$ is discarded as the derivation is limited to this lowest order.

Although one solves for the particle distribution function, the GKE has taken full advantage of guiding center theory as $\left.\frac{D}{Dt}\right|_{u.t.g.}$ stands for the total time derivative along the unperturbed trajectories of the GC [50]:

$$\left.\frac{D}{Dt}\right|_{u.t.g.}=\frac{\partial}{\partial t}+\vec{v}_g\cdot\frac{\partial}{\partial\vec{R}},$$

$\vec{v}_g$ being the GC velocity divided into parallel motion and drifts related to curvature and gradients of magnetic field:

$$\begin{aligned}\vec{v}_g &= v_\parallel\vec{e}_\parallel+\vec{v}_d,\\ \vec{v}_d &= \frac{1}{\Omega}\vec{e}_\parallel\times\left[v_\parallel^2\vec{e}_\parallel\cdot(\nabla\vec{e}_\parallel)+\frac{v_\perp^2}{2}\nabla\ln B\right].\end{aligned}$$

From MHD equilibrium one can easily show

$$\vec{B} \cdot (\nabla \vec{B}) = \nabla(\frac{1}{2}B^2 + \mu_0 p),$$

so that

$$\vec{v}_d = \frac{1}{\Omega}\, \vec{e}_\parallel \times \left[\left(\frac{v_\perp^2}{2} + v_\parallel^2 \right) \nabla \ln B + v_\parallel^2 \frac{\mu_0}{B^2} \nabla p \right],$$

and for a low pressure plasma one can approximate

$$\vec{v}_d = \frac{1}{\Omega} \left(\frac{v_\perp^2}{2} + v_\parallel^2 \right) \vec{e}_\parallel \times \nabla \ln B.$$

To be able to perform exactly the gyroaveraging of the unknown potential ϕ, we will consider here a plane wave decomposition:

$$\phi(\vec{r}) = \int d\vec{k}\; e^{i\vec{k}\cdot\vec{r}}\; \overset{\wedge}{\phi}(\vec{k}),$$

so that

$$<\phi> = \int d\vec{k}\; e^{i\vec{k}\cdot\vec{R}}\; \overset{\wedge}{\phi}(\vec{k}) \frac{1}{2\pi} \int_0^{2\pi} d\alpha\; \exp(-i\,\vec{k} \cdot \frac{\vec{v} \times \vec{e}_\parallel}{\Omega}) = \int d\vec{k}\; J_0\left(\frac{k_\perp v_\perp}{\Omega}\right) e^{i\vec{k}\cdot\vec{R}}\; \overset{\wedge}{\phi}(\vec{k}),$$

using the integral representation of the Bessel function [60]:

$$J_p(x) = \frac{1}{2\pi} \int_0^{2\pi} d\alpha \exp i(x \sin\alpha - p\alpha). \tag{A.8}$$

The GKE can now be written

$$\left.\frac{D}{Dt}\right|_{u.t.g.} \tilde{g}\,(\vec{R}, \mathcal{E}, \mu, \sigma, t) = \left[\frac{q}{T} F_M \frac{\partial}{\partial t} + \nabla_n F_M \frac{1}{B} \nabla_b \right] \int d\vec{k}\; J_0\left(\frac{k_\perp v_\perp}{\Omega}\right) e^{i\vec{k}\cdot\vec{R}}\; \overset{\wedge}{\phi}(\vec{k}, t).$$

A.3 The Propagator Solution to the GKE

Formally the GKE can always be solved by integrating along the GC trajectories defined by the first order differential equation

$$\frac{d\vec{R}'}{dt} = \vec{v}_g \left(\vec{R}'(t), \mathcal{E}, \mu, \sigma \right), \quad \text{with} \quad \vec{R}'(t=0) = \vec{R}.$$

As the unperturbed system is homogeneous in time, one can consider perturbations having a time dependence of the form $e^{-i\omega t}$. Solving the GKE is then essentially brought down to evaluating the propagator $\mathcal{P}$:

$$\begin{aligned} \tilde{g}\,(\vec{R}, \mathcal{E}, \mu, \sigma; \omega) &= -\frac{q}{T} F_M \int d\,\vec{k}\; J_0(\frac{k_\perp v_\perp}{\Omega}) e^{i\vec{k}\vec{R}} (\omega - \omega^\star) i \mathcal{P}\, \hat{\phi}\,(\vec{k}), & \text{(A.9)} \\ \mathcal{P}(\vec{R}, \vec{k}, \mathcal{E}, \mu, \sigma; \omega) &= \int_{-\infty}^{0} dt \exp i \left[\vec{k} \cdot (\vec{R}' - \vec{R}) - \omega t \right], & \text{(A.10)} \end{aligned}$$

where

$$\omega^\star = \frac{T}{qB} (\nabla_n \ln F_M) k_b = \omega_n \left[1 + \eta (\frac{\mathcal{E}}{v_{th}^2} - \frac{3}{2}) \right], \tag{A.11}$$

stands for the diamagnetic drift frequency with $\omega_n = T(\nabla_n \ln N) k_b / qB$, and by definition $v_{th}^2 = T/m$ is the thermal velocity squared. One must point out that in definition (A.10) for the propagator, $\Im m(\omega) > 0$ for the time integral to converge, in agreement with causality. Thus, it is mainly through the propagator that the solution to one system differs from another. In particular it contains all resonances. $\mathcal{P}$ is in fact the Green's function of the GKE and is solution of the differential equation

$$\left[-i\omega + \vec{v}_g \cdot \left(i\,\vec{k} + \frac{\partial}{\partial \vec{R}} \right) \right] \mathcal{P} = 1. \tag{A.12}$$

The perturbed particle density $\tilde{n}$ is evaluated from $\tilde{g}$ by integrating over velocity space after transforming back to particle variables which basically consists in replacing $\exp i\,\vec{k}\vec{R}$ in Eq.(A.9) by $\exp i\,\vec{k} \cdot \left[\vec{r} + (\vec{v} \times \vec{e}_\parallel)/\Omega \right]$:

$$\tilde{n} = \frac{q}{T} \left[-N\phi - \int d\,\vec{k}\; e^{i\vec{k}\cdot\vec{r}}\, \hat{\phi}\,(\vec{k}) \int d\,\vec{v}\; J_0^2(\frac{k_\perp v_\perp}{\Omega}) F_M (\omega - \omega^\star) i \mathcal{P} \right], \tag{A.13}$$

the gyroangle integration having been performed, providing a second Bessel function J_0, so that $d\,\vec{v} = 2\pi v_\perp dv_\perp dv_\parallel$.

Finally, note that it is the Fourier transform which enabled us to perform gyroaveraging and integrate along the GC trajectories explicitly although the field ϕ is unknown. For this reason, Fourier space appears as the natural representation in a gyrokinetic model.

Appendix B

The Propagator in a Toroidal Axisymmetric System

For completeness, the full propagator of an arbitrary tokamak-like system is derived. The limiting case of highly passing particles in a circular, large aspect ratio equilibrium is recovered. The results obtained are comparable with those of Rutherford and Frieman [10] as well as Taylor and Hastie [11].

B.1 General Case

The notations introduced in Sec.2.1 for a general toroidal, axisymmetric system are applied here. The solution (A.9) to the GKE is considered assuming that the plane wave decomposition has been transcribed to the general toroidal wave decomposition

$$\int d\vec{k}\hat{\phi}(\vec{k})e^{i\vec{k}\cdot\vec{r}} \longrightarrow \sum_m \int d\kappa\, \hat{\phi}_m(\kappa) \exp i(\kappa\psi + m\chi + n\varphi),$$

so that the local wave vector reads

$$\vec{k} = \kappa\nabla\psi + m\nabla\chi + n\nabla\varphi.$$

A systematic approach for evaluating the propagator entails solving the differential equation (A.12)

$$\left[-i\omega + \vec{v}_g \cdot (i\vec{k} + \frac{\partial}{\partial\vec{R}})\right]\mathcal{P} = 1.$$

The spatial variation of $\mathcal{P}$ is on the long scale of equilibrium. Thus in the frame of gyro-ordering the differential operator can be approximated by

$$\vec{v}_g \cdot \frac{\partial}{\partial \vec{R}} \simeq v_\parallel \, \vec{e}_\parallel \cdot \frac{\partial}{\partial \vec{R}} = -\frac{v_\parallel}{JB}\frac{\partial}{\partial \chi},$$

with the fact that $\mathcal{P}$ is independent of φ in an axisymmetric system. As an effect, drifts are taken into account iteratively by integrating their contributions along the lowest order trajectories which follow the magnetic field lines. The equation for $\mathcal{P}$ now reduces to an ordinary differential equation in χ:

$$\frac{\partial}{\partial \chi}\mathcal{P}(\chi, \sigma) = \frac{JB}{v_\parallel} i(\vec{k} \cdot \vec{v}_g - \omega)\mathcal{P}(\chi, \sigma) - \frac{JB}{v_\parallel}, \tag{B.1}$$

$(\psi, \kappa, m, n, \mathcal{E}, \mu; \omega)$ appearing as parameters. When integrating (B.1) one must distinguish between circulating particles, for which $v_\parallel = \sigma\sqrt{2\mathcal{E}(1 - \lambda B(\psi, \chi)/B_0)}$ always keeps the same sign, from trapped particles, for which $v_\parallel$ goes to zero at the turning points.

In the following we will use the definitions

$$S(\chi', \chi) = \int_\chi^{\chi'} d\chi'' \frac{JB}{v_\parallel}(\vec{k} \cdot \vec{v}_g - \omega) = S_0(\chi', \chi) + \sigma S_1(\chi', \chi),$$

with

$$\begin{aligned} S_0(\chi', \chi) &= \int_\chi^{\chi'} d\chi'' JB k_\parallel = -\int_\chi^{\chi'} d\chi''(n\frac{d\varphi}{d\chi} + m), \\ S_1(\chi', \chi) &= \int_\chi^{\chi'} d\chi'' \frac{JB}{|v_\parallel|}(\vec{k} \cdot \vec{v}_d - \omega) = \kappa\psi_d(\chi', \chi) + m\chi_d(\chi', \chi) + n\varphi_d(\chi', \chi) - \omega t(\chi', \chi), \end{aligned}$$

as $d\varphi/d\chi = -JB_\varphi/r$ and invoking the fact that drifts $\vec{v}_d$ are independent of σ. In appendix C it is shown in detail how the radial contribution can be integrated:

$$\psi_d(\chi', \chi) = \int_\chi^{\chi'} \frac{JB}{|v_\parallel|}\nabla\psi \cdot \vec{v}_d \, d\chi'' = \frac{rB_\varphi}{\Omega}|v_\parallel|\Big|_\chi^{\chi'}. \tag{B.2}$$

In most systems $|B_p/B_\varphi| \ll 1$ so that the contribution φ_d is negligible. However it is shown in appendix C that the simultaneous effect of $\vec{v}_\parallel$ and $\vec{v}_d$ give rise to a toroidal precessional drift. Due to the iterative method employed for handling drifts, this effect is not included here.

The different functions of two variables defined above naturally verify

$$\begin{aligned}\mathcal{F}(\chi',\chi) &= -\mathcal{F}(\chi,\chi'),\\ \mathcal{F}(\chi',\chi) &= \mathcal{F}(\chi',\chi'')+\mathcal{F}(\chi'',\chi),\\ \mathcal{F}(\chi+2\pi,\chi) &= \mathcal{F}(2\pi,0).\end{aligned}$$

B.1.1 Circulating Particles

In this case, (B.1) can be integrated over the complete poloidal revolution:

$$\mathcal{P}(\chi+2\pi)=\exp[iS(\chi+2\pi,\chi)]\left\{\mathcal{P}(\chi)-\int_{\chi}^{\chi+2\pi}d\chi'\frac{JB}{v_{\|}}\exp[-iS(\chi',\chi)]\right\},$$

and using the periodicity of $\mathcal{P}$ in χ:

$$\mathcal{P}(\chi)=\frac{1}{1-\exp[-iS(2\pi,0)]}\int_{\chi}^{\chi+2\pi}d\chi'\frac{JB}{v_{\|}}\exp[-iS(\chi',\chi)]. \tag{B.3}$$

Hence, for circulating particles the resonance of order p is given by

$$S(2\pi,0)=(nq_s-m)2\pi+\sigma\left[m\chi_d(2\pi,0)-\omega\tau_t\right]=p2\pi.$$

with $\tau_t=t(2\pi,0)$ the transit period and

$$q_s(\psi)=-\frac{1}{2\pi}\int_0^{2\pi}d\chi\frac{d\varphi}{d\chi},$$

the safety factor. Using (B.2) one obtained $\psi_d(2\pi,0)=0$ as $v_{\|}$ is periodic in χ, which clearly shows that the GC trajectories are closed curves in the poloidal plane.

As discussed in chapter 4, it can be useful to write the propagator as a sum of contributions corresponding to the different resonances. This so-called harmonic decomposition is obtained by taking the Fourier series of the periodic function

$$\begin{aligned}\frac{JB}{v_{\|}}e^{-i\Delta(\chi)} &= \sum_{p=-\infty}^{+\infty}\frac{C_p}{2\pi}e^{ip\chi}\\ &\Longleftrightarrow\\ C_p(\psi,\kappa,m,n,\mathcal{E},\mu,\sigma;\omega) &= \int_0^{2\pi}d\chi\frac{JB}{v_{\|}}e^{-i(\Delta(\chi)+p\chi)},\end{aligned}$$

with $\Delta(\chi) = S(\chi, 0) - S(2\pi, 0)\chi/2\pi$. Inserting this relation into (B.3) leads to

$$\mathcal{P}(\chi) = e^{i\Delta(\chi)} \sum_{p=-\infty}^{+\infty} \frac{C_p e^{ip\chi}}{i[S(2\pi, 0) - p2\pi]}. \tag{B.4}$$

B.1.2 Trapped Particles

In this case Eq.(B.1) can only be integrated up to the turning point angles χ_1 and χ_2:

$$\begin{aligned} \mathcal{P}(\chi_1, \sigma) &= \exp i[S_0(\chi_1, \chi) + \sigma S_1(\chi_1, \chi)] \times \\ &\left(\mathcal{P}(\chi, \sigma) - \sigma \int_{\chi}^{\chi_1} d\chi' \frac{JB}{|v_\parallel|} \exp -i[S_0(\chi', \chi) + \sigma S_1(\chi', \chi)]\right), \qquad \text{(B.5)} \\ \mathcal{P}(\chi_2, \sigma) &= \exp i[S_0(\chi_2, \chi) + \sigma S_1(\chi_2, \chi)] \times \\ &\left(\mathcal{P}(\chi, \sigma) - \sigma \int_{\chi}^{\chi_2} d\chi' \frac{JB}{|v_\parallel|} \exp -i[S_0(\chi', \chi) + \sigma S_1(\chi', \chi)]\right). \qquad \text{(B.6)} \end{aligned}$$

Integrating (B.1) between χ_1 and χ_2 for particles following the magnetic line in the opposite direction yields

$$\begin{aligned} \mathcal{P}(\chi_2, -\sigma) &= \exp i[S_0(\chi_2, \chi_1) - \sigma S_1(\chi_2, \chi_1)] \times \\ &\left(\mathcal{P}(\chi_1, -\sigma) + \sigma \int_{\chi_1}^{\chi_2} d\chi' \frac{JB}{|v_\parallel|} \exp -i[S_0(\chi', \chi_1) - \sigma S_1(\chi', \chi_1)]\right). \qquad \text{(B.7)} \end{aligned}$$

For trapped particles the propagators corresponding to σ=+1 and σ=−1 are not independent and must verify

$$\mathcal{P}(\chi_i, \sigma) = \mathcal{P}(\chi_i, -\sigma),$$

at the turning angles $\chi_i, i = 1, 2$. This allows one to solve the system (B.5)- (B.7) for $\mathcal{P}(\chi, \sigma)$:

$$\begin{aligned} \mathcal{P}(\chi, \sigma) &= \frac{\exp[-i\sigma S_1(\chi_1, \chi)]}{i \sin S_1(\chi_2, \chi_1)} \int_{\chi_1}^{\chi_2} d\chi' \frac{JB}{|v_\parallel|} \exp[-iS_0(\chi', \chi)] \cos S_1(\chi', \chi_2) \\ &\quad -\sigma \int_{\chi_1}^{\chi} d\chi' \frac{JB}{|v_\parallel|} \exp -i[S_0(\chi', \chi) + \sigma S_1(\chi', \chi)], \end{aligned}$$

defined for $\chi_1 < \chi < \chi_2$.

Here the resonance of order p is given by

$$2S_1(\chi_2, \chi_1) = \sigma\, [m2\chi_d(\chi_2, \chi_1) - \omega\tau_b] = p2\pi,$$

$\tau_b = 2t(\chi_2, \chi_1)$ being the bounce period. Note that over one such period the dynamics along the magnetic field is averaged out so that $k_\parallel$ does not appear in these resonances. Again applying (B.2) gave $\psi_d(\chi_2, \chi_1) = 0$ as $v_\parallel = 0$ at $\chi_{1,2}$, showing that the banana trajectories in the poloidal plane of these particles are closed as well.

B.2 Circular, Large Aspect Ratio Torus

As an illustration of the above results, let us consider the large aspect ratio equilibrium given by (2.6). In this simplified geometry (ψ, χ) are replaced by the polar coordinates (ρ, θ). The following list of relations comes in useful:

$$\begin{aligned}
JB &= Rq_s = \text{const}, \\
\frac{d\varphi}{d\theta} &= -q_s = \text{const}, \\
|v_\parallel| &= \sqrt{2\mathcal{E}\left[1 - \lambda(1 - A^{-1}\cos\theta)\right]}, \\
\vec{k} \cdot \vec{v}_d &= k_z v_{dz} = -v_{dz}(\kappa \sin\theta + k_\theta \cos\theta), \\
v_{dz} &= \frac{1}{\Omega}\left(\frac{v_\perp^2}{2} + v_\parallel^2\right)\frac{1}{R} \simeq \frac{\mathcal{E}(2-\lambda)}{\Omega R},
\end{aligned}$$

with $A^{-1} = \rho/R$ the inverse aspect ratio of the magnetic surface $\rho =$const. The θ dependence of $v_\parallel$ and $v_\perp$ in the drift term only gives rise to a weak modulation of the numerator and is therefore neglected.

In all cases, S_0 is given by

$$S_0(\theta', \theta) = (nq_s - m)(\theta' - \theta).$$

To calculate S_1:

$$S_1(\theta', \theta) = \kappa\rho_d(\theta', \theta) + m\theta_d(\theta', \theta) - \omega t(\theta', \theta),$$

one must evaluate

$$\rho_d(\theta) = \int_0^\theta d\theta' \frac{JB}{|v_\parallel|}\, \vec{v}_d \cdot \vec{e}_\rho = -\frac{Rq_s v_{dz}}{\sqrt{2\mathcal{E}}}\int_0^\theta d\theta' \frac{\sin\theta'}{\sqrt{1 - \lambda(1 - A^{-1}\cos\theta')}}, \tag{B.8}$$

$$\theta_d(\theta) = \int_0^\theta d\theta' \frac{JB}{|v_\parallel|} \frac{\vec{v}_d \cdot \vec{e_\theta}}{\rho} = -\frac{Rq_s v_{dz}}{\sqrt{2\mathcal{E}}\rho} \int_0^\theta d\theta' \frac{\cos\theta'}{\sqrt{1-\lambda(1-A^{-1}\cos\theta')}}, \tag{B.9}$$

$$t(\theta) = \int_0^\theta d\theta' \frac{JB}{|v_\parallel|} = \frac{Rq_s}{\sqrt{2\mathcal{E}}} \int_0^\theta \frac{d\theta'}{\sqrt{1-\lambda(1-A^{-1}\cos\theta')}}. \tag{B.10}$$

A convenient parameter for expressing these integrals is

$$X = \frac{1-\lambda B_{min}/B_0}{2\lambda A^{-1}},$$

allowing one, as λ, to classify the two groups of particles:

$$\begin{array}{lccc} \text{circulating:} & 0 < \lambda < \dfrac{B_0}{B_{max}} & \Longleftrightarrow & 1 < X < +\infty, \\ \text{trapped:} & \dfrac{B_0}{B_{max}} < \lambda < \dfrac{B_0}{B} < \dfrac{B_0}{B_{min}} & \Longleftrightarrow & 0 < \sin^2\dfrac{\theta}{2} < X < 1, \end{array}$$

with $B_{max,min} = B_0(1 \pm A^{-1})$ and $B = B_0(1 - A^{-1}\cos\theta)$ the magnetic field at the point of interest (ρ, θ). Contrary to λ, the boundary for X between circulating and trapped particles is independent of ρ. For trapped particles the turning point angles satisfy:

$$\frac{B(\rho,\theta_{1,2})}{B_0} = 1 - A^{-1}\cos\theta_{1,2} = \frac{1}{\lambda} \quad \Longleftrightarrow \quad \sin\frac{\theta_{1,2}}{2} = \pm\sqrt{X}.$$

Rel.(B.8) can be easily integrated in a common form for all particles:

$$\rho_d(\theta) = 2\sqrt{\frac{2}{\mathcal{E}}} \frac{Rq_s v_{dz}}{\sqrt{1-\lambda B_{min}/B_0}} X \left(\sqrt{1 - \frac{1}{X}\sin^2\frac{\theta}{2}} - 1 \right).$$

For $\theta_d(\theta)$ and $t(\theta)$, which can be expressed in terms of elliptic integrals of the first and second kind [67], one must however distinguish between circulating and trapped particles.

B.2.1 Circulating Particles

In this case one obtains

$$\theta_d(\theta) = -\sqrt{\frac{2}{\mathcal{E}}} \frac{1}{\rho} \frac{Rq_s v_{dz}}{\sqrt{1-\lambda B_{min}/B_0}} \left[(1-2X)\boldsymbol{F}(\frac{\theta}{2}, \frac{1}{X}) + 2X\boldsymbol{E}(\frac{\theta}{2}, \frac{1}{X}) \right],$$

$$t(\theta) = \sqrt{\frac{2}{\mathcal{E}}} \frac{Rq_s}{\sqrt{1-\lambda B_{min}/B_0}} \boldsymbol{F}(\frac{\theta}{2}, \frac{1}{X}).$$

Note that here $1/X < 1$.

The resonance of order p now reads

$$S(2\pi, 0) = (nq_s - m)2\pi + \sigma\tau_t \left\{ -k_\theta v_{dz} \left[(1 - 2X) + 2X \frac{\boldsymbol{E}(1/X)}{\boldsymbol{K}(1/X)} \right] - \omega \right\} = p2\pi,$$

where

$$\tau_t = 2t(\pi) = 2\sqrt{\frac{2}{\mathcal{E}}} \frac{Rq_s}{\sqrt{1 - \lambda B_{min}/B_0}} \boldsymbol{K}(\frac{1}{X}),$$

is the transit period, having used the definitions of the complete elliptic integrals of the first and second kind. An estimate of this period is obtained with $\lambda = 0$ (highly passing) and yields a transit frequency of the order

$$\omega_t = \frac{2\pi}{\tau_t} \sim \frac{v_{th}}{Rq_s}.$$

The radial excursion of circulating particles is given by

$$\Delta\rho_t = |\rho_d(\pi)| = 2q_s \frac{\sqrt{2\mathcal{E}}}{\Omega} \frac{2 - \lambda}{\sqrt{1 - \lambda B_{max}/B_0} + \sqrt{1 - \lambda B_{min}/B_0}},$$

which is typically of the order

$$\Delta\rho_t \sim \lambda_t = q_s \lambda_L.$$

The propagator for highly passing particles used in chapter 4 can easily be recovered from the general relation (B.4). For this one needs to take the limits

$$\begin{aligned} \lim_{\lambda \to 0} S(2\pi, 0) &= \left[(nq_s - m) - \frac{\omega}{\omega_t} \right] 2\pi, \\ \lim_{\lambda \to 0} \Delta(\theta) &= -x_t \left[\sin(\theta + \theta_{\vec{k}}) - \sin\theta_{\vec{k}} \right], \end{aligned}$$

using the notations of section 4.1 for ω_t, x_t, $\theta_{\vec{k}}$ and the fact that $\lim_{\lambda \to 0} \sigma\sqrt{2\mathcal{E}} = v_\parallel$. From

$$\frac{JB}{v_\parallel} e^{-i\Delta(\theta)} = \frac{1}{\omega_t} \exp ix_t \left[\sin(\theta + \theta_{\vec{k}}) - \sin\theta_{\vec{k}} \right] = \sum_{p=-\infty}^{+\infty} \frac{C_p}{2\pi} e^{ip\theta},$$

one can evaluate the Fourier coefficients of the harmonic decomposition:

$$C_p = \frac{2\pi}{\omega_t} J_p(x_t) \exp i(p\theta_{\vec{k}} - x_t \sin\theta_{\vec{k}}),$$

which are independent of ω in this limit. Inserting these results in (B.4) yields

$$\begin{aligned}
\mathcal{P}(\chi) &= \exp -ix_t\left[\sin(\theta+\theta_{\vec{k}})-\sin\theta_{\vec{k}}\right]\sum_{p=-\infty}^{+\infty}\frac{\frac{2\pi}{\omega_t}J_p(x_t)\exp i(p\theta_{\vec{k}}-x_t\sin\theta_{\vec{k}})}{i\left[(nq_s-m)-\omega/\omega_t-p\right]2\pi}e^{ip\theta}\\
&= \sum_{p,p'=-\infty}^{+\infty}\frac{J_p(x_t)J_{p'}(x_t)}{i\left[\omega_t(nq_s-m-p)-\omega\right]}\exp i(p-p')(\theta+\theta_{\vec{k}}),
\end{aligned}$$

which matches Rel.(4.6).

B.2.2 Trapped Particles

For this group one gets

$$\begin{aligned}
\theta_d(\theta) &= -\frac{1}{\sqrt{\mathcal{E}}}\frac{1}{\rho}\frac{Rq_sv_{dz}}{\sqrt{\lambda A^{-1}}}\left[2\boldsymbol{E}\left(\arcsin(\frac{1}{\sqrt{X}}\sin\frac{\theta}{2}),X\right)-\boldsymbol{F}\left(\arcsin(\frac{1}{\sqrt{X}}\sin\frac{\theta}{2}),X\right)\right],\\
t(\theta) &= \frac{1}{\sqrt{\mathcal{E}}}\frac{Rq_s}{\sqrt{\lambda A^{-1}}}\boldsymbol{F}\left(\arcsin(\frac{1}{\sqrt{X}}\sin\frac{\theta}{2}),X\right),
\end{aligned}$$

valid for $\theta_1=-\theta_2<\theta<\theta_2$. Here $X<1$.

The resonance of order p is given by

$$2S_1(\theta_2,\theta_1)=\sigma\tau_b\left\{-k_\theta v_{dz}\left[2\frac{\boldsymbol{E}(X)}{\boldsymbol{K}(X)}-1\right]-\omega\right\}=p2\pi,$$

where

$$\tau_b=4t(\theta_2)=\frac{4}{\sqrt{\mathcal{E}}}\frac{Rq_s}{\sqrt{\lambda A^{-1}}}\boldsymbol{K}(X),$$

is the bounce period. A good estimate for the bounce frequency is obtained taking $\lambda=1$:

$$\omega_b=\frac{2\pi}{\tau_b}\sim\sqrt{A^{-1}}\frac{v_{th}}{Rq_s}\sim\sqrt{A^{-1}}\omega_t.$$

The radial excursion for trapped particles reads

$$\Delta\rho_b=2|\rho_d(\theta_2)|=4q_s\frac{\sqrt{2\mathcal{E}}}{\Omega}\frac{(2-\lambda)\sqrt{1-\lambda B_{min}/B_0}}{\sqrt{2\lambda A^{-1}}},$$

with a typical value of the order

$$\Delta\rho_b\sim\frac{\lambda_t}{\sqrt{A^{-1}}}\sim\frac{\Delta\rho_t}{\sqrt{A^{-1}}}.$$

Appendix C

Toroidal Precessional Drift

In the same way as the Larmor rotation of magnetized particles is averaged to define the GC trajectory, the periodic motion of the GC of trapped particles, called the second periodicity, can be averaged in turn so as to extract the effective drift of the corresponding banana orbit. Indeed, it will be shown here how for trapped particles, in the particular case of an unperturbed tokamak-like system, the combined effect of parallel motion and perpendicular drifts of the GC results, over a bounce period, in an average toroidal drift. A simple expression for this so-called precessional drift $<\dot{\varphi}>$ is given in terms of the second (or longitudinal) adiabatic invariant $I_\parallel$:

$$\begin{aligned} <\dot{\varphi}> &= \frac{1}{\tau_b}\int_0^{\tau_b}\frac{d\varphi}{dt}dt = -\frac{m}{q}\frac{\partial I_\parallel/\partial\psi}{\partial I_\parallel/\partial\mathcal{E}}, && \text{(C.1)} \\ I_\parallel(\psi,\mathcal{E},\mu) &= \oint dl_\parallel v_\parallel = 2\int_{\chi_1}^{\chi_2} d\chi JB|v_\parallel|, && \text{(C.2)} \end{aligned}$$

with $\chi_{1,2}$ the turning point angles and $I_\parallel$ function of the poloidal flux ψ and the velocity variables $(\mathcal{E},\mu)$. The method given here for establishing C.1 is similar to the one used by Rosenbluth and Sloan [51]. Other references present derivations for general configurations [68] and non-stationary states [69].

C.1 Derivation in Terms of the Second Adiabatic Invariant

The coordinate χ is assumed to be defined such that (ψ, χ, φ) is an orthonormal set. In particular the associated Jacobian reads

$$J = \frac{1}{|\nabla\chi||\nabla\psi||\nabla\varphi|} = -\frac{1}{|\nabla\chi|B_p}.$$

The equation of motion of the GC is written here

$$\frac{d\vec{R}}{dt} = \vec{v}_g = v_\parallel \vec{e}_\parallel + \frac{1}{\Omega}\vec{e}_\parallel \times \left[\left(\frac{v_\perp^2}{2} + v_\parallel^2\right)\nabla \ln B + +v_\parallel^2 \frac{\mu_0}{B^2}\nabla p\right],$$

which can easily be transformed to the magnetic coordinates (ψ, χ, φ):

$$\begin{aligned}
\frac{d\psi}{dt} &= \frac{d\vec{R}}{dt}\cdot\nabla\psi = -\frac{1}{JB}\frac{rB_\varphi}{\Omega}\left(\frac{v_\perp^2}{2} + v_\parallel^2\right)\frac{\partial \ln B}{\partial\chi},\\
\frac{d\chi}{dt} &= \frac{d\vec{R}}{dt}\cdot\nabla\chi = -\frac{1}{JB}v_\parallel + \frac{1}{JB}\frac{rB_\varphi}{\Omega}\left[\left(\frac{v_\perp^2}{2} + v_\parallel^2\right)\frac{\partial \ln B}{\partial\psi} + v_\parallel^2\frac{\mu_0}{B^2}\frac{dp}{d\psi}\right],\\
\frac{d\varphi}{dt} &= \frac{d\vec{R}}{dt}\cdot\nabla\varphi = \frac{B_\varphi}{rB}v_\parallel + \frac{B_p^2}{\Omega B}\left[\left(\frac{v_\perp^2}{2} + v_\parallel^2\right)\frac{\partial \ln B}{\partial\psi} + v_\parallel^2\frac{\mu_0}{B^2}\frac{dp}{d\psi}\right].
\end{aligned}$$

Further keeping only terms up to first order in the small parameter $\epsilon = \lambda_L/L$:

$$\frac{d\psi}{d\chi} = \frac{d\psi}{dt}\left(\frac{d\chi}{dt}\right)^{-1} = \frac{rB_\varphi}{\Omega v_\parallel}\left(\frac{v_\perp^2}{2} + v_\parallel^2\right)\frac{\partial \ln B}{\partial\chi} = \frac{\partial}{\partial\chi}\left(-\frac{rB_\varphi}{\Omega}v_\parallel\right) = \frac{d}{d\chi}\left(-\frac{rB_\varphi}{\Omega}v_\parallel\right) + O(\epsilon^2),$$

having used $\partial(rB_\varphi)/\partial\chi = 0$ and $\partial v_\parallel/\partial\chi = -(v_\perp^2/2v_\parallel)\partial \ln B/\partial\chi$. In fact this last relation corresponds to the conservation of the canonical momentum conjugated to φ:

$$\psi_0 = \psi + mrv_\varphi/q = \text{const.}$$

Thus, as $v_\parallel$ goes to zero at the turning points, there is no effective radial excursion of the banana orbit:

$$\Delta\psi = \int_{\chi_1}^{\chi_2}\frac{d\psi}{d\chi}d\chi = -\frac{rB_\varphi}{\Omega}v_\parallel\Big|_{\chi_1}^{\chi_2} = 0.$$

In the same way one obtains

$$\frac{d\varphi}{d\chi} = \frac{d\varphi}{dt}\left(\frac{d\chi}{dt}\right)^{-1} = -\frac{JB_\varphi}{r} - \frac{JB^2}{\Omega v_\parallel}\left[\left(\frac{v_\perp^2}{2} + v_\parallel^2\right)\frac{\partial \ln B}{\partial\psi} + v_\parallel^2\frac{\mu_0}{B^2}\frac{dp}{d\psi}\right]. \tag{C.3}$$

When integrating over a banana orbit, the first term vanishes to zero order. However, to first order this is not the case as the radial excursion $\delta\psi = -(rB_\varphi/\Omega)v_\parallel$ depends on the sign of $v_\parallel$. For this reason one expands:

$$-\frac{JB_\varphi}{r} = -\frac{JB_\varphi}{r}\bigg|_{\psi=\psi_0} + \frac{\partial}{\partial\psi}\left(\frac{JB_\varphi}{r}\right)\frac{rB_\varphi}{\Omega}v_\parallel + O(\epsilon^2). \tag{C.4}$$

The Jacobian J of the magnetic coordinate transformation is naturally related to equilibrium. This appears explicitly by writing the Grad-Shafranov equation as follows:

$$(\nabla\times\vec{B})\cdot\vec{e_\varphi} = -\frac{r}{J}\frac{\partial}{\partial\psi}(JB_p^2) = \frac{1}{2r}\frac{d}{d\psi}(rB_\varphi)^2 + r\mu_0\frac{dp}{d\psi},$$

which can also be put in the form

$$\frac{rB_\varphi}{B}\frac{\partial}{\partial\psi}\left(\frac{JB_\varphi}{r}\right) = \frac{\partial}{\partial\psi}(JB) + \frac{J}{B}\frac{\partial}{\partial\psi}(\mu_0 p + \frac{1}{2}B^2). \tag{C.5}$$

Inserting (C.4) and (C.5) into (C.3) leads to

$$\frac{d\varphi}{d\chi} = -\frac{JB_\varphi}{r}\bigg|_{\psi=\psi_0} + \frac{m}{q}\frac{\partial}{\partial\psi}(JBv_\parallel).$$

The toroidal advance after a full banana orbit can now be evaluated:

$$\Delta\varphi == -2\frac{m}{q}\frac{\partial}{\partial\psi}\int_{\chi_1}^{\chi_2} d\chi JB|v_\parallel| = -\frac{m}{q}\frac{\partial}{\partial\psi}I_\parallel.$$

Noticing that the bounce period can also be expressed in terms of $I_\parallel$:

$$\tau_b = 2\int_{\chi_1}^{\chi_2} d\chi\frac{JB}{|v_\parallel|} = \frac{\partial}{\partial\mathcal{E}}2\int_{\chi_1}^{\chi_2} d\chi JB|v_\parallel| = \frac{\partial}{\partial\mathcal{E}}I_\parallel,$$

one finally obtains the average toroidal drift

$$<\dot{\varphi}> = \frac{\Delta\varphi}{\tau_b} = -\frac{m}{q}\frac{\partial I_\parallel/\partial\psi}{\partial I_\parallel/\partial\mathcal{E}}.$$

C.2 Circular Large Aspect Ratio Torus

Using the same notations as in Section B.2 one can express the longitudinal invariant in terms of complete elliptic integrals:

$$\begin{aligned} I_\parallel &= 2\int_{\theta_1}^{\theta_2} d\theta JB|v_\parallel| = 4Rq_s\sqrt{2\mathcal{E}}\int_0^{\theta_2} d\theta\sqrt{1-\lambda(1-A^{-1}\cos\theta)} \\ &= 16Rq_s\sqrt{\mathcal{E}\lambda A^{-1}}\left[(X-1)\boldsymbol{K}(X) + \boldsymbol{E}(X)\right], \end{aligned}$$

with $0 < X < 1$ for trapped particles. One then can evaluate

$$
\begin{aligned}
\frac{\partial}{\partial \psi} I_{\parallel}(\rho, \mathcal{E}, \mu) &= 16\sqrt{\mathcal{E}}\frac{q_s^2}{B_0}\frac{1}{\rho}\sqrt{\frac{\lambda}{A^{-1}}}\left\{\hat{s}\left[(X-1)\boldsymbol{K}(X)+\boldsymbol{E}(X)\right]+\frac{1}{2}\left[\boldsymbol{E}(X)-\frac{1}{2}\boldsymbol{K}(X)\right]\right\}, \\
\tau_b &= \frac{\partial}{\partial \mathcal{E}} I_{\parallel}(\rho, \mathcal{E}, \mu) = \frac{4}{\sqrt{\mathcal{E}}}\frac{Rq_s}{\sqrt{\lambda A^{-1}}}\boldsymbol{K}(X), \qquad \text{(C.6)}
\end{aligned}
$$

using $d\psi/d\rho = \rho B_0/q_s$, the definition for magnetic shear $\hat{s} = d\ln q_s/d\ln\rho$ and relations[60]:

$$
\begin{aligned}
\frac{d\boldsymbol{E}(m)}{dm} &= \frac{1}{2m}\left[\boldsymbol{E}(m)-\boldsymbol{K}(m)\right], \\
\frac{d\boldsymbol{K}(m)}{dm} &= \frac{1}{2m}\left[\frac{1}{1-m}\boldsymbol{E}(m)-\boldsymbol{K}(m)\right],
\end{aligned}
$$

so that the precessional drift reads[56]:

$$
\begin{aligned}
<\dot{\varphi}> &= -\frac{\mathcal{E}}{\Omega}\frac{1}{R}\frac{q_s}{\rho}G, \qquad \text{(C.7)} \\
G(X, A^{-1}, \hat{s}) &= 4\lambda\left\{\hat{s}\left[(X-1)+\frac{\boldsymbol{E}(X)}{\boldsymbol{K}(X)}\right]+\frac{1}{2}\left[\frac{\boldsymbol{E}(X)}{\boldsymbol{K}(X)}-\frac{1}{2}\right]\right\}.
\end{aligned}
$$

The limits

$$
\lim_{X\to 0} G = \frac{B_0}{B_{min}} \qquad \text{and} \qquad \lim_{X\to 1} G = -\frac{B_0}{B_{max}},
$$

show that the toroidal drift of barely trapped particles ($X = 1$) is always in the opposite direction from the one of deeply trapped ($X = 0$). To estimate the average value of G on a given magnetic surface over all possible values of X, this factor is integrated over the corresponding volume in velocity space at $\theta = 0$ using

$$
d^3v = \sum_{\sigma=\pm 1}\pi\frac{B}{B_0}\sqrt{\frac{2\mathcal{E}}{1-\lambda B/B_0}}d\mathcal{E}d\lambda,
$$

and $d\lambda/dX = -2A^{-1}\lambda^2$, so that:

$$
\begin{aligned}
< G > &= \left[\int_{B_0/B_{max}}^{B_0/B_{min}}\frac{d\lambda}{\sqrt{1-\lambda B_{min}/B_0}}\right]^{-1}\int_{B_0/B_{max}}^{B_0/B_{min}}\frac{d\lambda}{\sqrt{1-\lambda B_{min}/B_0}}G \\
&= \frac{B_{min}}{B_0}\frac{A^{-1}}{\sqrt{1-B_{min}/B_{max}}}\int_0^1 dX\frac{\lambda^2}{\sqrt{1-\lambda B_{min}/B_0}}G \\
&= \frac{1}{2}\left[< G >_{\hat{s}=1}(1+\hat{s}) + < G >_{\hat{s}=-1}(1-\hat{s})\right].
\end{aligned}
$$

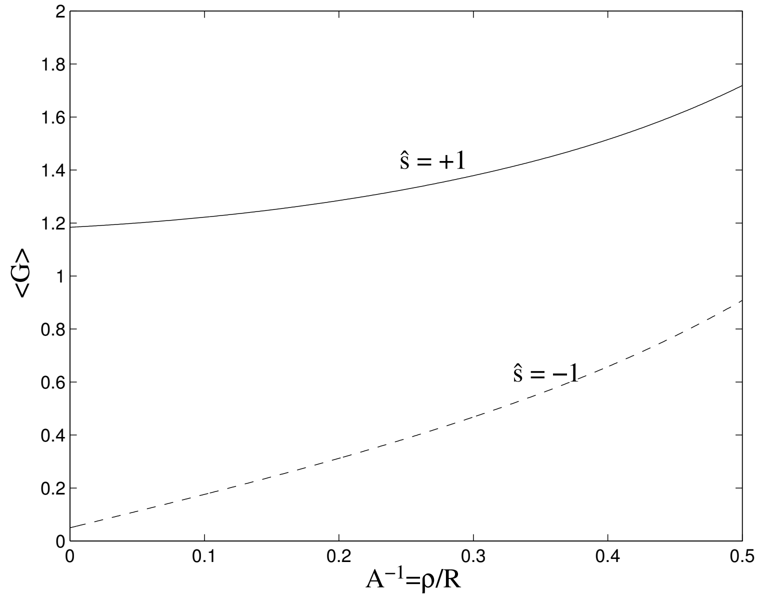

Figure C.1: Average factor $< G >$ of toroidal drift as a function of the inverse aspect ratio $A^{-1} = \rho/R$ for shear $\hat{s} = +1, -1$.

In Fig.C.1, $< G >_{\hat{s}=\pm 1}$ are plotted as a function of A^{-1}. These results show that one needs a strong reversed shear ($\hat{s} < -1$) for a given species of particles to drift on average opposite to the so-called diamagnetic direction.

C.3 The Bounce-Averaged Linearized Drift Kinetic Equation

In the case of a perturbation having a frequency ω significantly lower than the average bounce frequency $< \omega_b >$ of a given species, the wave interacts with the banana orbits as a whole, drifting with velocity $<\dot{\varphi}>$. These trapped particles can then be described by a bounce-averaged kinetic equation, which is obtained by averaging the DKE or GKE over this second periodicity in a similar way as these have been obtained by averaging the Vlasov equation over the Larmor gyration. An appropriate application are trapped electrons interacting with ITG-instabilities as in this case $\omega \sim \omega_i^\star$ so that

$$\frac{\omega}{\omega_{be}} \sim \frac{\omega_i^\star}{\omega_{be}} \sim \sqrt{\frac{m_e}{m_i}} \ll 1,$$

if $\tau = T_e/T_i \sim 1$. The Larmor radius of these particles being usually significantly smaller then all corresponding wave lengths, the DKE (2.22) is a justified starting point. This equation linearized for electrostatic perturbations reads

$$\left.\frac{D}{Dt}\right|_{u.t.g.}\tilde{f}_g=\left[\frac{\partial}{\partial t}+\vec{v}_g\cdot\frac{\partial}{\partial\vec{R}}\right]\tilde{f}_g=\frac{\nabla\phi\times\vec{B}}{B^2}\cdot\frac{\partial F_M}{\partial\vec{R}}+\frac{q}{m}\vec{v}_g\cdot\nabla\phi\frac{\partial F_M}{\partial\mathcal{E}},$$

where only the fluctuating part $\tilde{f}_g(\vec{R},\mathcal{E},\mu;t)$ of the GC distribution function relative to trapped particles shall be considered here. F_M is a Maxwellian distribution function of the form (A.3) but with $\psi_0 = \psi + mrB_\varphi v_\parallel/qB$ the gyroaveraged toroidal momentum. The right hand side can be expanded to give, in agreement with drift kinetic ordering:

$$\left.\frac{D}{Dt}\right|_{u.t.g.}\tilde{f}_g=\left.\frac{D}{Dt}\right|_{u.t.g.}\left(-\frac{q}{T}\phi F_M\right)+\frac{q}{T}\frac{\partial\phi}{\partial t}F_M+r\nabla_\varphi\phi\frac{\partial F_M}{\partial\psi},$$

where the fact that $\left.\frac{D}{Dt}\right|_{u.t.g.}qF_M/T=0$ and $\vec{e_\varphi}=(B_\varphi\,\vec{e_\parallel}-B_p\,\vec{e_b})/B$ have been used. In this last relation, F_M can now be considered a function of $(\psi,\mathcal{E})$. Defining the non-adiabatic part $\tilde{g}_g=\tilde{f}_g+q\phi F_M/T$, one can write for perturbations of the form $\exp i(\omega t-n\varphi)$:

$$\left.\frac{D}{Dt}\right|_{u.t.g.}\tilde{g}_g=-\frac{q}{T}F_M i(\omega-\omega^\star)\phi.$$

Note that here

$$\omega^\star=-\frac{T}{qB}(\nabla_n\ln F_M)\frac{B}{B_p}k_\varphi=\omega_n\left[1+\eta\left(\frac{\mathcal{E}}{v_{th}^2}-\frac{3}{2}\right)\right],\qquad\omega_n=-\frac{T}{qB}(\nabla_n\ln N)\frac{B}{B_p}k_\varphi,$$

and that one can recover the definition (A.11) for the GKE by reminding that $k_\parallel = (Bk_\varphi+B_pk_b)/B_\varphi \ll k_\perp$ in gyro-ordering. This equation will now be expanded to different orders in the small parameter $\epsilon_b=\omega/\omega_b\ll 1$. Subtracting the slow precessional drift $<\dot{\varphi}>$ from the fast periodic trapping motion and assuming $\omega\sim\omega^\star$, one can write to lowest order in ϵ_b:

$$\left(\vec{v}_g\cdot\frac{\partial}{\partial\vec{R}}-<\dot{\varphi}>\frac{\partial}{\partial\varphi}\right)\tilde{g}_g^{(0)}=0,$$

which implies that $\tilde{g}_g^{(0)}$ is constant along the non-drifting banana orbits, and to first order:

$$\left(\vec{v}_g\cdot\frac{\partial}{\partial\vec{R}}-<\dot{\varphi}>\frac{\partial}{\partial\varphi}\right)\tilde{g}_g^{(1)}-i(\omega-n<\dot{\varphi}>)\,\tilde{g}_g^{(0)}=-\frac{q}{T}F_M i(\omega-\omega^\star)\phi.$$

By averaging this last relation over a complete banana trajectory leads to an additional condition for $\overset{\sim(0)}{g}_g$, that is the actual bounce-averaged equation:

$$(\omega - n <\dot{\varphi}>) \overset{\sim(0)}{g}_g = \frac{q}{T} F_M (\omega - \omega^\star) < \phi >_b,$$

which is trivial to solve:

$$\tilde{g}_g = \frac{q}{T} F_M \frac{\omega - \omega^\star}{\omega - n <\dot{\varphi}>} < \phi >_b, \tag{C.8}$$

with

$$< \phi >_b (\vec{R}, \mathcal{E}, \mu) = \frac{1}{\tau_b} \int_0^{\tau_b} dt \phi(\vec{R}'), \qquad \vec{R}' (t = 0) = \vec{R} .$$

By integrating only along the parallel motion of the GC, thus neglecting finite banana width effects, which is a good approximation for electrons, one obtains

$$\begin{aligned} < \phi >_b &= \frac{1}{\tau_b} \int_0^{\tau_b} dt \phi(\psi, \chi') e^{in\varphi'} = \frac{1}{\tau_b} 2 \int_{\chi_1}^{\chi_2} d\chi' \frac{JB}{|v_\parallel|} \phi(\psi, \chi') \exp in \left(\varphi - \int_\chi^{\chi'} \frac{JB_\varphi}{r} d\chi'' \right) \\ &= \bar{\phi} (\psi, \lambda) \exp in \left(\varphi + \int^\chi d\chi' \frac{JB_\varphi}{r} \right), \end{aligned}$$

defining

$$\bar{\phi} (\psi, \lambda) = \left(\int_{\chi_1}^{\chi_2} d\chi \frac{JB}{\sqrt{1 - \lambda B / B_0}} \right)^{-1} \int_{\chi_1}^{\chi_2} d\chi \frac{JB}{\sqrt{1 - \lambda B / B_0}} \phi(\psi, \chi) \exp -in \int^\chi d\chi' \frac{JB_\varphi}{r},$$

and having used ψ=const, $d\chi/dt = -v_\parallel/JB$, $d\varphi/d\chi = -JB_\varphi/r$ along these lowest order trajectories.

Bibliography

[1] S.Ejima *et al.*, Nuclear Fusion **22**, 1627 (1982).

[2] A.A.Galeev and R.Z.Sagdeev, Zh.Eksp.Teor.Fiz.**53**, 348 (1967), [Soviet Physics JETP **26**, 233 (1968)].

[3] M.Greenwald *et al.*, in *Plasma Physics and Controlled Nuclear Fusion Research 1984, London* (IAEA, Vienna, 1985), Vol. 1, p. 45.

[4] L.I.Rudakov and R.Z.Sagdeev, Nuclear Fusion Suppl. 1962 **2**, 481 (1962).

[5] W.Horton Jr., D.I.Choi, and W.M.Tang, Physics of Fluids **24**, 1077 (1981).

[6] B.B.Kadomtsev and O.P.Pogutse, Zh.Eksp.Teor.Fiz. **51**, 1734 (1966), [Soviet Physics JETP **24**, 1172 (1967)].

[7] B.B.Kadomtsev and O.P.Pogutse, Nuclear Fusion **11**, 67 (1971).

[8] F.Romanelli and S.Briguglio, Physics of Fluids B **2**, 754 (1990).

[9] W.A.Peebles *et al.*, in *Plasma Physics and Controlled Nuclear Fusion Research 1990, Washington DC* (IAEA, Vienna, 1991), Vol. 1, p. 589.

[10] P.H.Rutherford and E.A.Frieman, Physics of Fluids **11**, 569 (1968).

[11] J.B.Taylor and R.J.Hastie, Plasma Physics **10**, 479 (1968).

[12] P.J.Catto, Plasma Physics **20**, 719 (1978).

[13] E.A.Frieman and L.Chen, Physics of Fluids **25**, 502 (1982).

[14] T.S.Hahm, Physics of Fluids **31**, 2670 (1988).

[15] D.W.Ross and S.M.Mahajan, Physical Review Letters **40**, 324 (1978).

[16] W.M.Tang, G.Rewoldt, and E.A.Frieman, Physics of Fluids **23**, 2454 (1980).

[17] R.Marchand, C.F.Zhang, and Y.C.Lee, Physics of Fluids **26**, 194 (1983).

[18] R.D.Ferraro, H.Sanuki, R.G.Littlejohn, and B.D.Fried, Physics of Fluids **28**, 2181 (1985).

[19] J.W.Connor, R.J.Hastie, and J.B.Taylor, Physical Review Letters **40**, 396 (1978).

[20] E.A.Frieman, G.Rewoldt, W.M.Tang, and A.H.Glasser, Physics of Fluids **23**, 1750 (1980).

[21] G.Rewoldt, W.M.Tang, and M.S.Chance, Physics of Fluids **25**, 480 (1982).

[22] F.Romanelli, Physics of Fluids B **1**, 1018 (1989).

[23] X.Q.Xu and M.N.Rosenbluth, Physics of Fluids B **3**, 627 (1991).

[24] J.Q.Dong, W.Horton, and J.Y.Kim, Physics of Fluids B **4**, 1867 (1992).

[25] M.Kotschenreuther, G.Rewoldt, and W.M.Tang, Computer Physics Communications **88**, 128 (1995).

[26] F.W.Perkins *et al.*, Physics of Fluids B **5**, 477 (1993).

[27] R.Marchand, W.M.Tang, and G.Rewoldt, Physics of Fluids **23**, 1164 (1980).

[28] W.M.Tang and G.Rewoldt, Physics of Fluids B **5**, 2451 (1993).

[29] M.Artun, W.M.Tang, and G.Rewoldt, Physics of Plasmas **2**, 3384 (1995).

[30] M.A.Beer, Ph.D. thesis, Princeton University, 1995.

[31] M.Kotschenreuther, W.Dorland, M.A.Beer, and G.W.Hammett, Physics of Plasmas **2**, 2381 (1995).

[32] S.E.Parker, W.W.Lee, and R.A.Santoro, Physical Review Letters **71**, 2042 (1993).

[33] R.D.Sydora, Physica Scripta **52**, 474 (1995).

[34] R.D.Sydora, V.K.Decyk, and J.M.Dawson, to be published in Plasma Physics and Controlled Fusion.

[35] M.Fivaz *et al.*, in *Theory of Fusion Plasmas, Int. Workshop, Varenna, August 1996* (Editrice Compositori, Societa Italiana di Fisica, Bologna, 1997), p. 485.

[36] M.Fivaz *et al.*, Physical Review Letters **78**, 3471 (1997).

[37] S.Brunner *et al.*, in *Theory of Fusion Plasmas, Int. Workshop, Varenna, August 1996* (Editrice Compositori, Societa Italiana di Fisica, Bologna, 1997), p. 101.

[38] J.W.Connor and H.R.Wilson, Plasma Physics and Controlled Fusion **36**, 719 (1994).

[39] S.Brunner and J.Vaclavik, submitted for publication in Physics of Plasmas.

[40] B.Davies, Journal of Computational Physics **66**, 36 (1986).

[41] J.Q.Dong, Y.Z.Zhang, S.M.Mahajan, and P.N.Guzdar, Physics of Plasmas **3**, 3065 (1996).

[42] F.M.Levinton *et al.*, Physical Review Letters **75**, 4417 (1995).

[43] L.L.Lao *et al.*, Physics of Plasmas **3**, 1951 (1996).

[44] B.W.Rice *et al.*, Physics of Plasmas **3**, 1983 (1996).

[45] Y.Neyatani and the JT-60 Team, Plasma Physics and Controlled Fusion **38**, A181 (1996).

[46] C.Kessel, J.Manickam, G.Rewoldt, and W.M.Tang, Physical Review Letters **72**, 1212 (1994).

[47] M.S.Chu *et al.*, Physical Review Letters **77**, 2710 (1996).

[48] V.D.Shafranov, in *Reviews of Plasma Physics* (M.A.Leontovich, Consultants Bureau, New York, 1966), Vol. 2, p. 103.

[49] L.S.Solovev, Zh.Eksp.Teor.Fiz. **53**, 626 (1967), [Soviet Physics JETP **26**, 400 (1968)].

[50] D.V.Sivukhin, in *Reviews of Plasma Physics* (M.A.Leontovich, Consultants Bureau, New York, 1965), Vol. 1, p. 1.

[51] M.Rosenbluth and M.L.Sloan, Physics of Fluids **14**, 1725 (1971).

[52] B.D.Fried and S.D.Conte, *The Plasma Dispersion Function* (Academic, New York, 1961).

[53] A.B.Mikhailovskii, *Theory of Plasma Instabilities, Volume 2: Instabilities of an Inhomogeneous Plasma* (Consultants Bureau, New York, 1974).

[54] X.Garbet *et al.*, Physics of Fluids B **4**, 136 (1992).

[55] R.D.Hazeltine and W.A.Newcomb, Physics of Fluids B **2**, 7 (1990).

[56] B.B.Kadomtsev and O.P.Pogutse, in *Reviews of Plasma Physics* (M.A.Leontovich, Consultants Bureau, New York, 1970), Vol. 5, p. 249.

[57] W.M.Tang, J.C.Adam, and D.W.Ross, Physics of Fluids **20**, 430 (1977).

[58] G.Rewoldt and W.M.Tang, Physics of Fluids B **2**, 318 (1990).

[59] J.Q.Dong, S.M.Mahajan, and W.Horton, Physics of Plasmas **4**, 755 (1997).

[60] I.S.Gradshteyn and I.M.Ryzhik, *Table of Integrals, Series, and Products* (Academic, New York, 1965).

[61] O.Sauter, J.Vaclavik, and F.Skiff, Physics of Fluids B **2**, 475 (1990).

[62] S.Brunner and J.Vaclavik, in *Proceedings of the 22nd European Physical Society Conference on Controlled Fusion and Plasma Physics, Bournemouth 1995* (European Physical Society, Abingdon, 1995), Vol. IV, p. 241.

[63] W.Gautschi, SIAM Journal of Numerical Analysis **7**, 187 (1970).

[64] B.B.Kadomtsev, *Plasma Turbulence* (Academic, London and New York, 1965).

[65] W.H.Press, B.P.Flannery, S.A.Teukolsky, and W.T.Vetterling, *Numerical Recipes, The Art of Scientific Computing* (Cambridge University Press, Cambridge, 1986).

[66] T.S.Hahm and K.H.Burrell, Physics of Plasmas **2**, 1648 (1995).

[67] M.Abramowitz and I.A.Stegun, *Handbook of Mathematical Functions with Formulas, Graphs, and Mathematical Tables* (John Wiley & Sons, New York, 1964).

[68] B.B.Kadomtsev, in *Plasma Physics and the Problem of Controlled Thermonuclear reactions* (M.A.Leontovich, Pergamon Press, London, 1959), Vol. III, p. 340.

[69] T.G.Northrop, *The Adiabatic Motion of Charged Particles* (John Wiley & Sons, New York, 1963).

Curriculum Vitae

Name: Stephan BRUNNER

Age: 29 (Born September 26 1967, in Geneva, Switzerland)

Nationality: Swiss (Wald, ZH)

Schooling:

- First years of primary school in New Jersey, USA.
- **Summer 1986:** Scientific baccalaureate, Gymnase du Bugnon, Lausanne.

Studies:

- **Spring 1992:** Graduated in Physics from EPFL.
- **Spring 1992-Fall 1993:** Employed at CRPP as assistant.
- **Fall 1993:** Inscribed as Phd student at the CRPP.

Publications:

1. S.Brunner and J.Vaclavik, *Dielectric tensor operator of hot plasmas in toroidal axisymmetric systems*, Phys.Fluids B **5**, 1695 (1993)
2. L.Villard, S.Brunner, A.Jaun and J.Vaclavik, *Alfvèn wave heating and stability*, Physica Scripta T60, 44 (1995)
3. L.Villard, S.Brunner and J.Vaclavik, *Global marginal stability of TAEs in the presence of fast ions*, Nuclear Fusion **35**, 1173 (1995)
4. M.Fivaz, S.Brunner, W.Schwarzenbach, A.A.Howling and Ch.Hollenstein, *Reconstruction of the time-averaged sheath potential profile in an Argon RF plasma using the ion energy distribution*, Plasma Sources Science and Technology **4**, 373 (1995)

5. W.Schwarzenbach, A.A.Howling, M.Fivaz, S.Brunner and Ch.Hollenstein, *Sheath impedance effects in very high frequency plasma experiments*, J.Vac.Sci.Technol.A **14**, 132 (1996)
6. S.Brunner and J.Vaclavik, *Global approach to the spectral problem of microinstabilities in a cylindrical plasma using a gyrokinetic model*, submitted for publication in Physics of Plasmas

Proceedings and Posters (as first author):

1. S.Brunner and J.Vaclavik, *On absorption of low frequency electromagnetic fields*, 5th European Fusion Theory Conference, Madrid, Spain, September 1993
2. S.Brunner, L.Villard and J.Vaclavik, *A kinetic model for the global power transfer between particles and MHD waves*, Proc. Joint Varenna-Lausanne Int. Workshop on Theory of Fusion Plasmas, Varenna, Italy, August 1994, ISPP-15, 431 (1994)
3. S.Brunner and J.Vaclavik, *Spectra and mode structures of global drift waves in toroidal geometry*, Proc. Int. Sherwood Fusion Theory Conference, Incline Village, NV USA, April 1995, 1C51 (1995)
4. S.Brunner and J.Vaclavik, *Spectra and mode structures of global drift waves in toroidal geometry*, Proc. 22nd EPS Conference on Controlled Fusion and Plasma Physics, Bournemouth, Great Britain, July 1995, Vol.19C, Part.IV, 241 (1995)
5. S.Brunner, J.Vaclavik, M.Fivaz and K.Appert, *The spectral problem of global microinstabilities in tokamak-like plasmas using a gyrokinetic model*, Proc. Int. Sherwood Fusion Theory Conference, Philadelphia, PA, USA, March 1996, 2C13 (1996)

Invited Talks:

1. S.Brunner and J.Vaclavik, *Onde de dérive dans un modèle gyrocinétique: Résolution du problème spectral dans un cylindre*, GdR Sparch, Ecole Polytechnique, Paris, France, Octobre 1995

2. S.Brunner, J.Vaclavik, M.Fivaz, T.M.Tran and K.Appert, *Linear study of global microinstabilities using spectral and PIC methods*, Joint Varenna-Lausanne Int. Workshop on Theory of Fusion Plasmas, Varenna, Italy, August 1996